The Design, Fabrication and Characterization of Capacitive Micromachined Ultrasonic Transducers for Imaging Applications

by

Andrew Stephan Logan

A thesis
presented to the University of Waterloo
in fulfillment of the
thesis requirement for the degree of
Doctor of Philosophy
in
Systems Design Engineering

Waterloo, Ontario, Canada, 2010

AUTHOR'S DECLARATION

I hereby declare that I am the sole author of this thesis. This is a true copy of the thesis, including any required final revisions, as accepted by my examiners.

I understand that my thesis may be made electronically available to the public.

Abstract

Capacitive micromachined ultrasonic transducers (CMUTs) have proven themselves to be excellent candidates for medical ultrasonic imaging applications. The use of semiconductor fabrication techniques facilitates the fabrication of high quality arrays of uniform cells and elements, broad acoustic bandwidth, the potential to integrate the transducers with the necessary electronics, and the opportunity to exploit the benefits of batch fabrication.

In this thesis, the design, fabrication and testing of one- and two-dimensional CMUT arrays using a novel wafer bonding process whereby the membrane and the insulation layer are both silicon nitride is reported. A user-grown insulating membrane layer avoids the need for expensive SOI wafers, permits optimization of the electrode size, and allows more freedom in selecting the membrane thickness, while also enjoying the benefits of wafer bonding fabrication. Using a row-column addressing scheme for an *NxN* two-dimensional array permits three-dimensional imaging with a large reduction in the complexity of the array when compared to a conventional 2D array with connections to all N^2 elements. Only 2*N* connections are required and the image acquisition rate has the potential to be greatly increased. A simplification of the device at the imaging end will facilitate the integration of a three-dimensional imaging CMUT array into either an endoscope or catheter which is the ultimate purpose of this research project.

To date, many sizes of transducers which operate at different frequencies have been successfully fabricated. Initial characterization in terms of resonant frequency and, transmission and reception in immersion has been performed on most of the device types. Extensive characterization has been performed with a linear 32 element array transducer and a 32x32 element row-column transducer. Two- and three-dimensional phased array imaging has been demonstrated.

Acknowledgements

I would like to thank the many people who, in many different ways, have helped me complete this thesis. Yanhui Bai has been a good friend during my time here. He and I shared the long, endless hours together at the Cornell Nanofabrication Facility as we heroically struggled to fabricate our respective MEMS devices. If you are going to be working 20 hour days in a cleanroom, for days on end, it is much better to have a friend be there with you who understands the many ups and downs of fabrication and knows the specific type of uncomfortable you get from trying to grab a 30 minute nap in the lobby chair in the wee hours of the morning as you wait for the LPCVD furnace to cool down. Yanhui was that friend.

I also want to mention the other lab members who made the time pass much more enjoyably. Mohsen Shahini for the many esoteric discussions completely unrelated to research, Yun Wang for commiserating over the difficulties of graduate life and Sangtak Park for letting me bother him on many occasions about how one should go about fabricating an ultrasonic beamformer.

I would like to thank my supervisor, John Yeow, for giving me the opportunity to work in his lab. It takes a special kind of supervisor to send a student off to CNF to find a new way to fabricate CMUTs knowing that bills from hundreds to thousands of dollars would be showing up at the end of the week. Being able to take the lead on a new project has been exceptionally challenging and rewarding, and for that I am thankful. I would also like to thank the funding agencies that made this possible, the Natural Sciences and Engineering Research Council, the Canadian Institutes of Health Research, the Waterloo Institute of Nanotechnology, CMC Microsystems and the University of Waterloo.

I want to thank my parents for always supporting me through the many endeavours I've taken throughout my life, academic and otherwise. I would also like to mention my two wonderful daughters, Quinn and Kate, who, while not providing much technical advice, did help me finish this work by bringing many a smile to my face after a tough day in the lab. An enthusiastic "Daddy!!" and a great big grin as you walk in the door lets you quickly forget your troubles.

Finally, and most importantly, I would like to acknowledge the support and incredible patience of my beautiful wife, Michelle, over my nearly 7 years in graduate school. It cannot have been easy dealing with the long and irregular hours that come from being a graduate student. This is particularly

true during her first pregnancy, as I was frequently away in Ithaca, and in the final hectic months of my degree when I wouldn't come home until both kids were (hopefully) asleep. Thank you.

Table of Contents

List of Figures

List of Tables

Chapter 1 Introduction

1.1 Outline

This section provides a brief outline of the material covered in this thesis. In Chapter 1 the motivation behind the work done for this project is discussed. The contributions others have made toward the advancement of this project are acknowledged.

The second chapter presents the relevant background pertaining to ultrasound transducers and more specifically to capacitive micromachined ultrasonic transducers (CMUTs). The fundamentals of ultrasound imaging are described with a focus on using phased arrays. Current CMUT fabrication techniques are described.

In Chapter 3 the equivalent circuit method of modeling the CMUT is presented and applied to a few transducer designs.

In Chapter 4 the result of the first generation of fabricated CMUTs is reported. A detailed look at the novel fabrication process is followed by the electrical and acoustic characterization results. The lack of dielectric charging experienced by these devices is discussed in some detail.

In Chapter 5 a slightly simplified fabrication process is discussed. This is followed by electrical and acoustic characterization results from the devices which are suitable for phased array imaging. The design and implementation of a custom built transmit beamformer is discussed in detail. The performance of the beamformer is presented. Finally, the results of simple two-dimensional imaging are reported.

In Chapter 6 a unique way of obtaining three-dimensional images from a transducer little more complicated than a linear one-dimensional array is reported. The details of using a so-called row-column electrode transducer, as well as some of the advantages and disadvantages of such a technique, are discussed. A modified fabrication process is used to achieve this type of device; it is described in brief. The advantages of implementing this technique using CMUTs rather than piezoelectric transducers are reported. To drive this type of transducer, a beamformer different from the one used for the two-dimensional imaging in the previous chapter is required. The design and operation of the beamformer is discussed. Electrical, acoustic, and beamformer characterization is performed and reported. Finally, simple three-dimensional images taken using the row-column transducer are presented as a proof of concept.

The final chapter summarizes the results presented in the thesis and puts them into the overall context of the goals of the project. Specifically, the implication of the novel fabrication process and row-column beamforming method and their prospects of success are discussed. An outline of future work related to improving the fabrication process, transducer design, and other potential applications of CMUTs is given.

1.2 Motivation

The motivation behind the work in this dissertation is to develop a micro-electromechanical systems (MEMS) based ultrasound transducer that can be integrated into a standalone catheter based imager or combined with other imaging modalities, such as optical coherence tomography, into a single endoscope. This group has been developing MEMS and nano-devices for biological applications for a number of years; the work presented here is the first done in the field of ultrasound.

The ultimate purpose of this project is to develop small imaging transducers that are suitable for *in vivo* biological imaging applications. A potential application is to aid in the diagnosis and treatment of atherosclerosis, or the hardening and narrowing of the arteries. A primary complication of these plaques is when they rupture from the arterial wall. Blockages in the blood vessel are a common consequence and, depending on where the blockage occurs can lead to a stroke or myocardial infarction (heart attack). The occlusions can also lead to an aneurysm. The intravascular ultrasound (IVUS) systems available today use side-viewing transducers that help visualize the wall of the blood vessels as well as the plaques that line them [1]. Based on the acoustic properties of the plaques, its composition can be determined and the correct treatment applied [1]. The ultrasound beam is directed either mechanically or electrically within the blood vessel and typically slowly pulled out to image a length of the artery [2]-[3]. Forward and side looking high-frequency phased arrays would permit new imaging modalities and better quality imaging than what is commercially available now [4].

Higher frequency sound permits better resolution imaging; frequencies ranging from 20-40 MHz are commonly used with IVUS [3]. Electronic scanning of the acoustic beam (while keeping the transducer fixed in place) is viewed as the best way to generate high quality images quickly and reliably [5]-[6]. Mechanical motion tends to add artifacts to the image and slows image acquisition [7]. However, to achieve good quality images with electronic scanning the center-to-center distance

(pitch) between the elements that make up the array needs to be sufficiently small. This distance is determined by the frequency of operation of the transducer and scales linearly with frequency. Therefore, since high quality images require high frequencies, the element pitch needs to be small. It is challenging to make arrays with element dimensions suitable for high-frequency imaging with conventional piezoelectric fabrication techniques [6]-[7]. For this reason, transducers based on semiconductor microfabrication technology have been gaining interest since the early 1990s because they do not suffer this limitation. Using a semiconductor fabrication processes also permits tight integration to the driving electronic systems, shrinking the size and improving the performance of the transducer.

With a lack of ultrasound experience within the group, one of the goals of this thesis is to lay a foundation in ultrasonic transducers and imaging for future students to build upon. To do this, a method to easily and reliably make the transducers needs to be developed. Finding a novel way is one of the contributions of this thesis. A lot of time is also spent building and acquiring the tools necessary to characterize ultrasound transducers and have them operate as phased arrays. Volumetric imaging with purely electronic scanning requires a two-dimensional array of some type. The complexity of a full two-dimensional array is exponentially greater than that of a one-dimensional one. For this reason, a simpler scheme that has the potential to achieve good results is also explored.

1.3 Project Contributors

The results presented in this thesis have been obtained directly as a result of the author's efforts. This includes transducer design, development of the fabrication process, transducer characterization, beamformer design and assembly, image processing software, and analysis of the results. Understandably, plenty of help and advice is required when working on a project that covers such diverse disciplines. Outlined below are the significant contributions other individuals have made to the project.

- Mike Skvarla and many of the staff members at the Cornell Nanofabrication Facility provided the equipment training in the cleanroom. They were also instrumental in helping debug the fabrication process that was being developed.
- Bill Jolley and Ryan Norris were of assistance in the operation of the vector network analyzers used for some of the electrical testing of the CMUT devices.

- Training and insight into the wirebonding necessary to connect the electronic circuitry to the transducer was provided by Alireza Rezvani.
- Sangtak Park gave valuable direction and ideas about methods to build the pulsers and amplifiers needed to implement the custom-built beamformers.
- Some of the laborious optical and acoustic characterization was performed with the help of Lawrence Wong and Albert Chen.

Chapter 2 Ultrasound & CMUT Review

2.1 Introduction to Ultrasound

Ultrasound is typically defined as sound which has a frequency greater than that which is audible to an average human, around 20 kHz [8]. The use of ultrasound for diagnostic and medical purposes rose out of work done with underwater echo-ranging developed around the time of the First World War [9]. The effects ultrasound could have on living tissue was observed at that time, as the high power signals they were using caused schools of fish to die and float to the surface [10]. Ultrasound was first demonstrated for diagnostic purposes by Karl Dussik (Austria, 1937) who used it to measure acoustic attenuation in the brain [10].

In practice, the frequency of sound used in ultrasonic diagnostic tools is between 1 MHz and 60 MHz. Images or information is generated by emitting a pulse of sound and detecting an echo from that pulse. The time of flight as well as the strength and frequency components of the echo provides information about the depth and nature of a boundary within a medium being measured [3]. Collecting a series of these pulse-echo measurements over a volume allows a sub-surface image to be created. Usually, the same transducer is used to generate and receive the ultrasound signal.

Much like light, sound can be absorbed, scattered, refracted, and reflected. Absorption occurs within a medium and the latter three phenomena occur at an interface between two materials with different acoustic properties. Reflection and scattering are the properties typically used to gain information about the interior of a body while the other two cause a degradation of the signal. The quality of the echo signal depends on the depth of the boundary, the acoustic contrast of the boundary materials, and the smoothness of the boundary. The acoustic contrast is determined by the characteristic acoustic impedance of the two materials at the interface. Acoustic impedance is typically defined as

$$Z_L = \rho_0 c_L \tag{2.1}$$

where Z_L is the characteristic longitudinal impedance (fluids can only support longitudinal waves, unlike solids), ρ_0 is the density of the fluid, and c_L is the longitudinal speed of sound [11]. The units of acoustic impedance are the Rayl (defined as kg/m^2s, and named after Lord Rayleigh, an important figure in the development of acoustics). As a reference, water has an acoustic impedance of 1.48

MRayl. The amplitude reflection factor (*RF*) is the ratio of the amplitudes of the reflected beam to that of the incident beam. For a plane wave perpendicularly incident on an interface between two media RF is given by

$$RF = \frac{Z_2 - Z_1}{Z_2 + Z_1} \tag{2.2}$$

It is clear from (2.2) that if the acoustic impedances of the two materials are equal then there is no reflection [11]. If they are not equal, some of the sound is reflected at the surface and some passes through into the adjacent material. The amplitude transmission factor is the ratio of the amplitudes of transmitted beam to that of the incident beam and is given by

$$TR = \frac{2Z_2}{Z_1 + Z_2} \tag{2.3}$$

Just like light, the angle of reflection is equal to the angle of incidence and the ultrasound passing through is refracted according to Snell's law or

$$c_2 \sin\alpha_1 = c_1 \sin\alpha_2 \tag{2.4}$$

where c_1 and c_2 are the speeds of sound of the originating medium and transmitted medium respectively, and α_1 and α_2 are the angles of incidence and the angles of refraction respectively [12]. A schematic of reflection and refraction at a smooth interface is given in Figure 2.1.

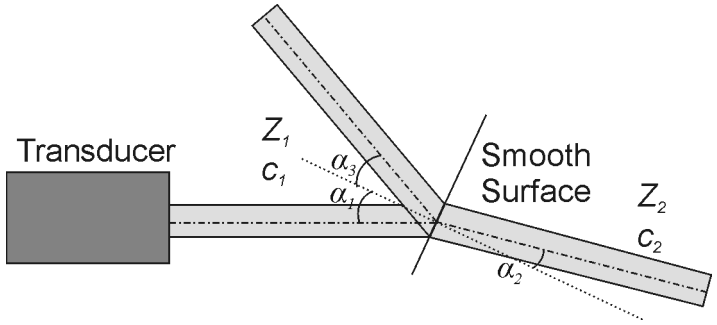

Figure 2.1: Schematic of the reflection and refraction of an ultrasound beam at a smooth interface between two fluids of difference acoustic impedance

2.2 Ultrasound Imaging

In the medical field, ultrasound imaging is a mature technology and is a commonly used diagnostic tool due to its relative low cost, efficacy, and potential portability. Other common imaging modalities are magnetic resonance imaging (MRI), X-rays, and computed tomography (CT) but each suffers drawbacks.

2.2.1 Other Imaging Modalities

X-ray imaging is a straightforward transmission method with an x-ray source on one side and an x-ray detector on the other side of the patient. Soft tissues cannot be distinguished well, but lungs and bones are well imaged. The use of ionizing radiation means that care much be taken to limit exposure, both at one time and cumulatively [13].

CT also uses X-rays, and exploits the subtle differences in x-ray absorption of different tissue types. In this case many images are taken from around the subject at many different angles. Computer algorithms are used to interpret the images and reconstruct the makeup of the volume based on the different absorption properties. The x-ray dose is higher with CT because many images are required. The machines also tend to be stationary since they need to be large enough to fit a person inside [13].

Magnetic resonance imagers measure the decay time of the precession of hydrogen atoms within the body. Applying a large static magnetic field causes the magnetic moments of the hydrogen nuclei to align with the field. A brief RF pulse is applied which causes the magnetic moments to oscillate (precess) around the static magnetic field. As the oscillations decay back to the steady state, radiation is given off that is measured. The decay time is dependent on the molecule in which the hydrogen atom is a part of. Using the decay time the system is able to reconstruct volume. Imaging is fast and safe however the machine is large and very expensive [13].

2.2.2 Ultrasound Imaging

Ultrasonic imaging systems are low cost compared to MRI and CT and do not use any ionizing radiation. There are no known deleterious biological effects from the acoustic fields at the power levels used for imaging [10], [13]. It can also operate at higher frame rates than the other imaging modalities which is important for monitoring fast moving organs such as the heart. The resolution attainable is inversely proportional to the frequency of sound and the aperture of the transducer. A

higher source frequency yields a better resolution in both the lateral and axial directions. A large bandwidth yields better axial resolution. Higher frequency sound is attenuated more efficiently by tissue which limits the depth that high-frequency ultrasound can be used for imaging. Attenuation also narrows the bandwidth of the sound as the higher frequency components are absorbed preferentially near the surface while the lower frequency components can pass deeper. Therefore the frequency must be chosen based upon the desired application and imaging depth [12]. Resolution can be improved by focusing the acoustic beam using a curved transducer, an acoustic lens, or a phased array (to be discussed in a later section). Similar to optics, a smaller focal spot can be obtained by using a transducer with a large aperture, a short focal length, and a short wavelength.

Ultrasound cannot be used to image bones and lungs *in vivo* because the acoustic impedance mismatch between them and the surrounding tissue is so great that almost all of the sound is reflected at the interface and very little penetrates. For this reason, acoustic windows are needed to image certain organs such as the heart, which is surrounded by the ribs and the lungs. For imaging done at the surface of the body frequencies in the range of 1 – 15 MHz are typically used to achieve a suitable depth [13]. For higher resolution images higher frequencies are needed and therefore the transducer needs to be closer to the imaging target. Endoscopic and catheter based transducers achieve this.

2.2.3 Phased Arrays

To achieve the best resolution some type of focusing of the ultrasound beam is needed. This is done using an acoustic lens, a geometrically curved transducer, or a phased array. An acoustic lens is the same in practice as an optical lens and is typically affixed to the transducer itself. The lens is made of a material with an acoustic impedance different from that of the medium. As sound reaches the curved lens-fluid interface it refracts toward a focus. Spherical and cylindrical lenses (which yield a line focus) are commonly used. Similarly, the transducer itself can be a given concave curvature which will focus the sound to a point or a line (depending on whether it is a spherical or cylindrical curvature). The drawback of focusing with a lens or a curved transducer is that the focal length and position is fixed with respect to the transducer. To generate a good quality image the focal spot needs to be scanned within the sample, meaning the transducer needs to be mechanically moved. Mechanical motion tends to degrade the quality of the image and reduce the acquisition rate [6]-[7].

It is for this reason that phased arrays are commonly used. The first published report of an angular scanning phased array for ultrasound imaging was reported by J. C. Somer in 1968 [15]. Commercial

real-time phased array imagers were available by 1980; made possible by advancements in microprocessors, memory, delay lines and miniaturization [15]. A phased array is a single transducer made up of many individually addressable elements. By coordinating the timing of firing, sound from each of them can be made to arrive at a single point in space, effectively mimicking a physical lens. Electronically focusing the beam using an array allows a user to arbitrarily and dynamically determine the focal depth and position.

The principal of phased array imaging is relatively straightforward. By offsetting the times the elements are fired in a coordinated manner, the acoustic beam can be directed and focused in different directions. In a one-dimensional array each element emits a cylindrical wave that travels at the speed of sound in the medium. By firing the outer elements before the inner elements in a precisely timed manner the wavefronts arrive at the focal point at the same time and interfere constructively. Away from the focal spot they interfere destructively. The result is a line focus. It is relatively easy to expand this idea to a two-dimensional array where the timing of all of the elements can be coordinated so that all of the acoustic pulses arrive at single point in space at the same time, instead of a line. Figure 2.2 illustrates the principal of focusing along the acoustic axis and along an angle of 25°.

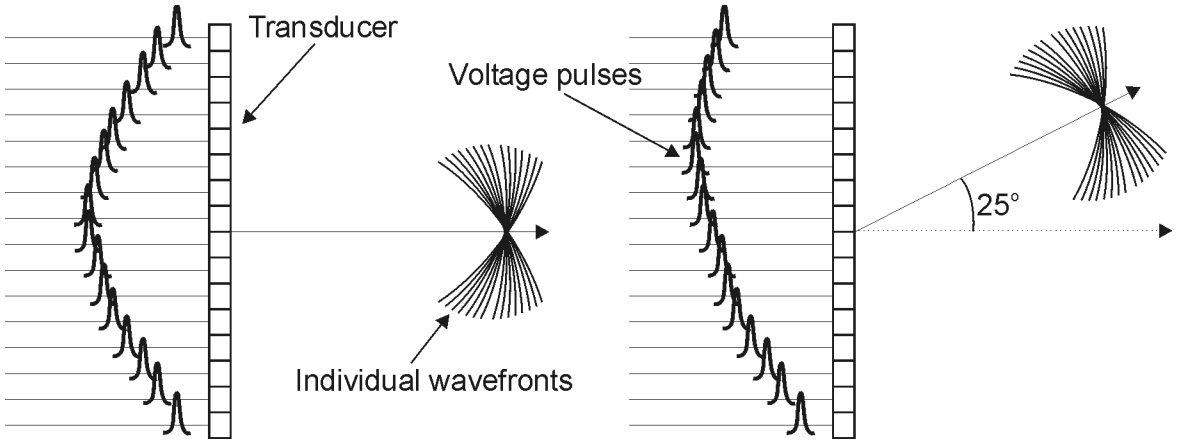

Figure 2.2: Schematic illustrating the principle of transmit beamforming. On the left, the timing of the voltage pulses is such that the wavefronts from each element reach the acoustic axis a given distance away at same time. On the right, the timing is adjusted such that the wavefronts converge a certain distance away at an angle 25° off the centre axis.

Receive beamforming is a similar idea. Sound from a point reflector will arrive at the different elements at different times depending on their distance from the reflector. By imposing the correct time delays on the signal received by each element, as seen in the top part of Figure 2.3, the signals

are summed coherently to achieve a large signal. At the same time, acoustic signals arriving from areas away from the receive focal point are effectively removed because the time delays applied by the receiver will not yield a coherently summed signal as seen in the bottom part of Figure 2.3. In effect transmit beamforming allows you to focus sound to one point (or line) in space, while receive beamforming allows you to listen to a single point (or line) in space yielding an excellent signal-to-noise ratio.

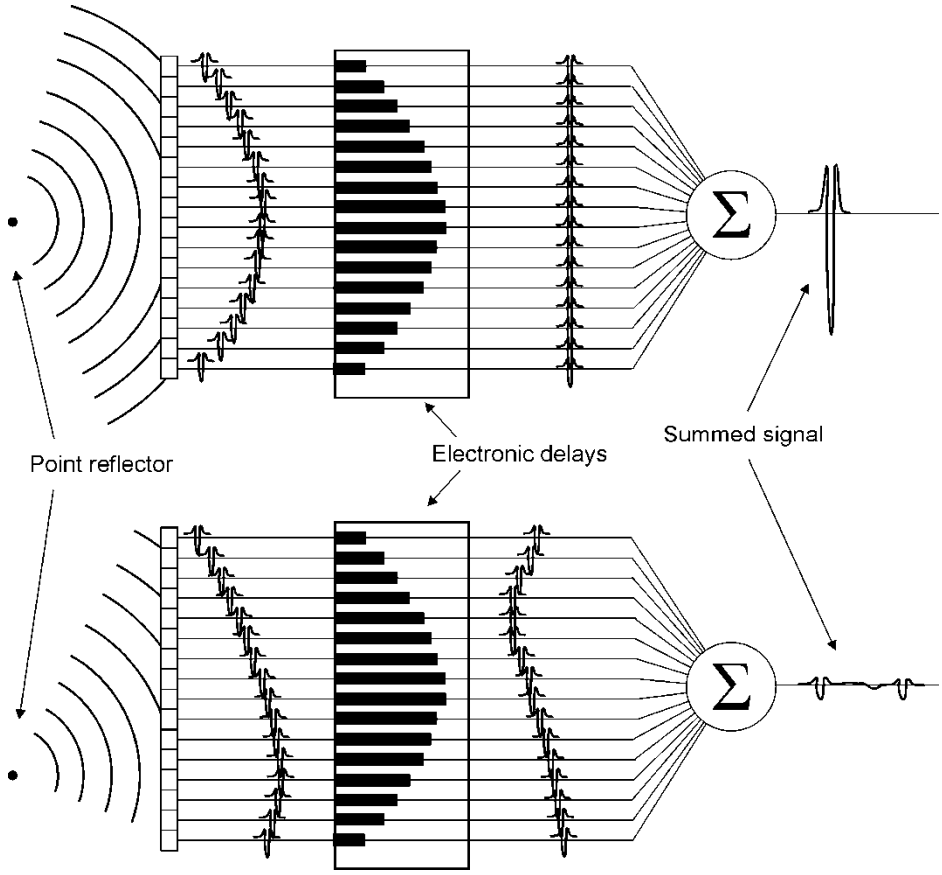

Figure 2.3: Schematic illustrating the principle of receive beamforming. Top – the point reflector is located directly in front of the transducer and the appropriate electronic delays are applied such that signal from each element is added coherently and the amplitude of the receive beamformed signal is large. Bottom - the point reflector is located at an angle to the transducer but the same delays as above are applied. The delays do not correctly compensate for the signal distribution on the elements. The result is a largely incoherent summed signal with a low amplitude.

Because of the ratio of the wavelength to the aperture the beam is not quite as contained as it is for something like a laser. In a one-dimensional array each element emits a cylindrical wave that radiates out into 180°. At the focal point the peaks from each element arrive at the same time yielding

a large amplitude. If the element pitch is too large, however, the same constructive interference can occur elsewhere in the field. These are called grating lobes and arise where the propagation delays of neighboring elements are equal to one period. The signals to do not arrive at the same time but they are still in phase. This can be avoided if the element pitch is set to one-half of the wavelength [16]. This satisfies the Nyquist sampling theorem. The wavelength of sound is given by

$$\lambda = \frac{c_L}{\upsilon} \tag{2.5}$$

where λ is the wavelength, c_L is the speed of sound in the medium and υ is the frequency. At high frequency such as 40 MHz the wavelength in tissue is ~39 μm. The element pitch then needs to be less than 20 μm to avoid grating lobes. This is difficult to achieve using the traditional dice-and-fill process and is one of the primary reasons fabricating high frequency phased arrays is so difficult with conventional piezoelectric fabrication techniques [6], [17]. In practice, a large bandwidth can significantly reduce the amplitude of any grating lobes that may be present when the element pitch does not satisfy the Nyquist criteria. A very broadband signal will consist of little more than a single oscillation of the pressure wave. In this case, if the signal from a neighboring element arrives one period later there is nothing for it to interfere with meaning there can be no constructive interference.

The necessary delays are relatively easy to calculate as they arise from the differences in time of flight between the elements. A schematic of the geometry used to calculate the delays is shown in Figure 2.4. The distance from the centre of the array to the target is *r*. The distance from the centre of the array to the element of interest is *x*, and the distance from the element of interest to the target is *r'*. The value of *r'* is given by

$$r' = \sqrt{x^2 - 2r\sin\theta + r^2} \tag{2.6}$$

The time of flight difference between the centre of the array and the element of interest is given by

$$\Delta t = \frac{r' - r}{c_L} \tag{2.7}$$

In this case, the element of interest should be fired Δt after the middle of the transducer is triggered. The delays for receive beamforming are calculated in the same manner.

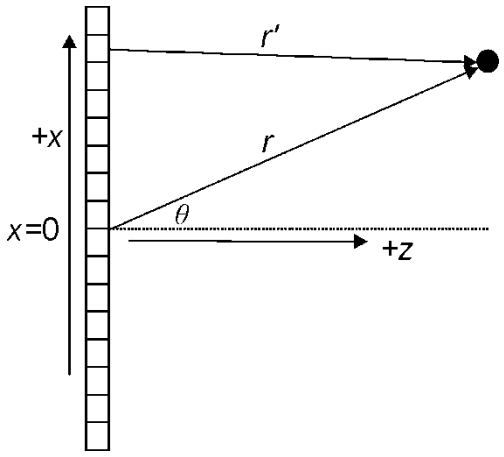

Figure 2.4: Schematic illustrating how the time delays for beamforming may be determined.

2.3 Piezoelectric Transducers

In essentially all commercially available ultrasound imaging system the transducer is a piezoelectric crystal. Piezoelectric crystals experience a strain when an electric potential is applied across them. Applying a voltage pulse to the crystal will cause it to expand and contract yielding a pressure wave into the surrounding medium. Conversely, an incoming pressure wave will cause strains in the crystal which are converted back into a potential and can in turn be amplified and measured. The most common material used for medical transducers is the ceramic polycrystalline lead-zirconate-titanate (PZT) [18]-[19].

Piezoelectric materials generate large amplitude ultrasound power when operating at or near the resonant frequency. Care must be taken to ensure the dimensions correspond well to the desired frequency. The resonant frequency is governed principally by the thickness of the piezo layer, thereby limiting a given element to operation around a single frequency [20] .

Despite their ubiquity there are some drawbacks to using piezoelectric materials. One is that the acoustic impedance of the transducer is significantly higher than that of the medium. A typical transducer may have an acoustic impedance around 30 MRayl, while that of air is ~400 Rayl, and water is 1.5 MRayl [21]-[22]. In both cases impedance matching layers are required to ensure adequate energy is coupled into the medium. Similarly, to dampen the resonance and minimize a long ring down time, a backing layer is needed [20]. The long ring down narrows the bandwidth of the acoustic pulse and this in turn decreases the axial resolution. Typical bandwidths achieved with PZT transducers are in the range of 70-80% [23].

Given the relationship between frequency and element pitch in phased arrays, there can be tight tolerances when high frequency one- or two-dimensional element arrays are fabricated. To make an array using piezoelectric crystals a layer of the material is deposited and then each individual element is diced either mechanically or using a focused laser to electrically isolate it from its neighbour and the cut is filled with an insulating material [5], [19], [24]-[25]. When using a transducer at 40 MHz the element pitch needs to be less than 20 μm when one assumes a speed of sound of 1540 m/s (the assumed speed of sound in tissue). Making cuts narrow enough to not significantly reduce the active area of the element is quite challenging as blade widths are typically greater than 15 μm. This is especially true with two dimensional arrays where most of the active area would be lost to the cuts. Even at lower frequencies the tight tolerances of dicing can significantly impact uniformity [19]. There is, of course, ongoing work to address this issue using techniques such as kerfless arrays [17], [26], and interdigital pair bonding [27]

2.4 Introduction to CMUTs

The initial demonstration of an electrostatically actuated transducer to generate and receive sound occurred in the late 19th century (~1880) by Edison and Dolbear [28]. The idea eventually caught hold with the development of a reliable condenser microphone shortly after the First World War. In its most basic construct it amounts to a capacitor where one of the electrodes is flexible and moves with the application of an electrostatic field. One of the primary issues that limited its application in the field of ultrasound is that high electric fields (tens to hundreds of MV/m) are required for efficient transduction. This can be achieved by applying large voltages, or more conveniently, by having the electrodes of the capacitor very close together. Routinely and uniformly achieving the micron or sub-micron separation levels needed can be quite difficult to reliably achieve using conventional fabrication techniques. With the advancement of semiconductor fabrication technologies, where thicknesses of tens of nanometers and below are routinely handled, this obstacle was removed. Ultrasonic transducers based upon electrostatic forces have been subject to increasing interest since the mid 1990s [29]-[32]. Termed capacitive micromachined ultrasonic transducers or CMUTs, the basic unit (or cell) consists of a membrane (more like a thin plate) suspended over a shallow cavity with a fixed electrode at the bottom and a patterned electrode on top of the membrane.

2.4.1 Fundamentals of Operation

The actuation of a CMUT is fairly similar to a piezoelectric transducer except that a DC bias is applied in addition to the transient voltage signal. In transmit mode, a DC bias is applied across the capacitor and then subject to a short voltage pulse causing a deflection of the membrane toward the other electrode. The membrane vibrates with the release of the electrostatic force and some of the energy is coupled into the surrounding media as pressure waves. In receive mode the capacitor is also DC biased which charges the electrodes. The incoming pressure waves cause the membrane to vibrate, changing the capacitance of the cell which in turn causes a current. This can be understood through the relationship between capacitance (C), charge (q), and voltage (V)

$$C = \frac{q}{V} \tag{2.8}$$

The potential is fixed due to the applied DC bias, as the capacitance changes with membrane movement q must change as well. A change in charge on the capacitor with time means, of course, there is a current.

The individual cells of a CMUT are usually quite small, less than100 μm in diameter. As a result many of them are needed to generate significant acoustic pressure. A single transducer for phased array imaging is made up of many individually addressable elements (typically anywhere from 16 to 256 in a one-dimensional array). Each element is in turn made of many individual cells which are connected and driven in parallel. The general design of a CMUT cell is shown in Figure 2.5. The bottom electrode is usually common to all of the elements (in a one-dimensional array) and the signals to individual elements are applied via the top electrodes. The DC bias is applied to either the top or bottom electrode.

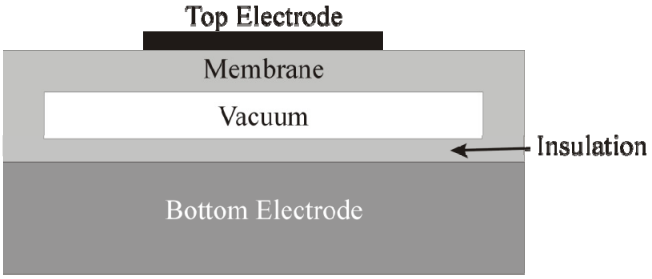

Figure 2.5: General schematic of a CMUT cell

2.4.2 CMUT Background

Over the past ten years there has been much work done with CMUTs in terms of fabrication methods, element design and device implementation. The fabrication process has moved from a purely surface micromachining process that involves sacrificial release to including a fusion bonding method that reduces design restriction, simplifies fabrication while also increasing the active area of the device [33], [34]. This fabrication processes will be discussed in greater detail in Section 2.5. High frequencies have been demonstrated, 60 MHz in air and 45 MHz in immersion [35]. Groups have demonstrated *in vivo* imaging using CMUT transducers, which in some cases have generated a better image than a traditional piezoelectric transducer [23], [36]. Work on two-dimensional arrays has also yielded promising results with three-dimensional imaging having been demonstrated [37]-[40]. Ring array with a reduced element count that demonstrate the ability to generate three-dimensional imaging have also been shown [41]-[42]. Ring arrays are well suited to catheter applications as they can be mounted at the distal end and the guide wire or other diagnostic equipment (such as an angioplasty balloon) can be passed through the middle.

There has also been a drive to incorporate the necessary electronics much closer to the transducer itself to improve system performance and simplify the connections between the transducer and the image processing system. The integration is done either by fabricating the CMUT devices directly on a CMOS circuit [32], [43]-[44] or with through-wafer vias and flip-chip bonding the CMUT array onto a separately fabricated circuit [45]-[47]. Putting the CMUT array directly on-top of CMOS electronics puts a strict thermal budget on the fabrication process, limiting the maximum temperature to around 400°C which restricts some fabrication options[48]-[49]. Putting electrical leads through the CMUT array substrate requires fewer compromises when fabricating the devices however putting a conductive conduit through the bulk of an entire wafer with a sufficiently small diameter so that it does not take up a large proportion of an element area can be challenging. Much work has also been put into miniaturizing the application specific integrated circuits necessary to drive CMUTs in a catheter or endoscope [41].

Beyond imaging applications, CMUTs have been explored for use in high intensity focused ultrasound (HIFU) for use in the targeted killing of cells [50]-[51]. In one case, an imaging transducer coexisted on the same substrate as the ultrasound [50]. CMUTs have been used as mixers for lab-on-a-chip experiments [52], as a hydrophone array for the calibration of other transducers [53], as a fluid property sensor [54], and as a chemical sensor where the surface of the CMUT is covered in a

chemical that adsorbs the molecule being measured [55]-[56]. The change in mass modifies the resonant frequency of the transducer. A CMUT has been used as the acoustic receiver for photo-acoustic imaging [57].

2.5 Fabrication Methods

When CMUTs were first developed they were fabricated using a sacrificial release surface micromachining technique. This carried on for well over a decade until Huang *et al* reported on a new technique that uses two wafers fusion bonded together to create the cell cavity [33]. It is fairly accurate to say that all CMUT fabrication is done using one of these two techniques. There have been some modifications reported with the sacrificial release (polyMUMPS process [58], or building from the bottom up [59]-[60]) and fusion bonding process (such as using silicon nitride as the membrane layer [61]-[62], LOCOS [63], or using anodic bonding instead of fusion bonding [64]). In the next two sub-sections the basic steps of both types of fabrication will be detailed as well as some of the benefits of the fusion bonding process.

2.5.1 Surface Micromachining Method

There is some variation in the reported methods of using the sacrificial release process in terms of materials used but a standard fabrication process can still be described [65]. The process begins with a conductive silicon wafer which acts as the common bottom electrode for the entire transducer. In the first processing step, the insulation layer is deposited. It also acts as the etch stop layer during sacrificial release (Figure 2.6(a)). Next, the sacrificial material is deposited; examples of materials used are chrome and polysilicon (Figure 2.6(b)). This is sometimes deposited in two steps so that the height of the etch channels is less than that of the cell cavities. This requires extra photolithography, etch and deposition (second sacrificial material) steps (Figure 2.6(c)). By lowering the height of the etch channels they become easier to seal at the end of the fabrication process. The cell cavities and membrane shape are then patterned into the sacrificial layer using a photolithography step (Figure 2.6(d)).

The first part of membrane layer is then deposited (Figure 2.6(e)). The membrane is typically low-stress silicon nitride, but doped polysilicon is used sometimes as well. The membrane is deposited in two steps because the membrane material is also used to seal the etch channels. Lithography is used to pattern the etch channels (Figure 2.6(f)). The sacrificial material layer is then

removed using wet chemistry (Figure 2.6(g)). This step can take a while (several days) due to the small channels available for the etchant to get into the cavity. The etch cavities are then sealed with the same material as the membrane (Figure 2.6(h)). The total membrane thickness is the sum of the sealing step and the initial membrane deposition step. The sealing is typically done with low-pressure chemical vapour deposition (LPCVD) so that the cell cavities are close to vacuum. Sealing is necessary to ensure that fluid does not enter into cavity. A vacuum, as opposed to air, reduces squeeze film damping during actuation and improves efficiency.

The next step establishes the bond pads for the bottom electrode using a photolithography and dry etch step. Finally the top electrodes and contact pads are deposited and patterned using a lift off metal process (Figure 2.6(i)).

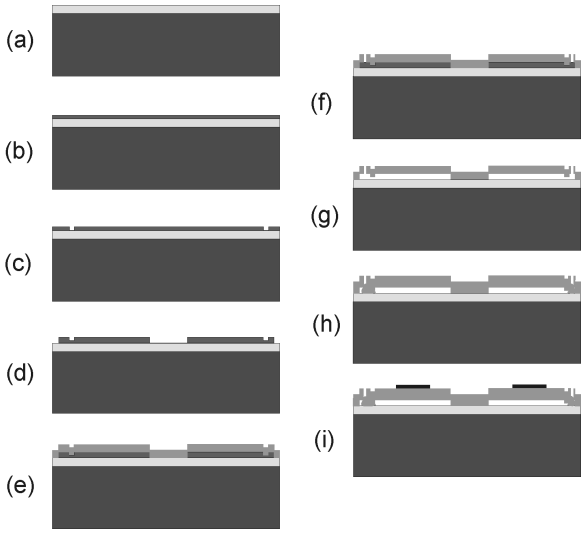

Figure 2.6: Basic process steps for the sacrificial release. (a) deposition of insulation/etch stop layer. (b) first deposition of the sacrificial layer. (c) etch sacrificial layer to define etch channels. (d) deposit second layer of sacrificial release material and define cell cavities and membrane. (e) deposit first layer of membrane material. (f) open etch channels. (g) release membranes. (h) seal etch channels. (i) expose bottom electrode for contact pads (not shown), metalize top electrodes and contact pads.

2.5.2 Fusion Bonding Method

Compared to the surface micromachining process, the standard fusion bonding process is very straightforward. It was first reported by Huang *et al* in 2003[33]. The process begins with two wafers, one a highly doped silicon wafer which will serve as the common bottom electrode, the other a silicon-on-insulator (SOI) wafer of which the device layer will serve as the membrane. The device layer is either intrinsic silicon or it is highly doped. The first step of the process is growing a layer of

thermal silicon dioxide (Figure 2.7(a)). This will serve as the insulation layer and sidewalls of the CMUT cells. The cell cavities are defined photolithographically and etched using a dry etch (Figure 2.7(b)). Next the two wafers are cleaned and bonded together in a wafer bonder under vacuum (Figure 2.7(c)). The bonded pair is then annealed at an elevated temperature (~800-1000°C) to significantly strengthen the bond. The handle portion of the SOI wafer is removed by a combination of grinding and wet etching. The oxide layer is removed with a buffered oxide etch (Figure 2.7(d)).

The second photolithography step defines the bottom electrode contact pads (Figure 2.7(e)). This is followed by metallization of the contact pads and top electrode (if the membrane is not sufficiently doped) (Figure 2.7(f)). The final step etches through the membrane defining the individual elements (Figure 2.7(g)). This is to ensure the elements are electrically isolated from one another.

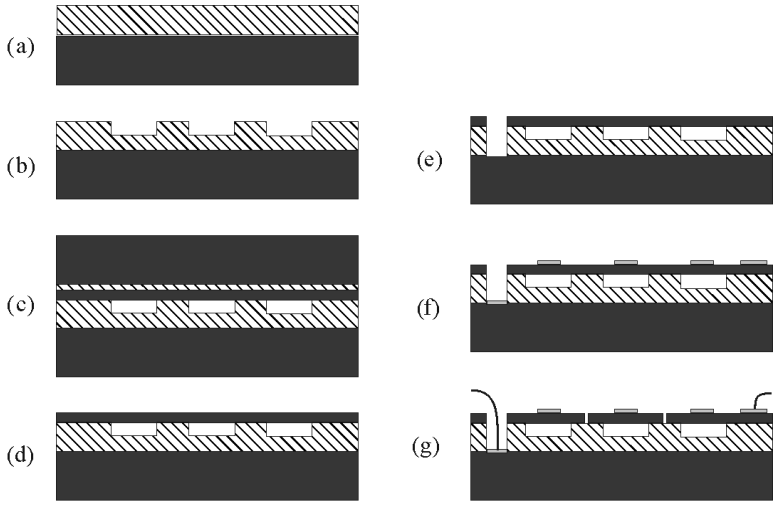

Figure 2.7: Process flow for a typical fusion bonding process. (a) growth of thermal oxide for insulation and cell side walls. (b) etching the cell cavities. (c) fusion bonding the SOI wafer to the bottom wafer, then annealing. (d) release the membrane by grinding and wet chemistry. (e) expose the bottom electrode contact pad. (f) metalize the contact pads and top electrodes. (g) silicon etch to electrically isolate each element from one another.

2.5.3 Advantages of Wafer Bonding Process

There are a number of advantages the silicon fusion bonding process has over the sacrificial release process. The primary one is the much simpler fabrication process. Only four masks are used and there are only two deposition steps in the entire process. An individual can complete the process in less than a week.

The thickness of all the layers is very well controlled because the thermal oxide growth is very uniform and the device layer of the SOI wafer is also very well controlled when it is purchased from the manufacturer. The exclusive use of dry etching steps also aids in maintaining control of the fabrication process.

Also, without the need for sacrificial release channels the cells can be packed closer together improving the fill factor and therefore the sound generating capability of the transducer. This lack of etch channels is also important for high frequency transducers where the elements are very small and space is at a premium. Another benefit of not using a sacrificial release is that stiction is not an issue. Stiction is a common problem with sacrificially released devices and occurs when the surface tension of the fluid in the cavity brings the top and bottom of the cell together and holds it together [65]. This effect sets some limits on the size and thickness of membranes that may be used for CMUTs fabricated using the sacrificial release process.

A final advantage is that by using a wafer bonder to bond the two wafers together it is easy to achieve a very good vacuum. Pressures in the sub μbar regime are readily achievable and the seal is hermetic.

2.6 CMUTs as an Imaging Technology

There are a number of reasons why CMUTs may end up being the transducer of choice for ultrasound imaging applications. There are however also several issues that need to be addressed before that is the case.

2.6.1 Advantages

The primary advantage of CMUTs over piezoelectric technology is the way they are fabricated, specifically with respect to high frequency transducers and two-dimensional arrays. Using photolithography to define the layout of the elements on a transducer makes it easy to accurately, and repeatedly manufacture arrays with arbitrary layouts and sizes. Microfabrication techniques can readily achieve sub-micron feature sizes, which is more than adequate for ultrasound imaging transducers. This is important for high frequency and two-dimensional arrays because the element sizes can be quite small, and reliable fabrication using the conventional dice-and-fill techniques used for piezoelectric transducers is not easy. Beyond being able to easily realize small feature sizes,

semiconductor processing techniques are also able to achieve high levels of parallelization such that hundreds or thousands of devices can be fabricated simultaneously. Once large scale fabrication is reached, the cost per transducer is driven significantly down by this parallelization.

A second advantage is that integration with the drive electronics necessary for imaging is more straightforward with CMUTs than piezoelectrics. The tight integration and miniaturization of the whole imaging assembly is important for endoscope and catheter based imaging where size and electrical optimization is critically important. This integration can be done via flip-chip bonding, or by directly building the CMUTs on top of a CMOS circuit.

A third advantage is the broad bandwidth of CMUTs. A large bandwidth corresponds to a short temporal pulse; this in turn means better depth resolution. Typical -6 dB fractional bandwidths achieved with piezoelectric transducers is 70-80% [23], for CMUTs bandwidths in excess of 100% are common. This is because of the low mass of the transducer membrane, the fluid quickly damps out the oscillations. Beyond improving axial resolution, the broad bandwidth may also be useful for harmonic imaging. In harmonic imaging, insonifying a target with ultrasound of frequency f induces emission at a frequency of $2f$ [66]. This reduces clutter in the image since the second harmonic is only generated at the target. In practice the transducer needs to be able to efficiently generate the fundamental frequency and be sensitive to the second harmonic [69]. The bandwidth of CMUTs would make them suitable for this application however because the electrostatic force is approximately proportional to the square of the potential, harmonics are generated [67]. Separating the tissue generated signal from the transmitted one is a challenge. Pre-compensation of the transmit waveform has been shown to be able to reduce the transmitted harmonics [68].

2.6.2 Disadvantages

There are few areas where CMUTs do not perform as well as piezoelectric transducers. The first is that the transduction efficiency of CMUTs is not as high as that of piezoelectric transducers [23]. This impedes the ability to image deep within a sample as the launched power is not as high and the ability to detect weak signals is diminished.

A second disadvantage is the relatively high levels of acoustic crosstalk between the elements of the transducer. While much of the energy is launched into the medium, some energy is transferred to the bulk silicon substrate as Lamb waves and some as Stoneley waves that are carried along the membrane-fluid interface [69]-[70]. This is important in phased arrays because the speed sound

travels in these two modes means the acoustic energy can interfere with adjacent elements that are being fired at a delayed time. This can result in changes in the emitted field pattern that negatively impact imaging performance. Much research has gone into mitigating this problem in CMUTs from etching cuts into the membrane [71], thinning the substrate [71]-[72], lossy layers on the top and bottom of the CMUT [70], [73]-[74], as well has modifying the transmit pulse to cancel the surface waves [68].

Another large potential drawback is the problem of dielectric charging. This, as the name suggests, is when charges get trapped in the dielectric layers and alter the performance of the transducer. Dielectric charging is a common issue for electrostatically actuated MEMS devices as the large electric fields can force charges into insulating materials [75]-[76]. Charging has a negative effect on the reliability of the transducers as the operating point changes with time. In the case of CMUTs, the bias voltage needs to be increased over time to achieve the same output pressure as charges trapped in the insulation layer mask a portion of the bias [65], [77]. The effect can be counteracted by reversing the polarity of the bias, but this is clearly not a desirable solution. Some work has gone into mitigating this problem, in one case posts were fabricated within the cavity instead of a uniform dielectric layers. This prevents a short circuit if the membrane collapses but provides less area for the charges to be trapped [77]. Results presented in Chapter 4, report a CMUT device that does not appear to suffer from the problem of dielectric charging.

Chapter 3 Equivalent Circuit Model of a CMUT

As with any engineered system it is necessary to have a model that can accurately describe it. In the case of MEMS, finite element method (FEM) simulations are a commonly used tool used to design and analyze devices. This is no different in the case of CMUTs. The problem with numerical based solutions, like FEM simulations, is that it frequently takes a long time to obtain a result and when trying to arrive at a final design iteratively the time cost can be great. Also, one must be careful when using commercial FEM packages, the results can be erroneous if care is not taken. For that reason it is good to have a simple analytical model that may be less accurate but is typically much quicker to solve and can give a reasonable solution.

The standard method used to analytically model an ultrasound transducer is derived from the Mason equivalent circuit model [78]. In it, the electrical and acoustical domains are coupled together by a transformer. The acoustic impedances are represented by electrical impedances in the model and various parameters of the system can be determined. Many variations of this and other models for CMUTs have been advanced in the literature in an attempt to improve the accuracy and reduce complexity [79]-[87]. However, accurately modeling an array of thin plate flexible capacitors connected in parallel with different sized electrodes subject to strong fluid damping and excited by transient signals is challenging. This is the case without taking into account there are many coupled interactions between the cells through the substrate, the membrane, and the fluid. For this reason the modeling work done for this thesis is of a first order nature suitable for estimating the resonant frequency, collapse voltage and impedance of a CMUT.

3.1 First Order Model

A first order model of a CMUT can provide some insight into its operation under static bias. Here we will assume that the deflection is relatively small and use a parallel plate approximation. Under static equilibrium the sum of the forces acting on the membrane is described as:

$$F_{mass} + F_{capacitance} + F_{mechanical} = 0 \tag{3.1}$$

where F_{mass} pertains to the mass of the membrane, $F_{capacitance}$ is the force associated with the electrostatic attraction between the two plates and $F_{mechanical}$ is the restoring mechanical force of the

membrane. F_{mass} is simply the mass times acceleration and $F_{mechanical}$ will be approximated with a linear spring with a restoring force of $-ku$. We can define the capacitance of the system as:

$$C = \frac{\varepsilon A}{d_0 - u(x,t)} \tag{3.2}$$

where ε is the dielectric permittivity of the medium between the plates, A is the area of the plates, d_0 is the distance between the plates with no applied potential and $u(x,t)$ is the displacement of the membrane under an applied potential. The energy stored in the capacitor is

$$E = \frac{CV(t)^2}{2} = \frac{\varepsilon A V(t)^2}{2\left(d_0 - u(x,t)\right)} \tag{3.3}$$

and the force is defined as

$$F_{capacitance} = -\frac{dE}{du} = \frac{\varepsilon A V(t)^2}{2\left(d_0 - u(x,t)\right)^2} \tag{3.4}$$

Substituting the force expressions into equation (1) yields

$$\begin{aligned} ma + \frac{\varepsilon A V(t)^2}{2\left(d_0 - u(x,t)\right)^2} - ku(x,t) = 0 \\ m\frac{d^2u(x,t)}{dt^2} + \frac{\varepsilon A V(t)^2}{2\left(d_0 - u(x,t)\right)^2} - ku(x,t) = 0 \end{aligned} \tag{3.5}$$

If we consider only the case, than the first term of equation (3.5) disappears and we are left with

$$\frac{\varepsilon A V^2}{2\left(d_0 - u(x)\right)^2} = ku(x) \tag{3.6}$$

It is relatively straightforward to show that when the gap between the two plates is reduced by 1/3 of the original amount snap down occurs. By substituting $u=d/3$ into equation (3.6) it can be shown that the collapse voltage is

$$V_{collapse} = \sqrt{\frac{8kd_0^3}{27\varepsilon A}} \tag{3.7}$$

Another phenomenon that can be derived from the simple first order model is a spring softening effect that occurs due to the relationship between the capacitive and mechanical restoring forces. As an increasing DC bias is applied, the membrane deflects closer to the bottom electrode, it is opposed by the mechanical stress in the membrane but as it deflects the electrostatic force becomes stronger. This increase in force can be interpreted as a softening of the spring constant. This effect can be qualitatively examined by expanding the capacitive force in equation (3.4) in a Taylor series about the deflection depth u_{DC}, which occurs due to the bias voltage V_{DC}, and then substituting back into equation (3.5).

$$m\frac{d^2u(x,t)}{dt^2} + \frac{\varepsilon A V_{DC}^2}{2\left(d_0 - u_{DC}\right)^2} + \frac{\varepsilon A V_{DC}^2}{\left(d_0 - u_{DC}\right)^3}\left(u\left(x,t\right) - u_{DC}\right) - ku(x,t) = 0 \tag{3.8}$$

This can be rearranged to

$$m\frac{d^2u(x,t)}{dt^2} + \frac{\varepsilon A V_{DC}^2}{\left(d_0 - u_{DC}\right)^2}\left(\frac{1}{2} - \frac{u_{DC}}{d_0 - u_{DC}}\right) - \left(k - \frac{\varepsilon A V_{DC}^2}{\left(d_0 - u_{DC}\right)^3}\right)u(x,t) = 0$$

In the last set of brackets the value subtracted from the spring constant k effectively decreases the spring stiffness.

3.2 Transducer Model

A transmitting CMUT transforms electrical energy into mechanical energy. The reverse is true when using it as a receiver. This coupling between two forms of energy is the definition of a transducer. Fortunately, the equations governing the different domains contain many similarities. Hence, problems in the electrical domain can be converted to the mechanical domain and vice-versa with a moderate loss of generality. Care must be taken to ensure that any generalizations are appropriate. An equivalent circuit model for an electrostatic transducer has been derived by Hunt in [88]. A circuit diagram of the equivalent circuit is shown in Figure 3.1. This model has been cited extensively in the literature as a basis for analytical modeling [23], [90]-[94].

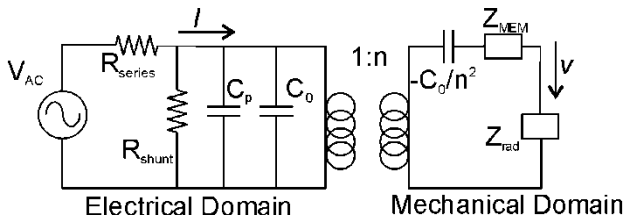

Figure 3.1: Schematic of the electrical equivalent circuit of an electroacoustic transducer.

The negative capacitance on the mechanical side is indicative of the spring softening effect. The value C_0 is the capacitance of the cell, R_{shunt} is associated with current leakage through the device (and is assumed to be infinite) and C_p is the parasitic capacitance between the top and bottom electrodes (assumed to be 0). The impedance Z_{rad} is the acoustic impedance of the immersion media. The transformer ratio, n, is the product of the device capacitance multiplied by the electric field across the gap [88].

$$n = \frac{C_0 V_{DC}}{d_0 - u_0} \tag{3.9}$$

The value d_0 is the initial gap between the electrodes, u_0 is the membrane displacement. It is clear that to maximize energy transfer from one domain to the other the value of n should be maximized; this can be done by operating the device close to pull-in.

3.2.1 Harmonic Diaphragm Displacement

In order to use the circuit model we must determine the mechanical properties of the circuit elements. This is done by solving for the displacement of a vibrating diaphragm. If we consider a circular diaphragm it makes sense to work in polar coordinates and we can assume that there is no dependence on θ. The response of a circular plate to a transverse harmonic excitation is given by Nayfeh [95] in polar coordinates as

$$\frac{Eh^3}{12\left(1-\upsilon^2\right)}\nabla^4 u - N_r\frac{\partial^2 u}{\partial r^2} - N_\theta\frac{1}{r}\frac{\partial u}{\partial r} - P + h\rho\frac{\partial^2 u}{\partial t^2} + 2c\frac{\partial u}{\partial t} = 0 \tag{3.10}$$

where E is Young's Modulus, N_r is the radial force (arising from residual manufacturing stresses), N_θ is the hoop force, h is the thickness, υ is Poisson's Ratio, ρ is the density of the diaphragm, c is the

damping coefficient and P is the pressure (either from the environment or a DC electrostatic pressure). The Laplacian operator is

$$\nabla^2 = \frac{\partial^2}{\partial r^2} + \frac{1}{r}\frac{\partial}{\partial r} \tag{3.11}$$

and the biharmonic operator is

$$\nabla^4 = \frac{\partial^4}{\partial r^4} + \frac{2}{r}\frac{\partial^3}{\partial r^3} - \frac{1}{r^2}\frac{\partial^2}{\partial r^2} + \frac{1}{r^3}\frac{\partial}{\partial r} \tag{3.12}$$

The radial and hoop forces are defined by Nayfeh as

$$\begin{aligned} N_r &= \frac{Eh^3}{1-\upsilon^2}\left(\varepsilon_r + \upsilon\varepsilon_\theta\right) \\ N_\theta &= \frac{Eh^3}{1-\upsilon^2}\left(\varepsilon_\theta + \upsilon\varepsilon_r\right) \end{aligned} \tag{3.13}$$

where ε_r is the radial strain and ε_θ is the hoop strain. Because the strains are purely tensile or compressive (as a result of the differences in thermal coefficients of expansion) the strains are purely radial and the value of ε_θ is 0. Frequently approximations are made that assume the diaphragm is a membrane and hence is very thin so the term with h^3 is assumed to go to 0, or that the diaphragm is relatively thick and there is no tension and hence the second term and third term of equation (3.10) goes to 0. In order to maintain generality we will assume a significant thickness and tension in the surface. We will also assume the harmonic steady state solution such that

$$u(t) = e^{j\omega t} \tag{3.14}$$

We can make some simplifications that make equation (3.10) more tractable. First, we will neglect the damping coefficient. This is reasonable because the damping will be dominated by the acoustic impedance into which the transducer is immersed, this will be added separately to the model. Squeeze film damping beneath the membrane will also not be an issue because the volume will be evacuated during the manufacturing process. Also, the terms N_r and N_θ will be considered equal, now just N. Evaluating equation (3.13) when there is no hoop strain, the hoop force is simply a factor of υ smaller than the radial force. So while the difference between the two values is greater than a factor of

two it is still reasonable to consider them equal because the behaviour of the membrane will be dominated by the plate stiffness. With the approximations made, equation (3.10) becomes essentially the same as that given by Mason in [78].

$$\frac{Eh^3}{12\left(1-\upsilon^2\right)}\nabla^4 u - N\nabla^2 u - P - \omega^2 h\rho u = 0 \tag{3.15}$$

Solving equation (3.15) we get

$$u(r) = AJ_0\left(k_1 r\right) + BJ_0\left(k_2 r\right) + CY_0\left(k_1 r\right) + DY_0\left(k_2 r\right) - \frac{P}{h\rho\omega^2} \tag{3.16}$$

where J_0 is a Bessel function of zero order of the first kind and Y_0 is a Bessel function of zero order of the second kind. We can immediately set the coefficients C and D to zero because a Bessel function of the second kind goes to negative infinity at $r=0$. The coefficients k_1 and k_2 are defined as

$$\begin{aligned} k_1 &= \sqrt{\frac{6N\left(\upsilon^2-1\right) + 2\sqrt{3\left(1-\upsilon^2\right)\left(3N^2\left(1-\upsilon^2\right) + \rho\omega^2 h^4 E\right)}}{h^3 E}} \\ k_2 &= \sqrt{\frac{6N\left(\upsilon^2-1\right) - 2\sqrt{3\left(1-\upsilon^2\right)\left(3N^2\left(1-\upsilon^2\right) + \rho\omega^2 h^4 E\right)}}{h^3 E}} \end{aligned} \tag{3.17}$$

Given that the diaphragm is fixed at the edges and has some rigidity we will assume the boundary conditions $u(a) = 0$ and $u'(a) = 0$ (where a is the radius of the membrane), that is the deflection and slope at the boundary is 0 along the edge of the membrane. Applying the boundary conditions to equation (3.16) we find the constants A and B are

$$\begin{aligned} A &= \frac{Pk_2 J_1\left(k_2 a\right)}{h\rho\omega^2\left(k_2 J_0\left(k_1 a\right)J_1\left(k_2 a\right) - k_1 J_0\left(k_2 a\right)J_1\left(k_1 a\right)\right)} \\ B &= \frac{Pk_1 J_1\left(k_1 a\right)}{h\rho\omega^2\left(k_1 J_0\left(k_2 a\right)J_1\left(k_1 a\right) - k_2 J_0\left(k_1 a\right)J_1\left(k_2 a\right)\right)} \end{aligned} \tag{3.18}$$

where J_1 is a Bessel function of the first order. So after some algebraic manipulation we find that the displacement of the membrane as a function of r is

$$u(r) = \frac{P}{h\rho\omega^2}\left[\frac{k_1 J_1(k_1 a) J_0(k_2 r) - k_2 J_1(k_2 a) J_0(k_1 r)}{k_1 J_1(k_1 a) J_0(k_2 a) - k_2 J_1(k_2 a) J_0(k_1 a)} - 1\right] \tag{3.19}$$

3.2.2 DC Displacement

In order to use equation (3.19) we must find an expression for *P*. While part of the pressure will be due to the static environmental pressure the rest will be from an applied bias potential. Here we will derive an expression for the displacement and hence the electrostatic force associated with a DC bias. Solving equation (3.15) with the time dependence set to 0 allows us to find the DC displacement. Going through essentially the same steps that were done above, we arrive at

$$\begin{aligned} k_{DC} &= \sqrt{\frac{12N(\upsilon^2 - 1)}{Eh^3}} \\ u_{DC}(r) &= \frac{P}{4N}\left[a^2 - r^2 + \frac{2a}{k_{DC} J_1(k_{DC} a)} \cdot \left[J_0(k_{DC} a) - J_0(k_{DC} r)\right]\right] \end{aligned} \tag{3.20}$$

Now to find the pressure, *P*, we need to know the electrostatic force between the two electrodes. Here we will use a parallel plate approximation, and neglect the fringing fields. The electrostatic force from a pair of charged plates is

$$F = \frac{d}{du}\frac{1}{2}CV^2 \tag{3.21}$$

Because the upper electrode is deposited on top of a dielectric membrane it is necessary to take into account the membrane when calculating the capacitance of the CMUT. The protective insulation deposited on top of the bottom electrode should also be taken into account. This geometry is equivalent to three capacitors in series with an effective capacitance of

$$C_{eff} = C_0 = \frac{\varepsilon_0 \varepsilon_i \varepsilon_m A_E}{\varepsilon_i h + \varepsilon_m t_i + \varepsilon_i \varepsilon_m (d - u_{ADC})} \tag{3.22}$$

where t_i is the thickness of the insulation layer, ε_i is the dielectric factor of the insulation layer, ε_m is the dielectric factor of the membrane material, d is thickness of the gap, A_E is the area of the top electrode and u_{ADC} is the average displacement of the membrane. Hence the electrostatic pressure is

$$P_{ES} = \frac{F}{A_M} = \frac{\varepsilon_0 \varepsilon_i^2 \varepsilon_m^2 V_{DC}^2}{2\left(\varepsilon_i h + \varepsilon_m t_i + \varepsilon_i \varepsilon_m \left(d - u_{ADC}\right)\right)^2} \tag{3.23}$$

If the membrane and insulating layer are made of the same material, equation (3.23) simplifies to

$$P_{ES} = \frac{F}{A_M} = \frac{\varepsilon_0 \varepsilon_i^2 V_{DC}^2}{2\left(\left(h + t_i\right) + \varepsilon_i \left(d - u_{ADC}\right)\right)^2} \tag{3.24}$$

Because the pressure in equation (3.24) depends on the displacement, u, the variable P should not be treated as a constant. However, it is substantially easier to solve the equation as a constant and then go back and substitute equation (3.24) into (3.20) and solve it iteratively so that the final displacement of the membrane is found. Once an equilibrium displacement is found the electrostatic force is known.

One can also try and take into account the curvature of the membrane by breaking up the round top electrode into a series of concentric ring electrodes and evaluating and summing the capacitance and force contribution from each. By iteratively using the displacement values found using equation (3.20) and substituting them for u_{ADC} in equation (3.24) the curvature can be taken into account. The pressure equation in this case is

$$P = \frac{1}{A_M} \sum_k \frac{\varepsilon_0 \varepsilon_i^2 V_{DC}^2 r_k \Delta r}{\left(\left(h + t_i\right) + \varepsilon_i \left(d - u_k\right)\right)^2} \tag{3.25}$$

where r_k is the radius of the rth ring, Δr is the width of the ring and u_k is the vertical displacement of the kth ring. A plot of the displacement of the membrane using both the average displacement method and the piecewise method, where the membrane is broken up into concentric rings, is given in Figure 3.2. For the simulation, the Si_xN_y membrane has a diameter of 22 μm, is 400 nm thick and has an insulation layer thickness of 260 nm and a cavity depth of 140 nm (physical dimensions are the same as the first generation devices presented in Chapter 4). Clearly breaking the cell into a series of concentric rings impacts the calculated displacement. This model still assumes that there is no fringe field. The fringe field appears to be significant since the top electrode has a diameter of 14 μm and the bottom electrode is the full 22 μm. A capacitance simulation with no bias voltage in Coventor yields a capacitance about 15% larger than that obtained with equation (3.22).

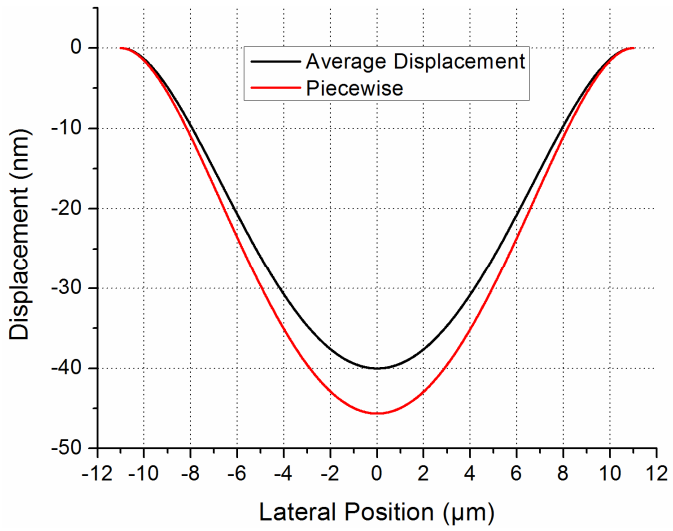

Figure 3.2: Plot of the simulated displacement of a Si_xN_y membrane with a 50 V bias voltage using the average displacement method and the piecewise displacement method.

3.2.3 Derivation of Transducer Impedance

Going back to the equivalent circuit; the impedance in the mechanical domain is defined as the force divided by the velocity or

$$Z_{mem} = \frac{F}{\bar{v}} = \frac{P \cdot A_M}{\bar{v}} \tag{3.26}$$

where A_M is the area of the membrane and $\bar{v}$ is the average velocity of the membrane and is found by taking the time derivative of (3.14). We will again assume harmonic time dependence so the velocity is simply

$$v = j \cdot \omega \cdot u(r) \tag{3.27}$$

where $u(r)$ is given in equation (3.19). To find the average velocity of the membrane we must integrate over the surface.

$$\bar{v} = \frac{1}{\pi a^2}\int_0^a \int_0^{2\pi} j\omega u(r) r\, d\theta dr$$
$$= \frac{jP}{h\rho\omega}\left[\frac{2\left(k_2^2 - k_1^2\right)J_1(k_1 a)J_1(k_2 a)}{ak_1k_2\left(k_2 J_1(k_2 a)J_0(k_1 a) - k_1 J_0(k_2 a)J_1(k_1 a)\right)} - 1\right] \quad (3.28)$$

Substituting (3.28) into (3.26) and doing some algebraic manipulation we get

$$Z_{mem} = jh\rho\omega A_M\left[\frac{ak_1k_2\left[k_2 J_1(k_2 a)J_0(k_1 a) - k_1 J_1(k_1 a)J_0(k_2 a)\right]}{ak_1k_2\left[k_2 J_1(k_2 a)J_0(k_1 a) - k_1 J_1(k_1 a)J_0(k_2 a)\right] - 2J_1(k_1 a)J_1(k_2 a)\left[k_2^2 - k_1^2\right]}\right] \quad (3.29)$$

A plot of the mechanical impedance of a membrane is illustrated in Figure 3.3.

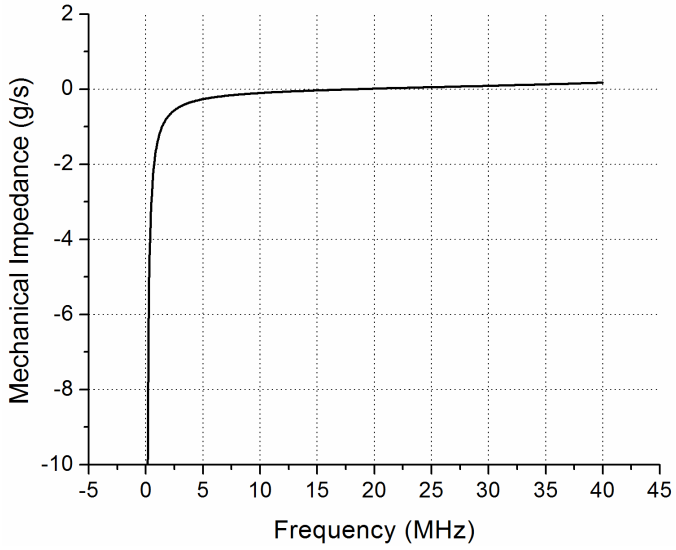

Figure 3.3: Imaginary component of the mechanical impedance for a 22µm diameter Si_xN_y membrane. The zero crossing corresponds to the resonant frequency of the membrane.

With Z_{mem} known we can substitute it into our equivalent circuit diagram and solve the electrical system to determine the resonant frequency of the system. A plot of the input impedance of the equivalent circuit is given in Figure 3.4. The physical properties of the individual cells are the same as used previously in this section. Since an element in one of the fabricated devices consists of 4100 cells in parallel the equivalent circuit of the element would consist of 4100 of the equivalent circuits seen in Figure 3.1. The radiation impedance in the model was set for air. The specific acoustic

impedance is defined by Szabo [96] as

$$Z_L = \rho c A_M \tag{3.30}$$

where ρ is the density of the medium, c is the speed of sound in the medium and A_M is the area of the membrane. Using the impedance in this manner is a reasonable approximation when the membrane dominates the impedance. It has been shown that it is not particularly accurate when the radiation impedance dominates the membrane impedance [97].

3.2.4 Comparison of Model to Experimental Results

For each of the different types of devices fabricated the resonant frequency and collapse voltage are calculated using the equivalent circuit model discussed previously. These are then compared to the results obtained from experiments (discussions of the experiments and device dimensions are included in the subsequent Chapter 4, 5, and 6). The results are presented in Table 3-1. The material constants are taken from CoventorWare simulation software. The density of silicon nitride is taken as 2700 kg/m^3, Young's modulus, 254 GPa and Poisson's ratio 0.23. The static pressure without a DC bias is assumed to be atmospheric (100 kPa). The piecewise method (described in section 3.2.2) is used to calculate the capacitance and the transduction coefficient n.

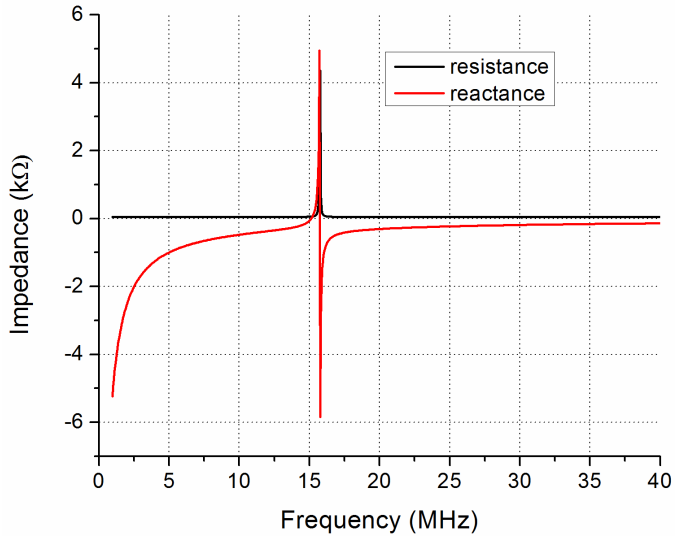

Figure 3.4: Calculated real and imaginary impedance of a 4100 cell element biased at 50 V. The calculated resonant frequency is 15.6 MHz.

Table 3-1: Summary of results comparing the equivalent circuit model to experimental results

	Resonant Frequency Model (MHz)	Resonant Frequency Experiment (MHz)	Collapse Voltage Model (V)	Collapse Voltage Experiment (V)
First Gen Device	18.0	14-17	63	45-55
1D – Low Freq	15.7	14-16	80	70-80
1D – High Freq	43.2	38	230	180
2D – Low Freq	16.8	14-16	80	60-80
2D – Med Freq	31.5	28	158	120

It is clear from the results that the DC displacement model and equivalent circuit model over estimate the collapse voltage by 20-30%, and the resonant frequency by 5-20%, respectively. Beyond the fact this is a first-order model there are few other reasons for the discrepancy between modeled values and the experimental ones. The first is that when calculating the resonant frequency, the mass of the top metal electrode is not included in the calculation. The aluminum/titanium electrode has a Young's modulus that is much lower than that of the silicon nitride and does not contribute significantly to the stiffness of the membrane yet the electrode has a mass of about a third of the membrane. The additional mass acts to lower the resonant frequency. Another possible source for the discrepancy is that the capacitance of the cell is underestimated. This is likely for two reasons; the first is because the fringe field is set to zero even though the two electrodes of the capacitor are of different sizes [98]. The optimal balance between maximizing bandwidth and capacitance is to have the top electrode be half the diameter of the bottom electrode [99]. The other is that the metal leads connecting the cells to one another are not accounted for. A sense of the value of this discrepancy is given from a Coventor simulation of the cell capacitance of a first generation device (with no bias). The simulated value is ~15% larger than that obtained using equation (3.22). Finally the model is sensitive to material parameters and device dimensions. The device dimensions used for the simulation are the nominal values obtained during fabrication. There is however variability in the process in terms of layer thicknesses and cavity and electrode diameters. These are discussed to a certain extent in Chapter 4, 5, and 6.

The model also neglects many of the other interactions between the membranes either through the substrate or through surface waves. However, as a first order approximation for the impedance, resonant frequency and pull-in voltage it is acceptable.

Chapter 4 First Generation CMUT Device

4.1 Introduction

In this chapter the fabrication and characterization results of the first generation of successfully made CMUT devices is discussed. The reason this chapter is included is because this first generation of devices exhibits certain beneficial characteristics that are not duplicated in subsequent fabrication runs. The reason for this is believed to be because of a slight change in the fabrication process from one generation to the next. The short time frame between the completion of this first generation and the unavailability of the Cornell Nanofabrication Facility (due to a substantial increase in user rates) meant there was no time to completely characterize these devices before CMUTs suitable for phased array imaging needed to be finished.

4.2 Design Objectives

The device design was chosen to be relatively conservative (in terms of membrane thickness, cell diameter and fill factor) to ensure successful fabrication while obtaining operating parameters that would prove insightful to future generations of devices. Based upon simulations done in CoventorWare as well as work previously reported in the literature, dimensions were chosen to yield a resonant frequency of ~15 MHz in air and ~5-10 MHz in immersion. Frequencies in this range are comfortably accessible to commercial ultrasound generation and receiving tools and are used for imaging applications. Element size is designed to help ensure large signal generation and receive sensitivity. A consequence of this is that the element pitch is much too large to attempt any phased-array experiments with these devices.

Before moving on it is worthwhile to briefly mention some of the failed designs that were attempted prior to the successful process being achieved. It is hoped that by doing so, future students may avoid spending time and money on a process that is unlikely to succeed.

From the start the fusion bonding fabrication method was the desired method to move forward due its simple and straightforward processing steps. In the first attempted design the patterned electrodes were to be the bottom electrodes. This was done so that the membrane could be conductive polysilicon. The result being that gap between the top and bottom electrode would consist

of only the cell cavity and a bottom insulation layer and therefore lowering the necessary DC bias for efficient operation. The bottom electrode material, either doped polysilicon or titanium, was deposited on top of an insulator and patterned. Next, an insulation layer of silicon dioxide was deposited on top to prevent short circuiting of the conductive membrane and bottom electrode. The bottom wafer was then to be planarized to permit fusion bonding. Unfortunately, the surface could not be made flat enough to permit a good fusion bond. The chemical mechanical polishing process would flatten the surface features but could not completely eliminate them as the polishing pad would tend to conform to the surface and just round off the corners. With the titanium as the bottom electrode, a damascene process was attempted but was also unsuccessful. In some cases a fusion bond would seem to be made but would come apart when trying to release the membrane. A few other permutations, such as using silicon nitride as the insulation layer, were attempted but successful release could not be achieved.

The first devices to survive the fabrication process discussed in the next section failed during electrical testing at the University of Waterloo. In some small areas (typically a few cells together) the membrane would come off during the membrane release step. An example of this is shown in Figure 4.1. As a result metal deposited for the top electrode would be placed directly into the cavity of those cells. When a bias voltage is applied, only the insulation layer prevents a short circuit between the top and bottom electrode in those cells. The insulation layer was unable to prevent dielectric breakdown and all of the devices were damaged during electrical testing. An SEM image of a damaged device is shown in Figure 4.2. The area of dielectric breakdown would short-out the entire element rendering it unusable. The layout of these devices was such that each transducer consisted of only a few elements, millimeters on a side, comprised of tens of thousands of individual cells. Therefore a failure to bond rate of less than one percent of all cells (which is what was observed) meant that there were no functioning devices. It is for this reason that the transducer design of the first generation devices contain only moderately sized elements. Very large elements increase the likelihood of a small defect in the transducer ruining the entire device.

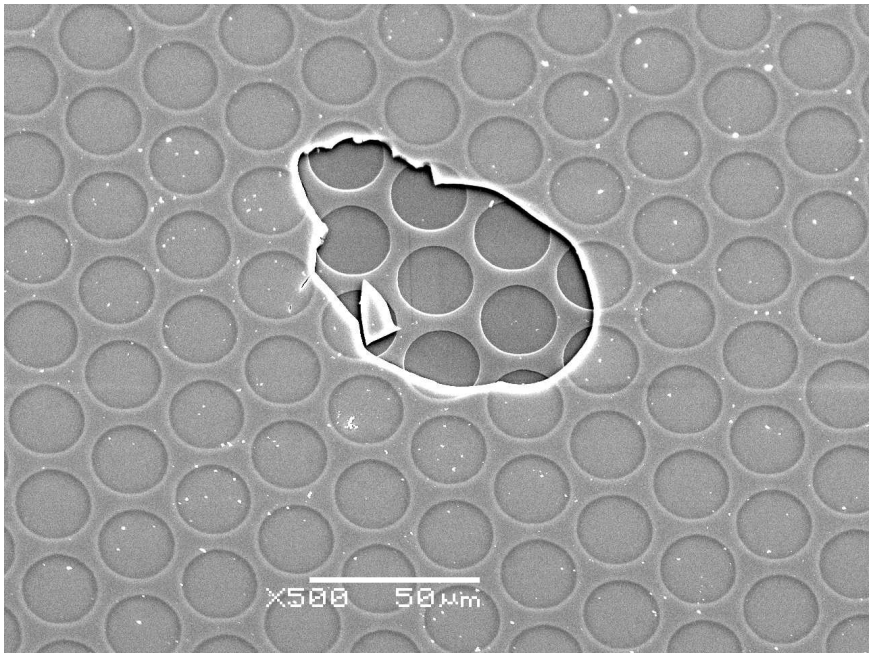

Figure 4.1: An SEM image of a pre-metallization device where the membrane came off during release.

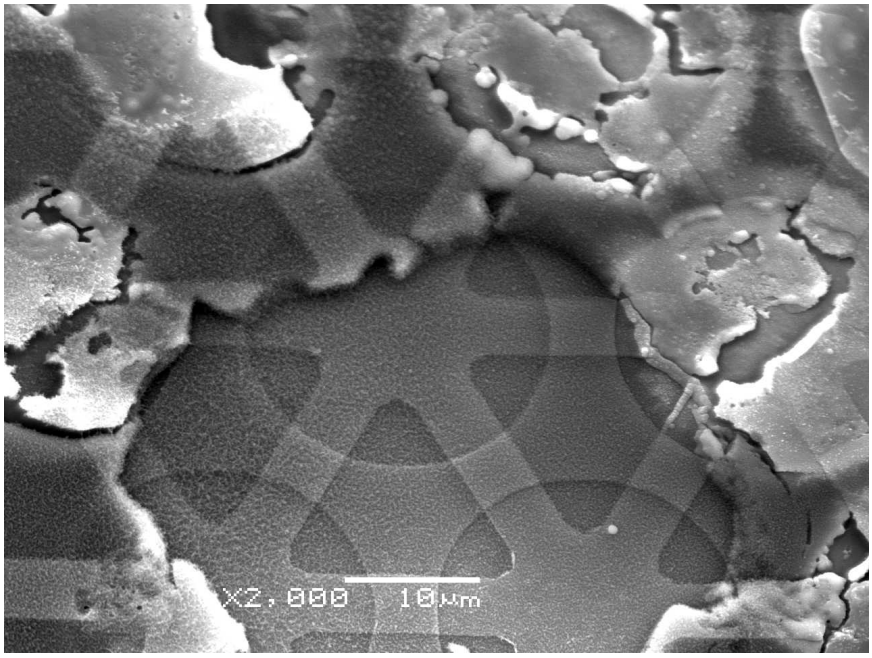

Figure 4.2: An SEM image of device after failure due to dielectric breakdown. Damage of this type is typically associated with a defect in membrane bonding.

4.3 Fabrication Method

The fabrication process of this generation of devices is similar to that used in the SOI wafer bonding process outlined in Section 2.5.2. Only 3 masks are needed to achieve the final device. Fabrication was done at the Cornell Nanofabrication Facility (CNF) at Cornell University in Ithaca, New York. A $\langle 100 \rangle$ 100 mm silicon wafer is used for both the membrane and the bottom electrode/cavity. The bottom wafer is lightly *p*-doped with boron and has a resistivity of 1-5 Ω-cm.

Because the bottom wafer has only moderate conductivity, a layer of LPCVD p+ polysilicon 750 nm thick is deposited at 600°C (the dopant is boron) to reduce the series resistance of the bottom electrode, Figure 4.3(a). The bulk of the wafer and the polysilicon layer will be used as the bottom electrode in the transducer. In the next generation one-dimensional arrays a highly conductive silicon wafer will be used which will obviate the need for the polysilicon layer. The bottom wafer is then annealed at 1000°C for 1 hour which increases the polysilicon grain sizes and increases the conductivity. The resistivity of the annealed polysilicon is measured to be ~9 mΩ-cm using a 4-point resistance mapper. The sheet resistance of the annealed polysilicon on top of the silicon wafer is measured to be ~30 Ω/sq.

The resulting increase in grain size that comes from the annealing process makes the polysilicon very rough with peaks of 50-100 nm being common. For that reason a short chemical mechanical polishing (CMP) step is used to smooth the surface again, Figure 4.3(b). The wafer is polished for about 30 seconds using a slurry of silicon dioxide particles suspended in a very dilute KOH solution. About 50 nm of material is removed in the polishing step. The RMS roughness before polishing is ~18 nm and after it is ~2 nm. Atomic force microscopy (AFM) scans of pre- and post-polished polysilicon are given in Figure 4.4.

Next, low-stress LPCVD silicon nitride is deposited on top of the polysilicon as a spacer and insulation. At the same time, nitride is deposited on the top wafer for what will be the membrane, Figure 4.3(c). The low-stress nitride is deposited at 800°C. The residual tensile stress of the low-stress nitride deposited from the LPCVD system has previously been characterized by CNF technicians as approximately 200 MPa.

While LPCVD nitride is not nearly as rough as the annealed polysilicon it must still be polished because fusion bonding is very sensitive to roughness and in order to achieve a good quality bond as

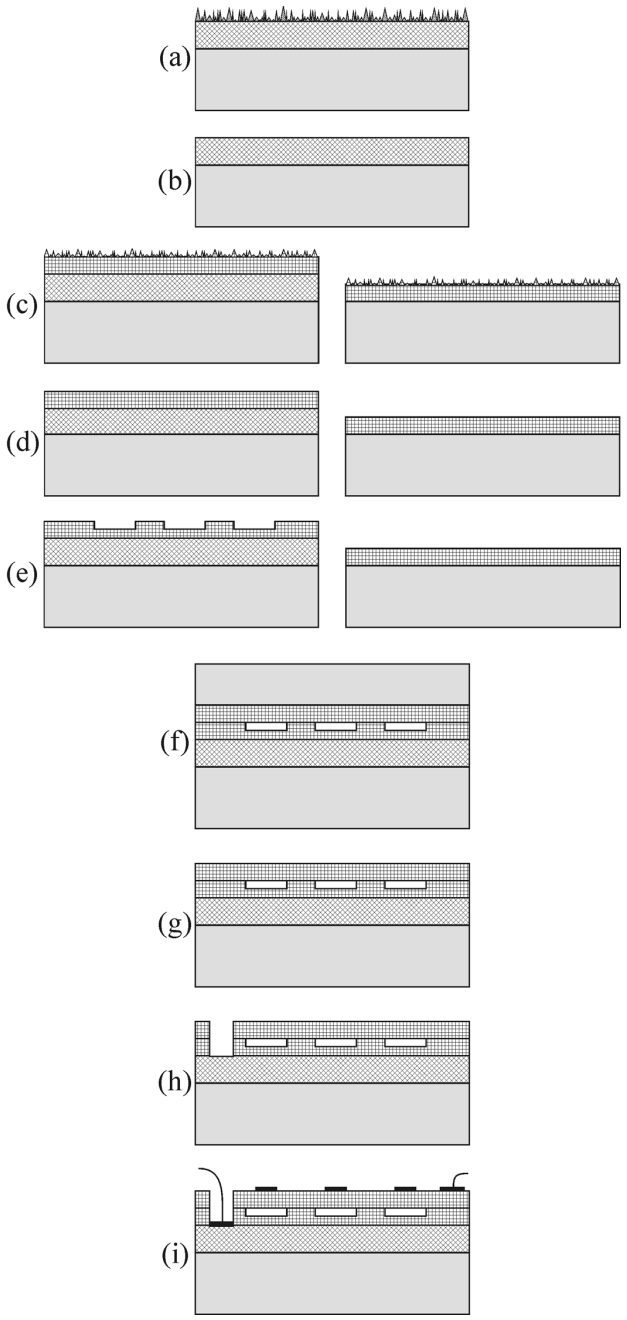

Figure 4.3: Summary of the fabrication process of a 1-D CMUT array. (a) Deposit p+ LPCVD polysilicon and anneal at 1000°C. (b) Smooth the surface with a short CMP step. (c) Deposit low-stress LPCVD silicon nitride on both wafers. (d) Perform a short polish of the SiN layer on both wafers. (e) Define cell cavities with an RIE step. (f) Fusion bond the top and bottom wafers. (g) Release the membrane in a KOH etch. (h) Expose the ground electrode with an RIE. (i) Pattern the top electrodes and contact pads using lift-off of evaporated metals.

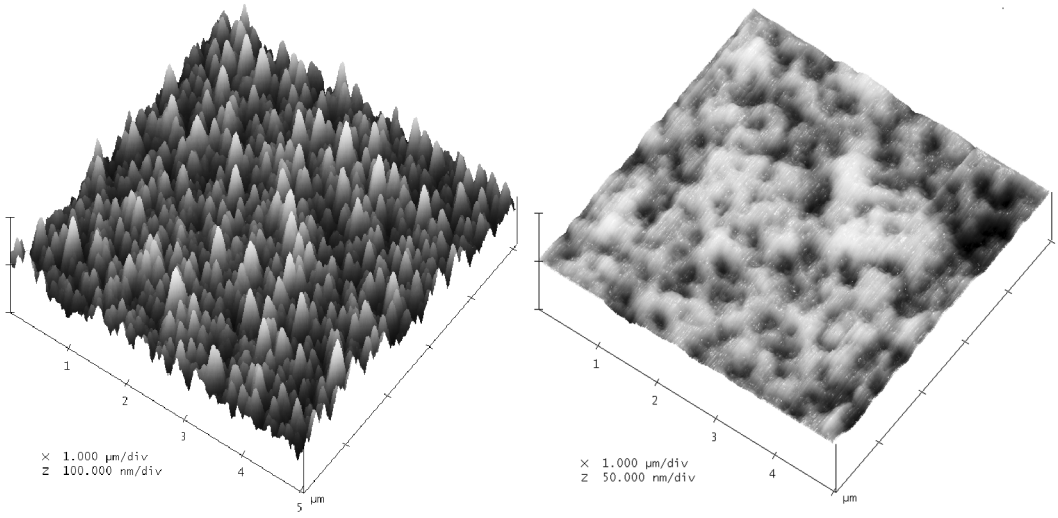

Figure 4.4: AFM scans of the polysilicon layer pre- (left) and post- (right) chemical mechanical polishing. The RMS roughness before polishing is 18 nm and after is 2 nm.

smooth a surface as possible is necessary. Both the top and bottom wafers are polished for about 50 seconds using the same silicon dioxide particle slurry, Figure 4.3(d). About 30 nm of material is removed and the RMS roughness of the membrane wafer is improved from 14 Å to 4 Å. That of the bottom wafer is slightly worse at ~8 Å after polishing. A surface plot of an AFM scan of the pre- and post- polished membrane wafer is given in Figure 4.5.

Care must be taken immediately after the polishing step. The post polished wafers must be rigorously washed and scrubbed to remove the silicon dioxide particles remaining on the surface from the CMP slurry. These particles can prevent bonding in their local area. If too many remain on the surface prior to bonding the yield will suffer.

The maximum RMS roughness typically cited as being required for decent quality spontaneous fusion bonding is 5 Å. The surface roughness of the nitride on polysilicon is somewhat greater than this apparent maximum value. A discussion of the bonding yield and potential explanations of the results are given in Section 4.4.

Following the polishing step, the cell cavities are etched into the bottom wafer nitride layer using a CF_4 reactive ion etch (RIE) process after a photolithography step using Mask I. The etch depth is about 160 nm. The step is illustrated in the left-hand diagram of Figure 4.3(e).

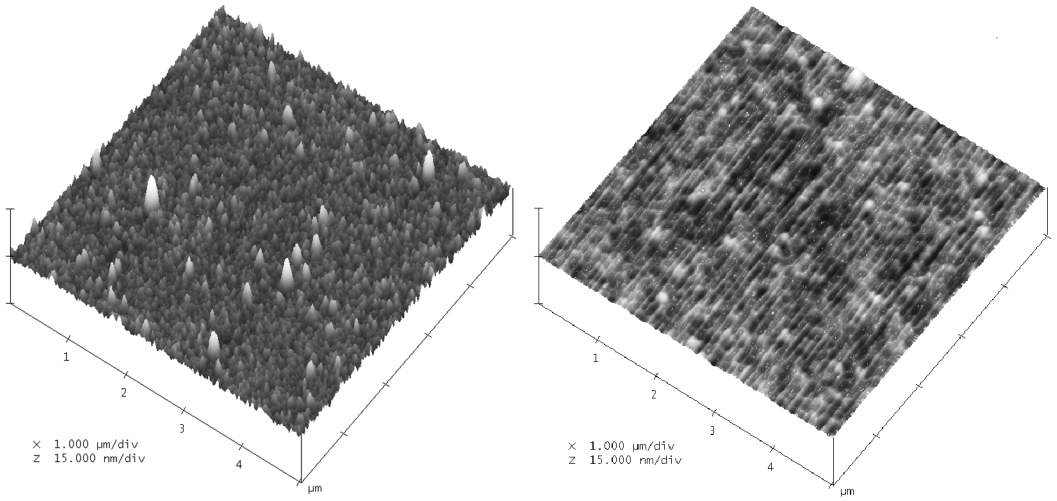

Figure 4.5: AFM scan of the pre- (left) and post- (right) polished silicon nitride layer. The RMS roughness before polishing is 1.4 nm and afterwards it is 0.4 nm.

After the RIE etch both the top and bottom wafers are cleaned in both an RCA 1 and RCA 2 bath, a low power oxygen plasma descum followed by another RCA 1 clean. The two wafers are then fusion bonded at 300°C in a chamber at a pressure of 0.7 µbar. A compressive force of 3500 N is applied for 10 minutes, Figure 4.4(f). The low pressure is required so that each of the cells is effectively a vacuum. This reduces the squeeze film dampening from within the cell. Following the bonding step the wafers are annealed at 900°C for 4 hours.

The silicon nitride on the backside of the bonded membrane wafer is removed via a CF_4 RIE process. With the nitride layer removed the silicon of the handle wafer is exposed and is removed by a 25% KOH etch at 95°C. The etch takes about 5 hours to completely remove the 500 µm wafer. The bonded wafer with the handle wafer removed is shown in Figure 4.3(g).

Next, a photolithography step is done using a second mask to pattern the ground electrodes. A CF_4 RIE etch is performed to etch through the nitride membrane and spacer layers to expose the ground electrode for metallization, shown in Figure 4.3(h). Finally, the top electrodes and contact pads are patterned using a third mask and a lift-off process. Titanium and aluminum are evaporated using an e-beam. About 30 nm of titanium is used as an adhesion layer and about 100 nm of aluminum is deposited on top. An illustration of the completed 1D array is given in Figure 4.3(i). A table of the device properties is given in Table 4-1. SEM images of a completed device are given in Figure 4.6.

Table 4-1: Physical properties of a first generation 23 element device.

Property	
Membrane Diameter	22 μm
Membrane Thickness	400 nm
Electrode Diameter	11 μm
Cavity Depth	140 nm
Insulation Thickness	260 nm
Element Length	8000 μm
Element Width	330 μm
# of elements	23
# of cells per element	4140

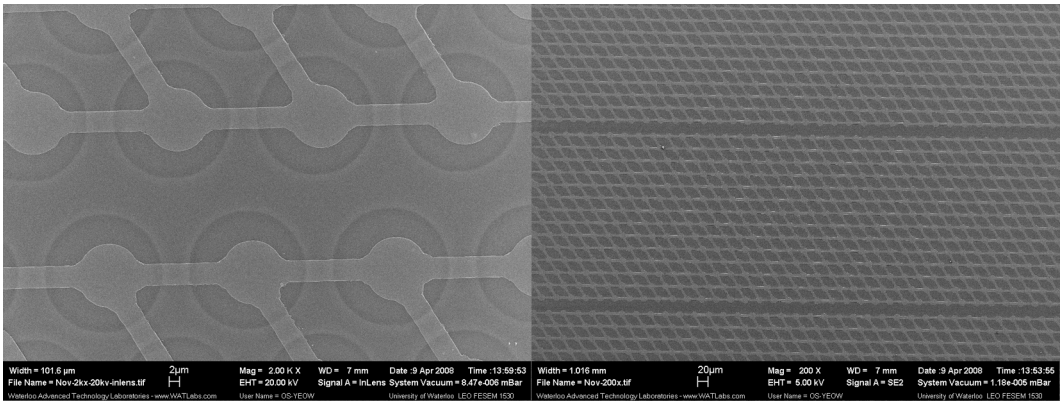

Figure 4.6: SEM images of a completed 23 element CMUT array.

4.4 Fabrication Yield

The fabrication yield is strongly dependent on the CMP step and the cleanliness of the wafers. While CMP is an established microfabrication process, experience has shown that it is not quite as predictable as other tools. The polishing rate is not uniform across the surface of the wafer. The removal rate tends to be higher away from the center of the wafer. Successful wafer bonding is primarily dependent on wafer smoothness and not flatness, however the difference in polishing rate can result in variations in thickness of the membrane layer across the wafer. These differences are less

than the variations observed from the deposition of low-stress LPCVD silicon nitride which can vary by up to 10% across a wafer. Variations in thickness will reduce the uniformity of the frequency of operation across devices.

Despite some of the challenges associated with CMP the membrane yield achieved with the fusion bonding process was reasonably good. Defining success as having at least 99.5% of the membranes bonded to the bottom wafer after release; slightly more than 80% (20 of 24) of the transducers released would be considered successful. Bonding at a local level is quite good; when failure to bond occurs it tends to be clusters of 5 adjacent membranes or more. Therefore, failure to bond appears to be more likely a result of contamination of one of the wafer surfaces as opposed to a surface too rough to bond. Given the roughness of the bottom wafer (measured RMS roughness of ~8 Å) it is somewhat surprising that the yield is as high as it is. A maximum RMS roughness of 5 Å is usually cited when bonding is done at room temperature with little additional pressure. It is possible that by operating in a vacuum at an elevated temperature with a relatively large compressive force being applied to the wafer pair (3600 N) the tolerance for roughness is eased somewhat. A possible mechanism is that because the cell cavities are a vacuum they tend to pull down on the membrane when at atmospheric pressure. More work will need to be done to investigate where the discrepancy occurs. As has been stated previously, the next generation of one-dimensional arrays eliminates the polysilicon layer and hence the roughness penalty associated with that layer.

For various reasons (mainly hedging against unexpected processing mishaps) only 8 transducers were taken from the released stage to completion. Of the 8 that were completed 7 have none or only one non-functional element. The remaining device has two non-functioning elements. As was the case with the first released devices, the failure mechanism of the elements is related to the non-bonded membranes which have peeled off. The insulating layer alone, even though the thickness is ~260 nm, is unable to prevent dielectric breakdown when the bias voltage exceeds 40-50 V. Electrical testing of the low-stress nitride indicates its relatively weak dielectric strength.

4.5 Device Characterization Results

A variety of experiments are typically performed to characterize a device. These include impedance tests using a vector network analyzer to determine the device resonant frequency as well as a variety of acoustic tests to determine operating frequency and performance in immersion.

4.5.1 Electrical Device Characterization

The resonant frequency of the device in air is determined by measuring the impedance of an element as a function of frequency. One-port s-parameter measurements are made using a 150 μm pitch ground-signal-ground (GSG) ACP40A RF probe from Cascade Microtech and an Agilent 8714ES Vector Network Analyzer. The measured s-parameter is converted to impedance via the following equation:

$$Z_L = Z_0\left(\frac{S_{11}+1}{S_{11}-1}\right) \tag{3.31}$$

Z_L is the complex impedance of the device under test; Z_0 is the system impedance and is assumed to be 50 Ω. S_{11} is the reflection coefficient of the input port of the circuit, in this case a CMUT element. At resonance very little energy is reflected back to the VNA as energy is efficiently converted to mechanical motion and manifests itself as a large resistance. This generation of CMUT does not have the necessary GSG contact pads to make the impedance measurement directly. As a result an adapter wafer with the necessary contact pad configuration is used. The CMUT is wirebonded to the adapter wafer. To measure the resonant frequency at different DC biases, an Inmet 8800SMF1-06 bias-T is used to add the DC component to the RF supplied by the VNA. The CMUT chip is mounted on a probe station and the DC+RF signal is applied via the RF probe. A schematic of the electrical layout is given in Figure 4.7. The resonant frequency of two devices is measured. With no bias voltage applied the resonant frequencies of the first and second devices are 17.5 MHz and 15.3 MHz, respectively. The collapse voltage can be determined by an abrupt change in the impedance characteristics as the bias voltage is swept. The observed collapse voltages are 55 V and 50 V for the two devices. At a bias voltage of 50 V the resonant frequency of the first device is 15.8 MHz. At a bias voltage of 45 V the resonant frequency of the second device is 14.1 MHz. A plot of the real part of the impedance at a number of different bias voltages for the first device is shown in Figure 4.8. A similar plot of the second device is given in Figure 4.9. The effect of spring softening can be observed as the bias voltage increases i.e. the resonant peak shifts to lower frequencies. The non-flat baseline impedance is due to RF noise pollution of the signal (because the system setup is not fully shielded) and not related to CMUT membrane motion. A plot of the imaginary impedance of the first device at a 50 V bias is shown in Figure 4.10.

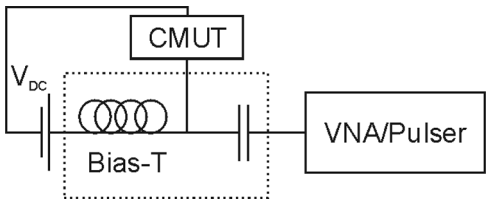

Figure 4.7: Electrical schematic of circuit used to characterize the CMUT array.

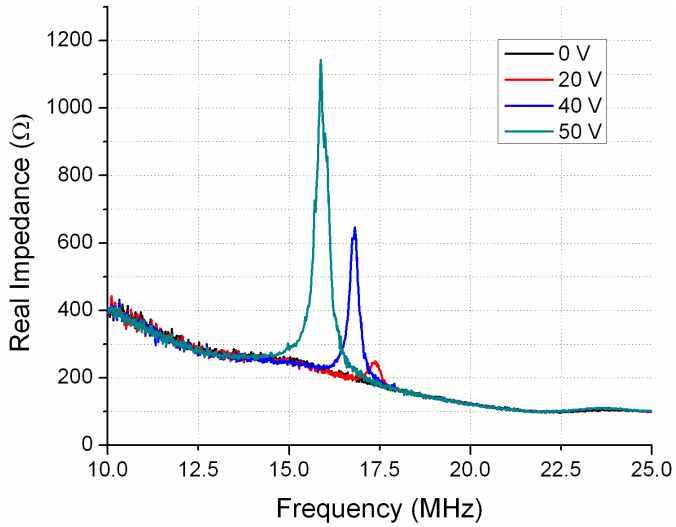

Figure 4.8: Real component of the impedance of a single element of a 23 element array at different bias voltages.

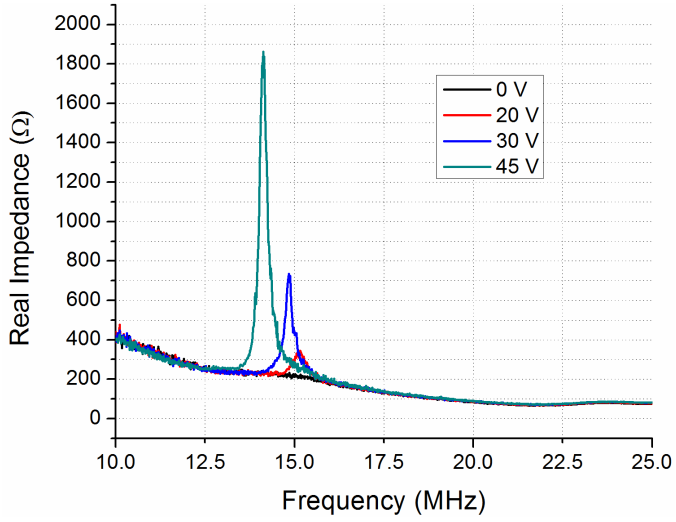

Figure 4.9: Real component of the impedance of a single element of a second first generation device at different bias voltages.

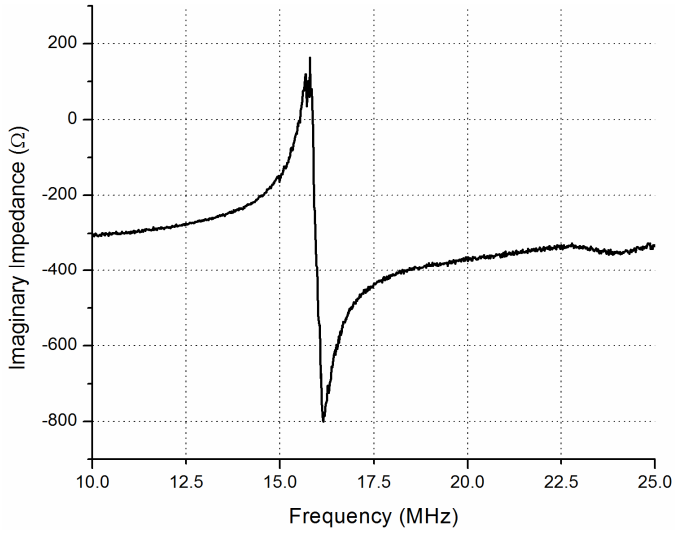

Figure 4.10: Imaginary component of the impedance of a single element of the first 23x1 array at a bias of 50 V.

4.5.2 Pitch-Catch Acoustic Experiment Setup

Two sets of experiments are performed in immersion to characterize the transducer. The first is a pitch-catch experiment where one element is used to transmit a signal to a nearby commercial hydrophone. The second is a pulse-echo experiment where a single element is used to transmit an acoustic pulse which then bounces of a steel block in the fluid and the reflected signal is measured with a different element on the same transducer.

For the pitch-catch experiment, the peak center frequency and bandwidth of a single element is determined by measuring the acoustic signal using a commercial hydrophone (an Onda HGL-0200, and an Onda AH-2010 20dB preamplifier) at a given distance from the CMUT element. The signal is recorded with a high speed oscilloscope. The fluid used is vegetable oil because an insulating fluid is needed to prevent electrical shorting of the exposed leads. The acoustic impedance and absorption of oil are also reasonably similar to that of tissue [100]. Future devices will need to incorporate a bio-compatible insulating coating to eliminate short-circuiting in all reasonable fluid environments [101]. An applied -40 V DC bias is added to a short ~-100 V negative voltage pulse from a commercial pulser/receiver (Panametrics 5073). A schematic of the electrical circuit used is given in Figure 4.11. The 4.7 μF capacitor serves to protect the pulser from the DC bias, while the inductor and resistor make the bias arm of the circuit high-impedance forcing the negative pulse through the CMUT. The distance between CMUT and hydrophone is estimated by measuring the time between the voltage

pulse and the measuring of the acoustic signal with the hydrophone. A speed of sound of 1430 m/s is assumed [22].

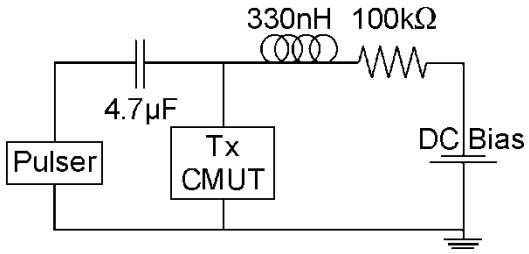

Figure 4.11: Schematic of the circuit used to drive the pulse-echo experiments.

Correcting for oil absorption, diffraction and the hydrophone frequency response gives a better indication of the transducer characteristics. The vegetable oil used in these experiments is an unknown mixture of canola and soybean oils. Chanamai and McClements have characterized the absorption coefficients of many edible oils including canola and soybean [102]. Acoustic absorption is governed by a typical inverse exponential law:

$$A = A_0 e^{-\alpha x} \tag{3.32}$$

where A is the amplitude of the signal after the absorber, A_0 is the amplitude at the source, x is the path length and α is the attenuation coefficient. The attenuation coefficient is dependent on the material and the frequency of operation. Given the data from Chanamai and McClements the equation for α is given as:

$$\alpha = Af^n \tag{3.33}$$

where A is a coefficient with a value of 7.83 x 10^{-12}, f is the frequency in Hz, and n is another coefficient with a value of 1.84. The coefficients of these oils are similar enough that it is not necessary to know the proportion of canola and soybean in the vegetable oil to correct for the absorption, therefore the coefficient values of canola oil are used.

In terms of determining the bandwidth of the transducer we are only interested in the relative effect absorption has as a function of frequency. Therefore to account for the effect the frequency dependent absorption has on the bandwidth we simply divide the Fourier spectrum of the transducer signal by the absorption spectrum.

We perform a similar operation to compensate for diffraction losses. Diffraction is dependent on frequency because the amount of spreading due to diffraction is dependent on the relative size of the aperture compared to the wavelength. Therefore, for a broadband source, such as a CMUT in immersion, the lower frequency components will spread out noticeably more than the higher frequency components because the ratio of wavelength to aperture is larger. Using the equations given by Szabo for a rectangular aperture in [103] we can correct for the relative difference in diffraction as a function of frequency by dividing the Fourier spectrum by

$$D \propto \frac{1}{\sqrt{\lambda}} \tag{3.34}$$

where λ is the wavelength range of the ultrasound pulse and we assume we are in the far-field. The details of what constitutes the near- and far-field will be discussed in Section 6.3.

The hydrophone and preamplifier frequency response are taken into account using characterization data provided by the manufacturer. A schematic of the experimental setup is given in Figure 4.12.

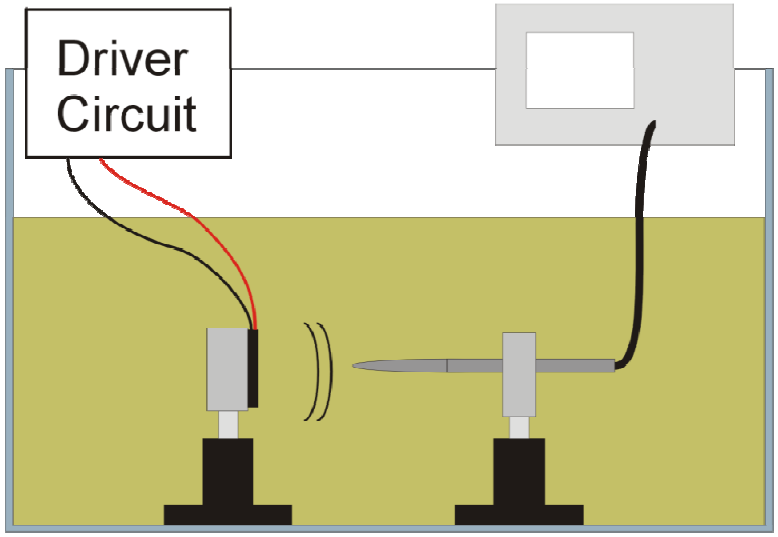

Figure 4.12: A schematic of the pitch-catch experiment used to characterize the first generation transducer. The hydrophone is connected to a preamplifier (also in the oil). Signal is recorded with the oscilloscope. The CMUT is connected to an external-to-the-tank circuit via a BNC cable.

4.5.3 Pitch-Catch Experimental Results

The pitch-catch experiment is performed with the hydrophone at a distance of 8 mm. The uncompensated center frequency is 9.3 MHz and the -3dB bandwidth is 8.6 MHz which translates to a relative bandwidth of 92%. After compensating for the absorption of the oil, diffraction and the response of the hydrophone the center frequency is 9.2 MHz and the -3 dB bandwidth is 10.5 MHz for a relative bandwidth of 114%. The center frequency is defined as midway between the two -3 dB points. Plots of the time and frequency domain signal from a single array element are shown in Figure 4.13 and Figure 4.14.

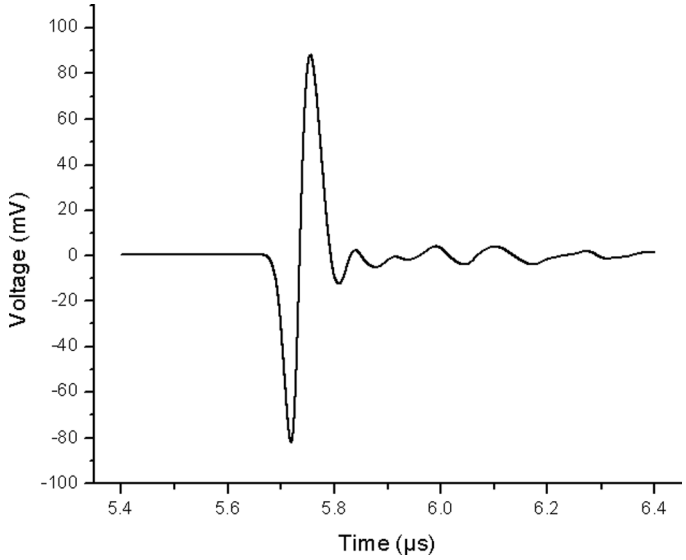

Figure 4.13: Time domain plot of transmission pulse of a single element 8 mm away from the hydrophone, biased at -40V.

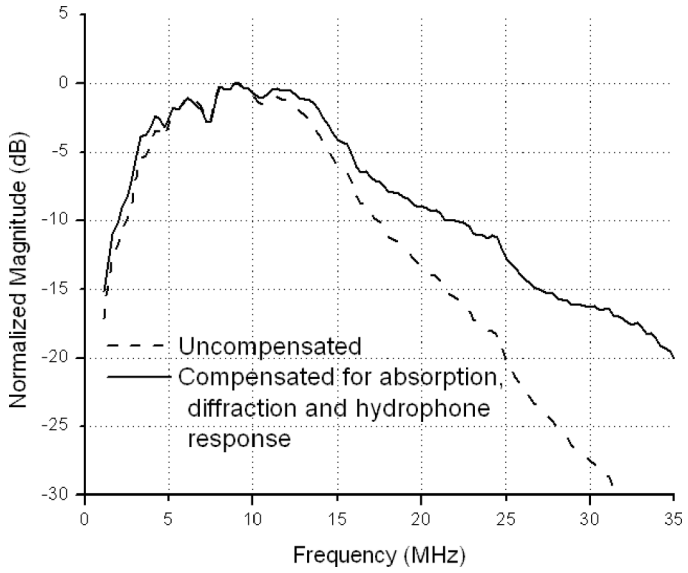

Figure 4.14: Compensated and uncompensated frequency domain plot of the transmission pulse from a single element 8 mm away from the hydrophone. The element is biased at -40 V. The compensated response is corrected for both the oil absorption and the hydrophone response. The uncompensated and compensated -3 dB center frequencies are 9.3 MHz and 9.2 MHz respectively. The relative bandwidths are 92% and 114% for the uncompensated and compensated responses respectively.

4.5.4 Pulse-Echo Experimental Setup

In this experiment one element of the array is used to generate the ultrasound pulse while another is used to receive the signal reflected from a steel block placed at a given distance. The block has a width of ~2 cm, a thickness of ~4 cm and a height of approximately 30 cm. A diagram of the experimental setup is given in Figure 4.15.

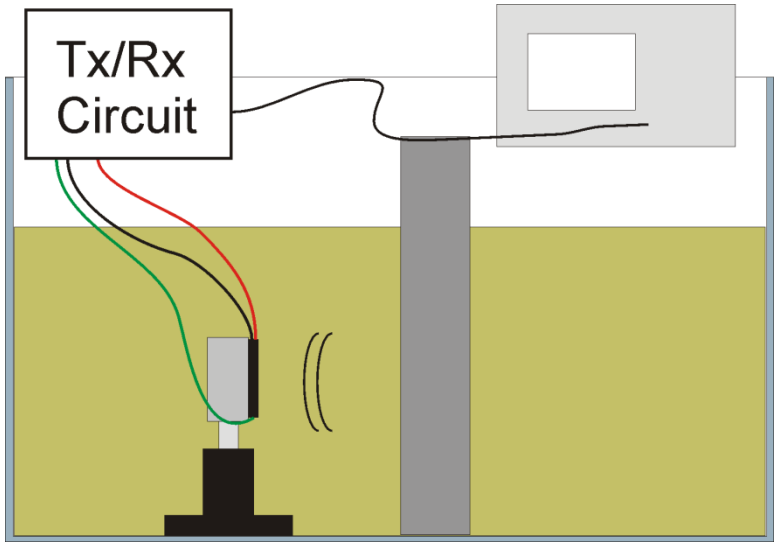

Figure 4.15: A schematic of the experimental setup for pulse-echo measurements. The red wire is for transmitting the voltage pulse, the black wire is ground and the green wire carries the small measured current back to the op-amp.

The transmit and receive elements are separated by about 1 mm on the surface of the transducer array. Using different elements to transmit and receive is done to simplify the electronics required for this experiment. In future work a more sophisticated circuit is employed to permit transmission and reception from the same element. A Texas Instruments OPA 657 operational amplifier is wired in a transimpedance configuration with a gain of 4 kΩ to amplify and convert the small current generated by the receiving element to a voltage. The signal is recorded with an oscilloscope. A schematic of the transmission/receiving circuit is illustrated in Figure 4.16. The inductor and resistor protect the amplifier from the voltage spike from the pulser. The capacitors block the DC signal from the pulser and the amplifier.

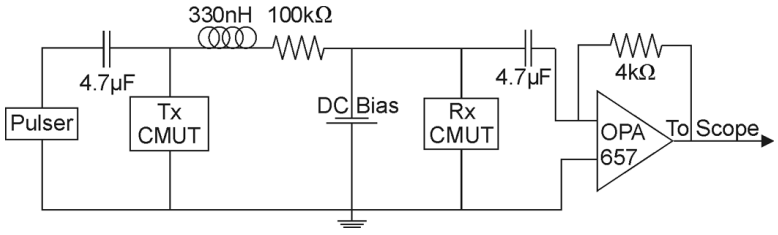

Figure 4.16: A schematic of the circuit used for pulse-echo characterization.

4.5.5 Pulse-Echo Experimental Results

As with the transmission measurements the frequency response of the transducer is corrected for oil absorption and diffraction. Time and frequency domain plots of the signal reflected from a steel block ~12 mm away are given in Figure 4.17 and Figure 4.18 respectively. Before compensating for the oil absorption the -6 dB center frequency is 8 MHz with a bandwidth of 9.6 MHz for a relative bandwidth 120%. After compensating for the oil absorption the center frequency is 9 MHz with a bandwidth of 11.1 MHz for a relative bandwidth of 123%. The center frequency is defined as the midpoint between the two -6 dB points.

Notches in the frequency spectrums at approximately 7.5 MHz are clearly visible in Figure 4.14 and Figure 4.18. These correspond to the substrate ringing modes of the bulk silicon as has been previously described by Ladabaum *et al* [104].

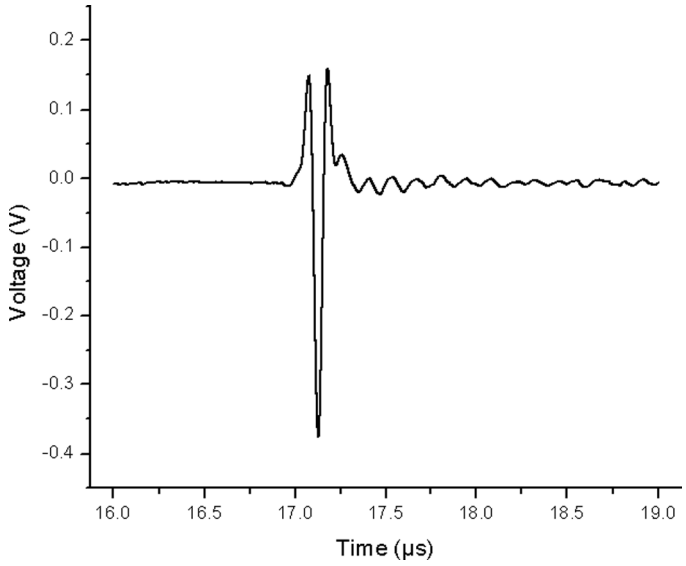

Figure 4.17: Time domain plot of a pulse-echo signal. The signal is reflected off a steel block ~12 mm away. The elements are biased at -40V.

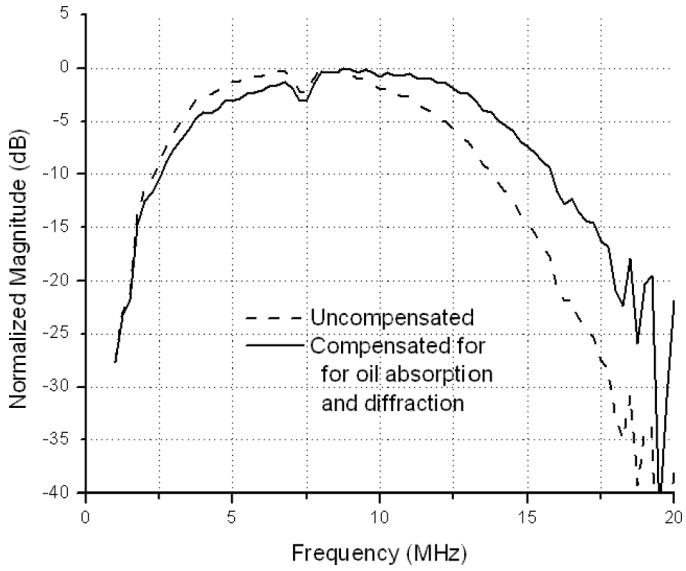

Figure 4.18: Fourier transform of a transmit-receive signal from one element to another. The signal is reflected off a steel block ~12 mm away. Both elements are biased at -40V. The uncompensated and compensated -6 dB center frequencies are 8 MHz and 9 MHz respectively. The relative bandwidths are 120% and 123% for the uncompensated and compensated responses respectively.

4.6 Investigation of Dielectric Charging

Trapping of electric charges in the dielectric insulating layer can lead to a degradation of performance in CMUT type devices over time and has the effect of masking the applied DC bias reducing the transduction efficiency [75]-[76], [105]. This effect is one of the primary drawbacks of CMUTs for commercial transducer applications. It has been shown many times that these charging effects can lead to a dramatic change in the DC operating point of the device [77]. In more extreme cases the membranes do not return from their collapsed position after the bias voltage has returned to zero [77] (collapse occurs when the electrostatic force from the DC bias exceeds the mechanical restoring force of the membrane causing the membrane to snap-down to the bottom of the cell cavity). The dielectric charging can be reversed by switching the polarity of the bias and driving the trapped charges out of the dielectric. Finding a way to eliminate dielectric charging would be significant because it would allow for the uninterrupted operation of a CMUT without a change in output pressure and sensitivity or the need to occasionally reverse the charging.

4.6.1 Dielectric Charging Experimental Setup

Measurements studying the effects of dielectric charging are made by monitoring the capacitance of a CMUT element over a period of more than 5 days. If charging occurs one would expect a shift in the pull-in and snap-back voltages over time.

In the experiment a previously unused element is biased at -80 V (past the collapse voltage of ~50 V) and negative voltage spikes from a Panametrics 5073 pulser at 1 kHz are applied for approximately 30 minutes. Experience indicates that this step stabilizes the performance of a new device. Though the reason for this is not entirely clear, it is hypothesized that this is due to charges trapped during the fabrication process rearranging themselves [77]. After this initialization step the element is biased at -40 V (in the non-collapsed regime) and the same negative voltage spikes are applied at a 1 kHz repetition rate. The capacitance of the element is determined by setting up a voltage divider circuit consisting of a 100 kΩ resistor in series with a CMUT element and measuring the potential drop across the CMUT. The same bias-T configuration illustrated in Figure 4.7 is used to add the DC bias to a 20 kHz 1V p-p sine wave from a function generator. The bias voltage is monotonically swept from 0 to -80 volts then from -80 V to +80 V and finally from +80 V to 0 V. Symmetric capacitive behaviour from the device when it is biased both positively and negatively indicates that there has been neither significant charging nor an accumulation of trapped charges.

4.6.2 Dielectric Charging Experimental Results

Measurements were taken after the initialization step, after 1 hour of charging, after 25 hours of charging and after 140 hours of charging. The measurements were done by disconnecting the pulser and connecting a function generator to apply the small ac signal. The measurements took about 45 minutes after which the pulser was reconnected and the charging continued.

A plot of the capacitance as a function of (positive) bias voltage after different charging times is shown in Figure 4.19. As can be seen the collapse voltage is initially between 45 and 50 V and the snapback voltage is between 10 and 20 V. In theory the transition to and from the collapse regime should be a very sharp. This is not observed because the individual membranes that make up the element can have slightly different collapse voltages and this tends to smear out the transition to and from the collapse regime. Over time it can be seen that there is little change in the either the shape of the graph or the values of the collapse and snapback voltages. After 140 hours of charging there is a small increase (<5 %) in the absolute capacitance measured but otherwise little else of note.

As stated above, the symmetry of the capacitance about the 0 V bias point is also indicative of dielectric charging. Shown in Figure 4.20 are plots of the capacitance as a function of both positive and negative bias voltage. Notwithstanding the post-collapse capacitance values in Figure 4.20(a) and a deviation of less than 5 pF in Figure 4.20(d) near the collapse and snap-back voltages, the data is essentially symmetrical. It is, therefore, reasonable to conclude that these CMUTs with a low-stress silicon nitride membrane and insulation layer suffer from minimal charging effects and can be operated for long periods of time with little change in performance.

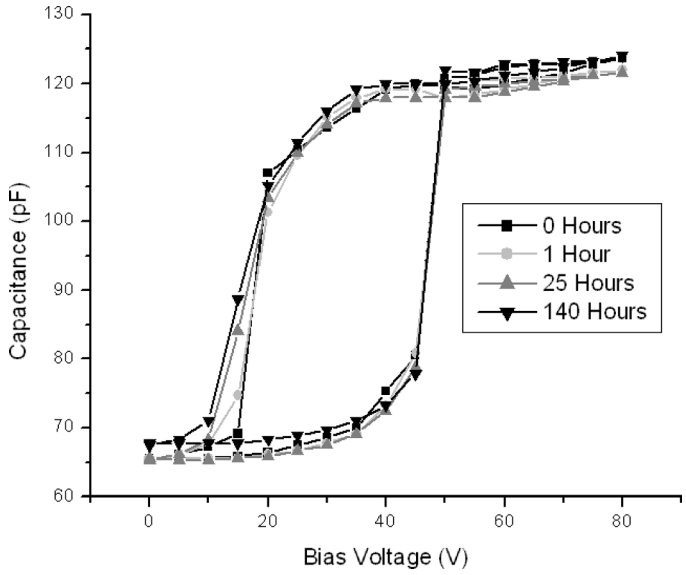

Figure 4.19: Demonstration of the lack of charging effects with Si_xN_y wafer bonded devices.

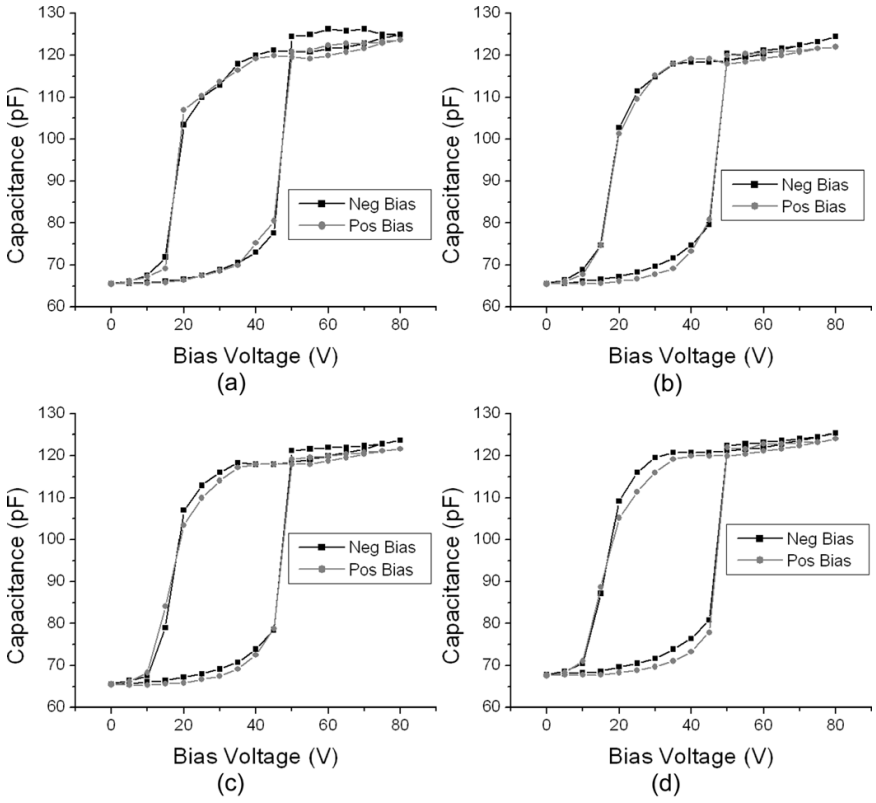

Figure 4.20: Plots of the capacitance of a CMUT element as a function of bias voltage after charging for (a) 0 hours, (b) 1 hour, (c) 25 hours, (d) 140 hours.

4.7 Failure Mechanisms

The devices described in this chapter have proven to be robust enough to operate for extended periods of time with little to no change in operating performance. Extended experience with the devices has shown that those that are successfully fabricated are extremely durable and are unlikely to fail while handling or in operation. When they did fail it was inevitably because, as mentioned in section 4.2, the membrane had not remained bonded to the substrate during the fabrication process. As such, after metallization the top electrode is inside the cell cavity and the insulation layer by itself is unable to prevent dielectric breakdown at modest DC biases of under 50 V. Testing of the dielectric properties of the low-stress silicon nitride by staff at CNF indicated that it does indeed have a low dielectric breakdown voltage consistent with the observations discussed here. It was possible to get successful data from these devices because the membrane remained bonded to the substrate in the vast majority of areas and the elements are sufficiently small that a good yield is achieved, as discussed in section 4.4.

Aside from dielectric breakdown of the insulation the other problem that crops up routinely with these devices is that wire bonding can occasionally be difficult. Wire bonding the contact pads of these devices to a chip carrier was performed using a wire bonder at CNF. Not infrequently the ultrasonic energy from the bonder would cause the membrane and the contact pad to come off. This problem seems to occur randomly with some contact pads from the same transducer coming off, while others bond normally with the same settings. It is possible that the bonder supplies enough energy to magnify any defect that may be present in the fusion bond between the membrane and the substrate causing it to separate. It should be noted that the settings of the bonder were not explored very thoroughly at Cornell and that this behavior is much rarer in subsequent generations of devices wire bonded using facilities at the University of Waterloo.

4.8 Discussion

The primary goal of this generation of devices has been to demonstrate the viability of fusion bonding chemically and mechanically polished silicon nitride to silicon nitride for the purpose of fabricating ultrasound transducers. Results indicate that the devices produced operate as expected, with a bandwidth greater than 120% and frequency of operation within the desired range. They have also proven to be quite durable with no change in performance over extended periods of time.

The fabrication process described is relatively straightforward and takes many of the best attributes of the typical surface fabrication and wafer bonding processes described in the literature. The process requires only three masks and can be completed by an individual in less than a week. The bonding process allows for the design and fabrication of the membrane and cavity wafers independently of one another which adds to flexibility in the design. It also permits tighter packing of the individual cells because sacrificial release channels are not required. Elimination of the etch channels is important as future work in high-frequency two-dimensional arrays will put strict limitations on element size and as large an active area as possible will be needed to obtain a sufficiently high signal-to-noise ratio.

To address the poor dielectric strength of the low-stress silicon nitride future generations incorporate a thin layer of stoichiometric nitride into the insulation layer. The stoichiometric nitride has been tested to have a dielectric strength close to that of thermally grown oxide (~900 V/μm).

4.8.1 Possible Mechanism for Resistance to Charging Effects

Aside from the fact that this first generation of devices indicates the suitability of using a user-deposited membrane in the fabrication of fusion bonded CMUTs the most important observation was the lack of dielectric charging. As is shown in section 4.6.2 the devices operate through collapse with both positive and negative bias voltages with no significant shift in the measured capacitance. Future generations incorporate a thin layer of stoichiometric nitride to reduce the likelihood of dielectric breakdown. While those devices do indeed exhibit a reduction in the number of occurrences of dielectric breakdown they also exhibit the negative effects of dielectric charging. While the fabrication methods of those devices is discussed in the following chapters it is sufficient to say here that the only significant changes in the fabrication process between the first generation devices and the next generation of one-dimensional arrays is that the polysilicon layer is eliminated and a 200 nm layer of stoichiometric nitride is incorporated. Of the two differences it would seem that the change in the composition of the insulation layer is the more significant. Unfortunately, given the massive increase in cost of fabrication at CNF, further experiments exploring this parameter have not been performed.

A more thorough exploration of the effect the stoichiometry of the silicon nitride has on dielectric charging, dielectric strength, yield (through changes in the residual stress), and performance may provide an opportunity to develop devices that incorporate the best of both low-stress and stoichiometric nitride. A device that does not exhibit the negative effects of dielectric charging while at the same time does not fail when only the insulation layer (and not both the insulation layer and the membrane) separates the top and bottom electrodes would be very advantageous.

Chapter 5 One-Dimensional Arrays

5.1 Introduction

The second generation capacitive micromachined ultrasonic transducers (CMUT) fabricated at the Cornell Nanofabrication Facility (CNF) consists of many different types of devices. These include one-dimensional arrays of different sizes, ring arrays and 1.5D arrays. The devices operate at one of two frequencies. Either a lower resonant frequency of approximately 15 MHz, or a higher resonant frequency of approximately 37 MHz. Due to time constraints the majority of the characterization experiments were performed on the lower frequency one-dimensional arrays. In this chapter the fabrication process, device characterization, beamformer design and two-dimensional phased array image generation are discussed in detail.

5.2 Design Objectives

The objectives of this generation of devices are to simplify the fabrication process, reduce some of the limitations of the previous generation and introduce the ability to perform phased array imaging. With that in mind two frequencies of operation are chosen, the first being the same as was successfully demonstrated in the previous generation (a resonant frequency of 15 MHz) and a second, higher one, that would be more suitable for catheter or endoscope based imaging. This is because, as was discussed in section 2.2.2, higher frequency operation can allow for higher resolution imaging and the poorer penetration depth at these frequencies is less of an issue. Also, the element sizes tend to be smaller and are therefore more amenable to the packaging restrictions of an endoscope or catheter.

For the low frequency devices, a variety of array arrangements are fabricated, the one tested extensively is a 64 element linear array. Also fabricated are 128 element linear arrays, 64x5 1.5 D arrays and 64 element ring arrays. While not giving the same beam control in elevation as a fully populated 2D array, a 1.5D array does allow some adjustment of the focal depth [106]-[107], though typically a fixed acoustic lens is still used. A ring array permits three-dimensional imaging with a much reduced element count when compared to a fully populated 2D array [41], [108]-[109]. Image suffers somewhat due to the sparseness of the array and the low signal-to-noise ratio that results. Essentially time constraints prevented experimentation with these devices. Drawing the designs for

these devices on the photolithography masks is a much easier thing to do than to design the control schemes and experiments to test them.

Multiple types of higher frequency arrays are also fabricated. These include 64 and 192 element linear arrays as well as 128 element ring arrays. Of these devices only the 64 element linear array is tested. The goal for these devices is to have a resonant frequency of ~40 MHz and a frequency of operation of ~25 MHz. While the resonant frequency is relatively easy to calculate analytically, the frequency of operation in a fluid is much more difficult. At the time of fabrication the design requirements for a 25 MHz frequency of operation was essentially an educated guess based on limited experience and results published in the literature. It is necessary to have some sense of what the centre frequency will be to permit the appropriate design of the element pitch.

The number of elements is chosen as a balance between transducer size and potential image quality. More elements results in an improved image quality, but also increases the transducer size. In the end, only a subset of the array elements are connected for phased array imaging due to the size and complexity of the circuits needed to drive them.

5.3 Fabrication Method

The fabrication process reported here was performed at the Cornell Nanofabrication Facility (CNF) at Cornell University in Ithaca, New York, it has been reported in [110]. It is a simplified version of the process discussed in Section 4.3. The bottom wafer is a $\langle 111 \rangle$ highly doped n+ 100 mm silicon wafer with a resistivity of ~0.01-0.02 Ω-cm. It is used as a common electrode to the entire CMUT. The top wafer is a $\langle 100 \rangle$ 100 mm wafer that is used as a mechanical platform on which to deposit the membrane.

The process begins with the deposition of 520 nm of low-pressure chemical vapour deposition (LPCVD) low-stress silicon nitride for what will become the device membrane (Figure 5.1 (a) - right). On the bottom wafer ~250 nm of stoichiometric silicon nitride is deposited, followed immediately by 200 nm of low-stress LPCVD silicon nitride, (Figure 5.1 (a) – left). The purpose of the stoichiometric nitride relates to its superior electrical insulating properties and is discussed in Section 4.8.1.

Good quality fusion bonding is enabled by subjecting both the top and bottom wafers to a quick chemical mechanical polish using a slurry consisting of silicon dioxide particles mixed in a dilute

KOH solution (Figure 5.1 (b)). The final nitride thickness of the top wafer is ~500 nm and the bottom wafer has a combined thickness of both types of nitride of ~ 420 nm.

The cell cavities are photolithographically patterned onto the bottom wafers and etched using a CF4 reactive ion etch (RIE) process to a depth of ~160 nm (Figure 5.1 (c) – left). The two wafers are then cleaned using a standard MOS clean, followed by an oxygen plasma clean, and finally another RCA 1 clean. The wafers are then fused together in a wafer bonder for 10 minutes at 120°C at a pressure of 0.5 μbar and compressive force of 3600 N. A 4 hour anneal at 950°C strengthens the bond, Figure 5.1(d).

The silicon nitride on the backside of the membrane wafer is etched away using an RIE step to permit the removal of the membrane handle wafer using a heated KOH bath. The removal rate is about 100 μm/hour and the nitride membrane acts as the etch stop, Figure 5.1(e).

In the second photolithography step the bottom electrode contact pads are patterned and then exposed by an RIE step through all of the nitride to the doped silicon wafer, Figure 5.1(f).

Patterning and metallization of the contact pads and top electrodes is the final step and consists of 30 nm of titanium followed by 100 nm of aluminum deposited using an e-beam evaporator, Figure 5.1(g). A table of the physical properties of the completed 64 element transducers is given in Table 5-1. Optical and SEM images of completed low- and high-frequency arrays are shown in Figure 5.2 and Figure 5.3 respectively.

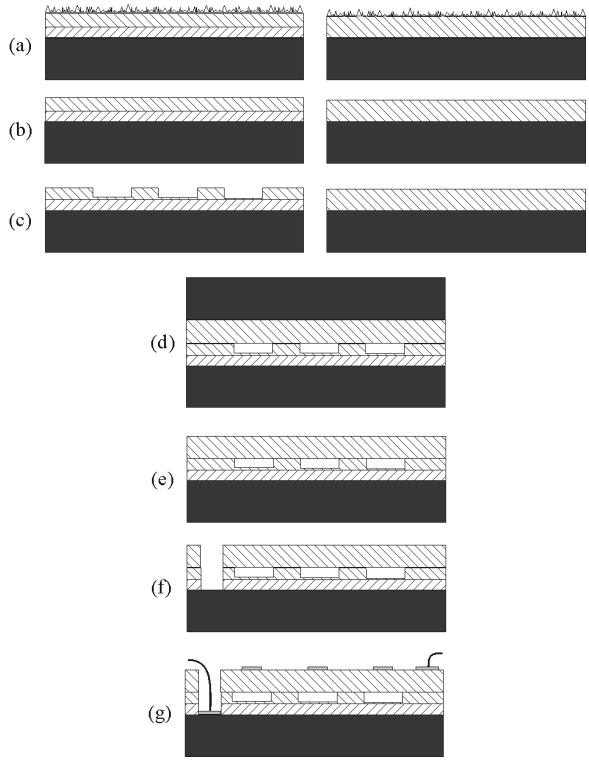

Figure 5.1: Summary of the fabrication process. (a) Deposit low-stress nitride (right) and stoichiometric and low-stress nitride (left). (b) Chemical mechanical polish of both wafers. (c) Pattern and etch cell cavities. (d) Fusion-bond the two wafers. (e) Release membrane. (f) Pattern and expose ground electrode. (g) Deposit and pattern metal for top electrode and contact pads.

Table 5-1: Physical properties of the 64 element low- and high-frequency linear CMUT arrays.

Property	Low Freq	High Freq
No. of Elements	64	64
Membrane Diameter	25 µm	15 µm
Membrane Thickness	500 nm	500 nm
Electrode Diameter	15 µm	9 µm
Cavity Depth	160 nm	160 nm
Insulation Thickness	260 nm	260 nm
Element Length	5000 µm	2000 µm
Element Width	200µm	32 µm
# of cells per element	1424	228

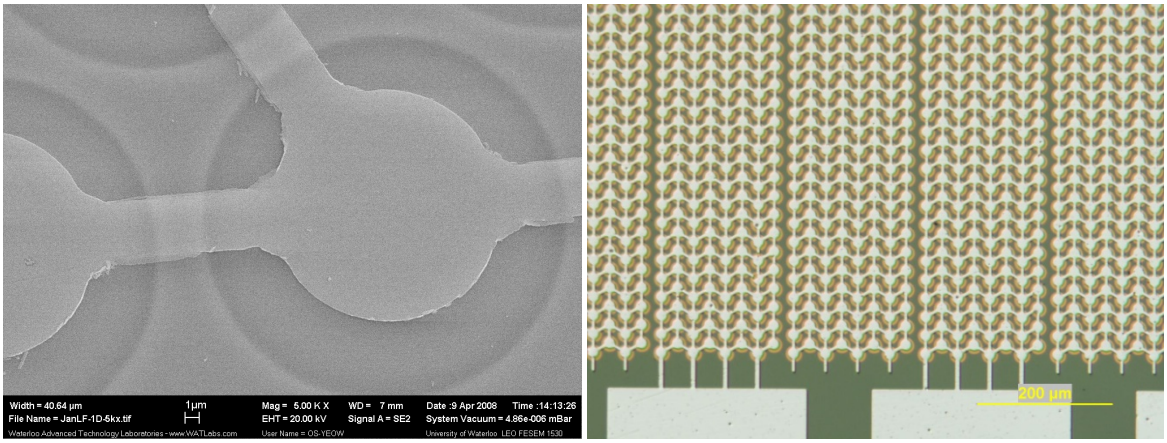

Figure 5.2: SEM and optical images of completed low-frequency 64x1 CMUT array.

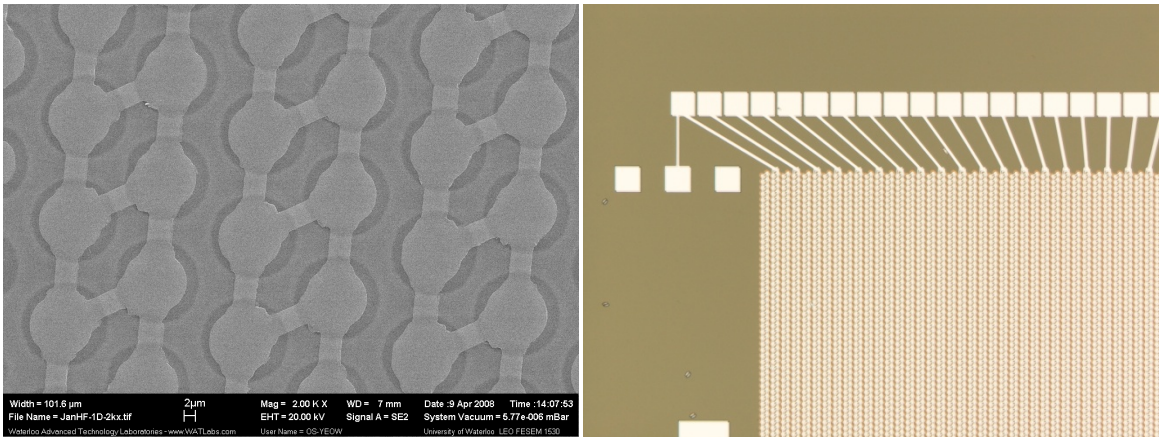

Figure 5.3: SEM and optical images of completed 64x1 high frequency arrays.

5.4 Fabrication Yield

The yield achieved with this generation of devices is qualitatively similar to that obtained from the previous generation. The fusion bond and release steps are the most critical, none of the other steps are particularly demanding. As with the previous generation, the yield from some wafers was nearly 100% while that from other wafers would yield only one or two devices where the membrane is completely attached. With the elimination of the polysilicon layer it is believed that the intrinsic roughness of the surfaces after polishing is not the principle factor inhibiting a consistently good bond. It seems unlikely that it would fluctuate to such a large degree on a single wafer and from wafer to wafer when all of the polishing materials and parameters are the same. It is more likely that the

large fluctuation in successful bonding comes from either residual particulates from the polishing slurry or from contamination after the second RCA cleaning but before bonding.

The mechanical polishing particulates in the slurry are an issue when polishing silicon nitride, which is hydrophobic. After the wafer is removed from the polishing pad the CMP machine sprays it with DI water which helps rinse the surface clean but does not completely remove all of the particulates. When unloading the polished wafer from the machine the DI water stops flowing and the water on the surface quickly beads up leaving remaining slurry particles behind to get permanently stuck on the surface. To deal with this the machine operator must transfer the wafer as quickly as possible from the machine to a bucket of DI water, before the water beads up significantly. The wafer is then transferred to an RCA 1 cleaning bath which forms a thin silicon oxynitride layer on the surface which is hydrophilic. The wafer can then be cleaned in a machine that gently mechanically and chemically cleans the surface of wafer to remove all of the remaining particulates. If the wafer were do go directly from the CMP machine to the wafer cleaning machine the water would bead up before the machine could start and the slurry particles would become stuck on the surface.

It is very difficult to determine if slurry particles have stuck to the wafer surface due to their small size (tens of nanometers). A nominal check of the wafer is done using a profilometer to scan various locations on the post-polished wafer. Clearly only a tiny fraction of the wafer surface is scanned and it amounts to a small statistical sampling. Despite the author's best efforts, this particular step remains the most likely reason for inconsistent bonding results.

A secondary source of potential surface contamination is the transfer of the wafers from the final cleaning bath to the wafer bonder. Efforts are made to maintain the cleanliness of the wafer bonder and to minimize the likelihood of contamination during transfer, which must be transported approximately 50 meters across the cleanroom.

5.5 Single Element Characterization

In this section the electrical and acoustic characterization of single elements of the second generation of devices is reported. As stated at the beginning of this chapter, the majority of the characterization work has been done with the low frequency 64 element arrays, however, some single element electrical and acoustic characterization of the high frequency arrays has been done as well.

5.5.1 Electrical Device Characterization

Electrical characterization of the low-frequency devices has been performed using two experimental setups consisting of different probe stations and vector network analyzers (VNA). The first setup used exactly the same equipment to characterize the first generation devices as discussed in Section 4.5.1; the second used an Agilent N5242A PNA-X network analyzer. In that case a Picosecond Pulse Labs 5530B bias-T is used to combine a DC bias to the RF signal provided by the network analyzer. Electrical characterization of the high-frequency devices has been done only with the first equipment setup. More extensive characterization of the low-frequency devices has been carried out using the second setup and so the results from those experiments are presented here.

The S_{11} parameter of a single element of a 64-element low-frequency device is measured with a 10 V DC bias applied. The S parameter is converted to impedance using equation (3.31). The observed resonant frequency is 14.4 MHz. A 10 V bias makes the resonant peak more clearly defined while keeping the frequency shift due to spring softening at a minimum. As the bias is increased to 60 V the resonant frequency drops to ~13.6 MHz. The collapse voltage is observed to be ~75 V with this device. The changing baseline as the bias increases is due to interaction between the network analyzer and the bias-T. Calibration work was done to minimize this effect, but it was not possible to completely remove it. A plot of the real component of the element impedance is shown in Figure 5.4. Similarly the resonant frequency of a single element of a 64-element high frequency linear array is measured at three different bias voltages. A plot of the real component of the impedance is shown in Figure 5.5. The resonant peak of 37 MHz is observed at a 0V bias. The collapse voltage was not determined using this method because the collapse voltage is greater than the rated limit of the bias-T used. A result of this is that the frequency shifting is not as dramatic because the device is operating further from the collapse voltage. For this data series the noise on the impedance plot was reduced by passing the data through a low-pass filter.

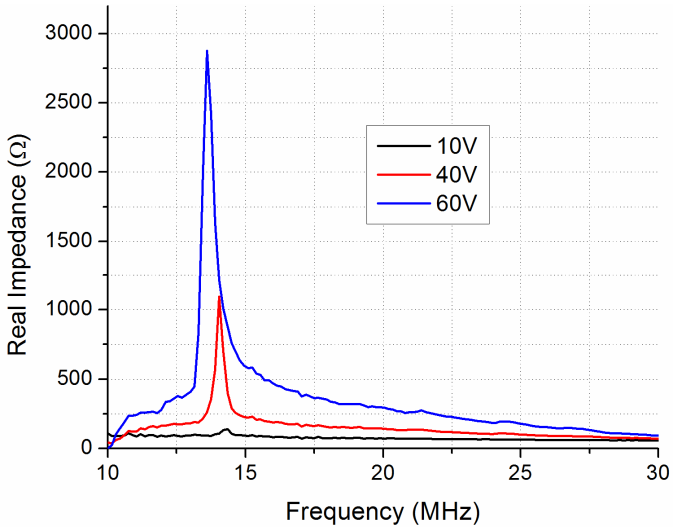

Figure 5.4: Real impedance of an element from a low-frequency 64-element linear array biased at different potentials.

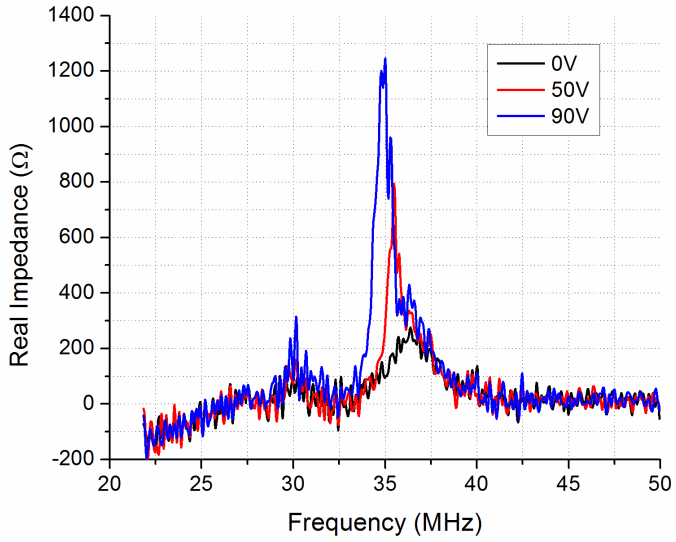

Figure 5.5: Real impedance of an element from a high-frequency 64-element linear array biased at different potentials.

5.5.2 Pitch-Catch Experimental Setup

Similar to the electrical characterization, different experimental setups have been used at different times to quantify CMUT performance in immersion. The same relatively primitive pitch-catch experiments used for the first generation devices, as discussed in Section 4.5.2, are used to

characterize both the low- and high-frequency devices, though only the results of the high-frequency devices are presented with this setup. A second set of experiments using a more advanced scheme are used to characterize only the low-frequency device. The rest of this section discusses the equipment setup used for the second set of experiments.

As the ultimate goal of these devices is to use them as phased-array imagers, a system able to perform this function is necessary. The immersion characterization for the first generation devices (and high frequency devices) uses a commercial ultrasonic pulser/receiver to generate the large voltage pulse necessary to create an ultrasonic pulse. For phased array imaging many individually addressable pulsers are needed to be able to steer the beam. While straightforward to implement, an array of commercial pulser/receivers is far too expensive to use. An alternative is devised using low-cost off-the-shelf components driven by a field programmable gate array (FPGA). To perform the pulse-echo experiments a single channel of this beamformer circuit is used to generate the voltage pulse. The pulser consists of two single-pole double-throw (SPDT) switches (Analog Devices ADG333A) and a fixed delay circuit (a pair of Texas Instruments CD4011BPW NAND gates). It is triggered by a 3.3 V pulse from a Xilinx Virtex 4 XC4VSX35 FPGA. The SPDT switches can tolerate a voltage difference of ~40 V across the inputs, which is suitable for a CMUT driving pulse. However, the off-on-off switching time is several hundred nanoseconds, too long to generate a useful pulse by itself. A 40 V bipolar pulse with a FWHM of ~40 ns can be generated by using two of the switches in series and a trigger that is delayed between the two of them. A block diagram of the pulser is given in Figure 5.6. It should be noted that instead of using a bias-T to add the voltage pulse to the DC bias, the bias is now connected to the bottom electrode of the CMUT. When using this pulser for experiments a unipolar 30 V pulse is used. An example of an excitation signal from the pulser is given in Figure 5.7.

Aside from using a single channel of the custom built beamformer to drive the CMUT pulse, the transducer is installed into the PCB of the beamformer which is mounted perpendicularly to the bottom of the fish tank using an L-mount fastened to an optical breadboard. The hydrophone is mounted onto a 3-axis optical translation stage (Thorlabs PT3) which has a graduation of 10 μm. The result of this is a consistent and repeatable measurement system. A diagram of the setup is shown in Figure 5.8. The received signal is recorded with a high speed oscilloscope.

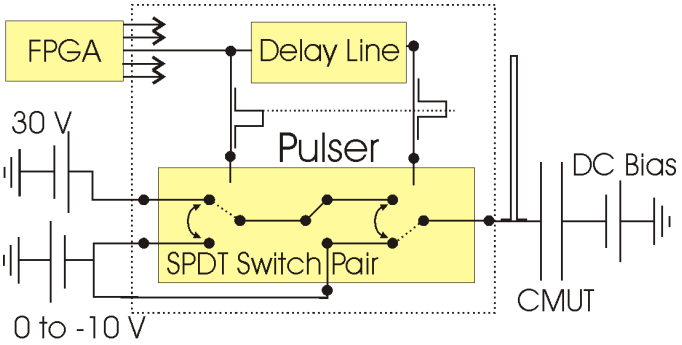

Figure 5.6: A block diagram of the circuit used to generate the CMUT driving pulse. An FPGA is used to trigger the switch. The DC bias is applied to the opposite electrode of the CMUT.

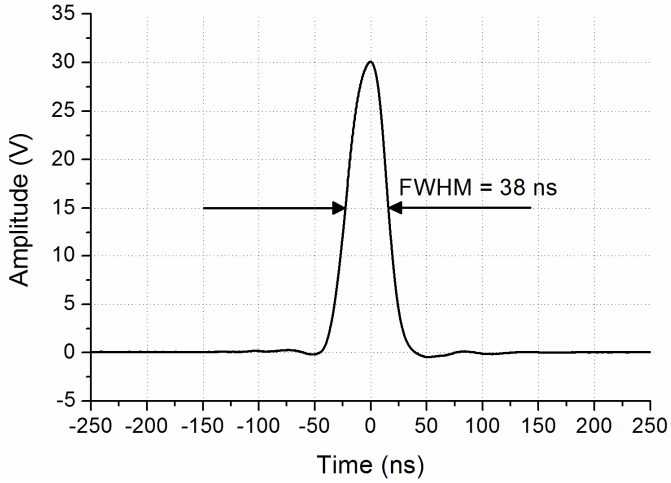

Figure 5.7: A 30 V voltage pulse generated by the pulser. It has a full-width-at-half-maximum of 38 ns.

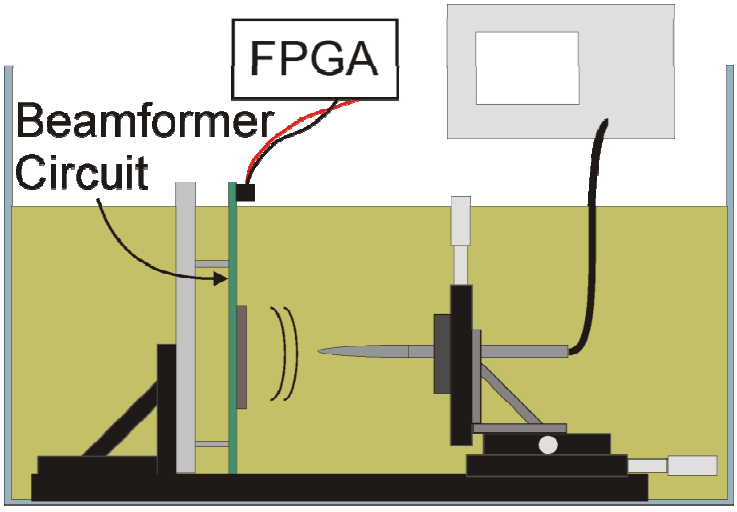

Figure 5.8: Schematic of the setup used for improved pitch-catch measurements.

5.5.3 Pitch-Catch Experimental Results

Presented here are the pitch-catch results from a low-frequency element driven by the beamformer and from the high-frequency device driven by the commercial pulser/receiver. The high-frequency devices are not tested with the beamformer circuit because the electrical pulse is too long to effectively excite the transducer.

For the measurement of the low frequency device the hydrophone is placed 20 mm away from the surface of the transducer. The distance is determined by measuring the time between the voltage trigger sent to the beamformer circuit and the arrival of the acoustic pulse at the hydrophone. A speed of sound is determined to be 1470 m/s.

The DC bias is set to -60V (~80% of the collapse voltage) and the voltage amplitude is 30 V. A plot of the recorded acoustic pulse from a single element is given in Figure 5.9. The voltage signal recorded by the oscilloscope is converted to pressure using the characterization data supplied by the manufacturer of the amplifier and hydrophone. Taking the Fourier transform yields the centre frequency and the bandwidth of the pulse. The -3dB bandwidth is measured to be 4.2 MHz with a center frequency of 5.2 MHz. Correcting the transform for hydrophone response (provided by the manufacturer, [111]), oil attenuation (absorption data from [102]) and diffraction (using equations from Szabo, [103]) yields a center frequency of 5.3 MHz and a -3 dB bandwidth of 5.9 MHz which corresponds to a 111% fractional bandwidth. This is consistent with typical CMUT bandwidths exceeding 100%. A plot of the compensated and uncompensated Fourier transform is given in Figure 5.10.

The hydrophone is located ~1.8 mm away from the transducer when measuring the response of the high frequency 64-element array. The transducer is so close because the high frequency components are greatly attenuated by the vegetable oil. The negative voltage pulse is supplied by the commercial pulser/receiver and the DC bias is -125 V. The two signals are combined in the same manner as shown in Figure 4.11. The voltage pulse is applied to three neighbouring elements to increase the signal strength. A plot of the time domain signal is given in Figure 5.11. The measured pressure value takes into account the hydrophone and amplifier response. Taking the Fourier transform of the time domain signal yields a -3dB centre frequency of 18.3 MHz with a bandwidth of 8.3 MHz or 45%. A plot of the transform before and after correcting for absorption and diffraction is given in Figure 5.12. Correcting the spectrum of the acoustic pulse for the response of the hydrophone is not possible because calibration data is only available out to 20 MHz. Correcting for

absorption and diffraction does not change the centre frequency or the bandwidth values due to the proximity of the transducer to the hydrophone.

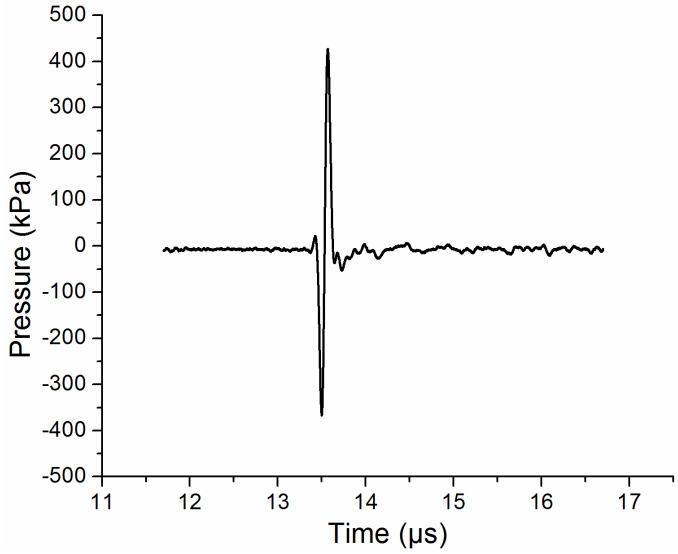

Figure 5.9: Time domain plot of the pitch-catch signal sent from a single element of a 64 element low-frequency 1D array. The hydrophone is 20 mm from the transducer. The signal is corrected for hydrophone response, absorption and diffraction.

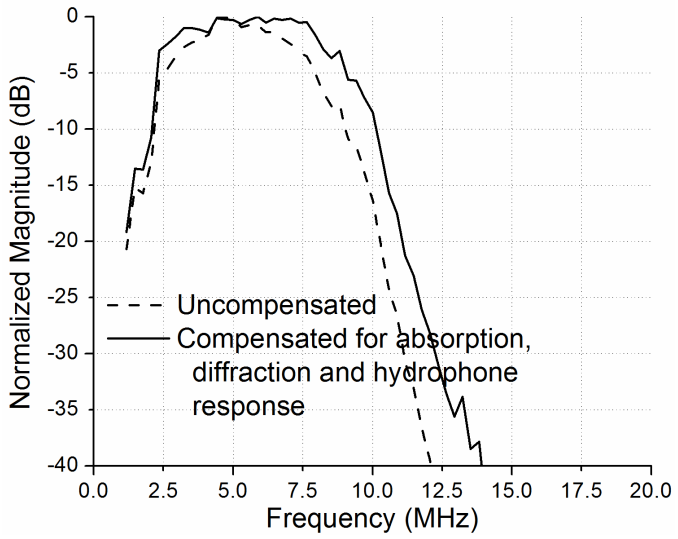

Figure 5.10: A frequency domain plot of the compensated and uncompensated Fourier transform of the pitch-catch measurement. The -3 dB centre frequency of the compensated plot is 5.2 MHz with a fractional bandwidth of 111%.

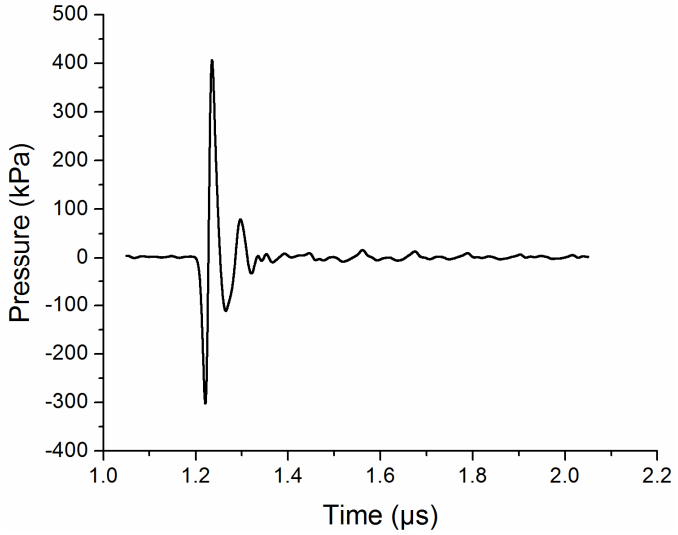

Figure 5.11: Time domain plot of the pitch-catch signal received with the hydrophone from 3 neighboring elements tied together electrically of a 64 element high frequency 1D array. The hydrophone is 1.8 mm away from the transducer.

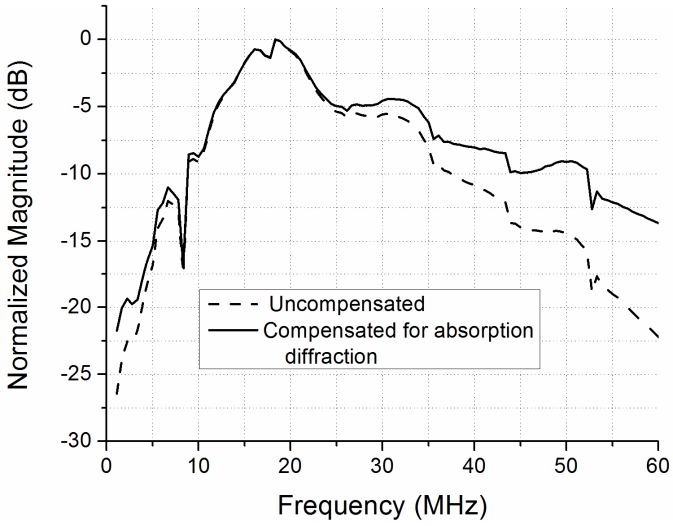

Figure 5.12: A frequency domain plot of the compensated and uncompensated Fourier transform of the pitch-catch data. The -3 dB centre frequency of the compensated plot is 18.3 MHz with a fractional bandwidth of 8.3 MHz.

5.5.4 Pulse-Echo Experimental Setup

The setup of the pulse-echo experiments follows a similar evolution as the pitch-catch experiments. A relatively crude method is used to measure reflected signals for both the low- and high-frequency transducers (though only the results from the high-frequency transducers are presented here). The

transducer is mounted perpendicular to the base of the fish tank. A steel block is placed some distance away. Sound reflected off the block is measured with an element different than the one used to transmit. Later, once the beamformer circuit is available, it is used to re-characterize the response of the low frequency transducer. As with the pitch-catch experiments, it is not used for the high frequency transducer because the pulser signal is too long to effectively actuate the transducer. The experimental setup used for the original characterization measurements is the same as described in Section 4.5.4. The rest of this section discusses the use of the beamformer circuit to perform the pulse-echo experiments.

As in the other pulse-echo experiments an acoustic pulse transmitted from a single element is reflected off a rectangular steel block located some distance away. What is different, is that the signal is measured by the same element used to transmit. The receiving element is connected to a high gain-bandwidth operational amplifier (Texas Instruments OPA 657) connected in a transimpedance configuration with a gain of 10 kΩ. An Analog Devices ADG333A SPDT switch is used to protect the op-amp from the voltage pulse and to switch from transmit to receive mode. The FPGA is used to time the switch. A schematic of the pulser/receiver circuit is shown in Figure 5.13. The pulser circuit is previously shown in Figure 5.6.

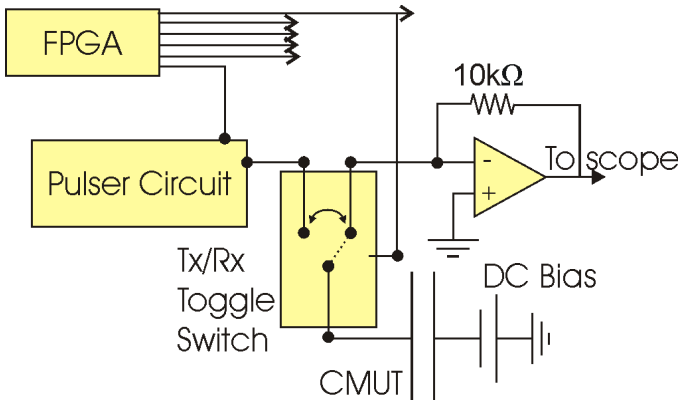

Figure 5.13: Schematic of the pulser/receiver circuit used to isolate the transmit excitation pulse from the receive amplifier. The FPGA is used to toggle the switch.

5.5.5 Pulse-Echo Experimental Results

The steel block is placed 20 mm away from the transducer when testing the low-frequency device. A plot of the time domain signal is given in Figure 5.14 and a plot of the frequency domain pre-and post-compensation for absorption and diffraction is given in Figure 5.15. Prior to compensating for

absorption and diffraction the center frequency is 5.2 MHz with a -6 dB bandwidth of 5.2 MHz. After compensation the center frequency is 6.6 MHz and the bandwidth is 8.1 MHz for a fractional bandwidth of 123%.

In pulse-echo experiments with the high-frequency 64 element array the steel block is placed 3.2 mm away from the transducer, three neighbouring elements are used to transmit the signal and a different set of four neighbouring elements are used to receive the signal. Also, the operational amplifier uses a 10 kΩ resistor for feedback instead of the 4 kΩ resistor used with the first generation devices. A plot of the received time domain signal is shown in Figure 5.16. The Fourier transform of the time domain signal is shown in Figure 5.17. The spectrum is again presented with and without corrections for both attenuation and diffraction. Before correcting for attenuation and diffraction the centre frequency is 13.2 MHz and the -6 dB bandwidth is 12.9 MHz; after, the centre frequency is 14 MHz with a bandwidth of 14.3 MHz, or a relative value of 102%.

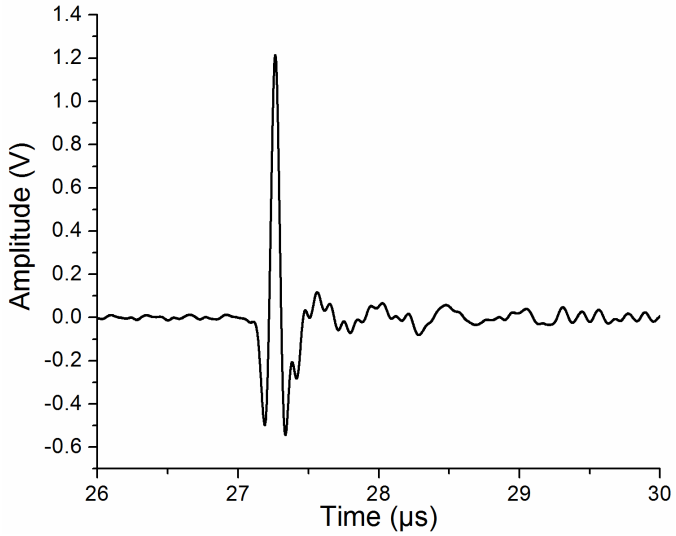

Figure 5.14: A plot of the reflected signal recorded by a single element of a low-frequency 64 element 1D array in a pulse-echo configuration. The steel block is 20 mm from the transducer.

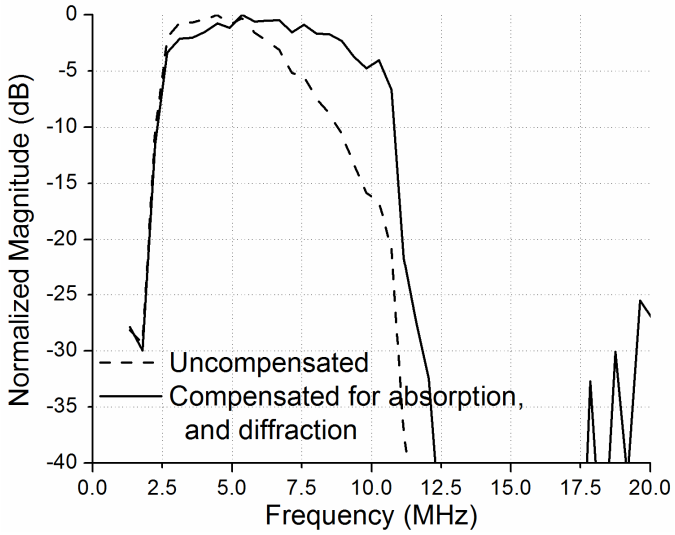

Figure 5.15: A plot of the compensated and uncompensated Fourier transform of the pulse-echo signal from a low-frequency 64 element 1D array. The compensated -6 dB centre frequency is 6.6 MHz with a fractional bandwidth of 123%.

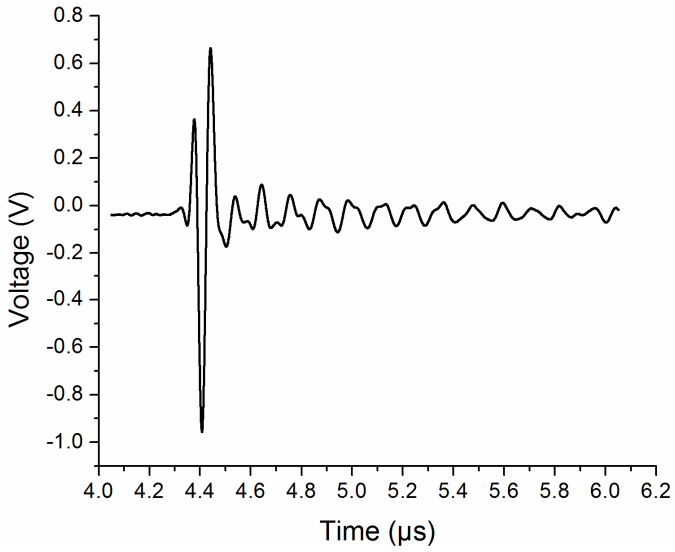

Figure 5.16: A plot of the signal from three transmitting elements reflected off a steel block 3.2 mm away and recorded by a four elements of a high-frequency 64 element 1D array in a pulse-echo configuration.

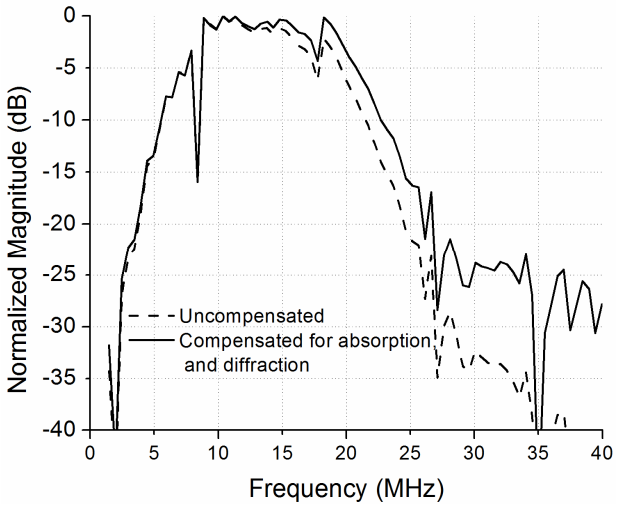

Figure 5.17: A plot of the compensated and uncompensated Fourier transform of the pulse-echo signal from a high-frequency 64-element 1D array. The compensated -6 dB centre frequency is 14 MHz with a fractional bandwidth of 102%.

5.6 Uniformity Characterization

Having obtained nominal operating parameters of the CMUTs further experiments are carried out to determine how uniform their performance is across single transducers, across multiple devices from the same wafer, and from wafer to wafer. Using user deposited silicon nitride as the membrane instead of the device layer of an SOI wafer reduces the uniformity of the completed devices because material deposition rates tend to be non-uniform across a single wafer and among multiple wafers in the LPCVD furnace. In order to quantify this, a number of different measurements are made in both air and immersion. The first set of measurements determines the uniformity of the resonant frequency across a single transducer. Next, the transmit and receive uniformity in immersion across a single transducer is measured. The uniformity across a wafer and from wafer to wafer is determined by measuring the resonant frequency in air of a subset of elements.

5.6.1 Resonant Frequency Uniformity Across a Single Transducer

The resonant frequency of each element of a low-frequency 64-element 1D array is measured to determine uniformity across the transducer. This is done by measuring and averaging together the resonant frequency of 5 cells from each of the 64 elements using a Polytec OFV-5000 single point vibrometer with a high frequency DD-300 displacement decoder. The element is excited with a 30 V unipolar pulse from the beamformer pulser. No bias voltage is applied. A plot of the average resonant

frequency obtained from each of the elements is given in Figure 5.18. The mean value obtained is 14.4 MHz with a standard deviation of 89 kHz or a relative value of 0.62%.

The position of each of the 5 measured cells within an element is the same for each element. This is important as the position of the cell within the element can have an impact on the measured resonant frequency due to the complex acoustic interaction between neighboring cells and elements occurring both through the substrate, the membrane, and the cell walls. Using a network analyzer to measure the resonant frequency of each element would be a preferable method to using the vibrometer because it would provide a faster method to average across the entire element. However, this was not possible as only 4 elements had the necessary ground-signal-ground contact pads necessary to use a network analyzer.

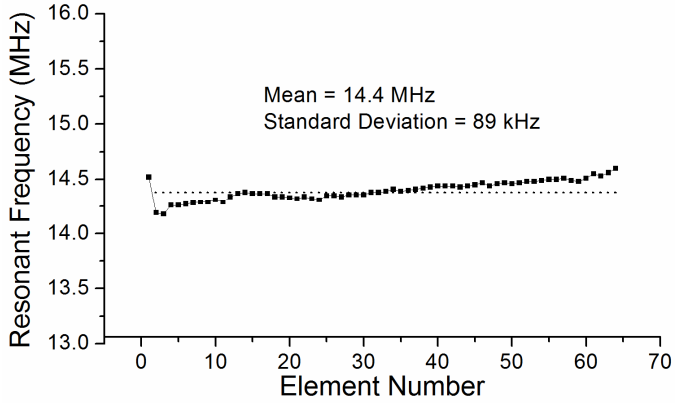

Figure 5.18: A plot of the resonant frequency of each element of a 64 element array.

5.6.2 Immersion Transmit and Receive Uniformity

Measuring the uniformity of an array in immersion is important for two reasons, first to gain further insight into how non-uniformities in the fabrication process can manifest themselves while the device is operating. The other is that when using the array as an imager the relative sensitivity of each element has an impact on the reconstructed image. The differences between the elements can be compensated for to a certain extent during image processing.

Uniformity in immersion is characterized by measuring the transmission pressure of 32 different elements and also the receive sensitivity of 32 elements to an external ultrasound pulse generated from a piezoelectric transducer. For the transmission experiments, a hydrophone is mounted 30 mm away from the transducer on a translation stage. Each element is biased at -60 V and driven with a 30 V pulse. The position of the hydrophone is adjusted to ensure that it is directly in front of the element

being measured. The average peak-to-peak pressure is 51.1 kPa with a standard deviation of 1.7 kPa, or a relative value of 3.3%. The signals are not corrected for attenuation or diffraction.

To test the receive uniformity of 32 elements, a commercial piezoelectric transducer (Panametrics-NDT V327-SU) driven by a commercial pulser/receiver (Panametrics 5073) located 140 mm away is used to generate acoustic pulses. The piezoelectric transducer is mounted onto the translation stage to ensure that it remains directly in front of the element being tested. The signal received by the CMUT is amplified using the same transimpedance amplifier circuit shown in Figure 5.13. The average measured amplitude after amplification is 887 mV, with a standard deviation of 102 mV. Element 7 is a very clear outlier and is due to an incorrect feedback resistor in the op-amp circuit used for that channel. Discounting element 7, the average measured amplitude is 870 mV with a standard deviation of 36 mV, or 4.1 %. This response, of course, is a combination of the element sensitivity and the amplifier performance and it is entirely likely that a portion of the non-uniformity is due to amplifier variation. The receive values are used to scale the values obtained during image formation. A plot of the immersion transmit and receive uniformity results is given in Figure 5.19.

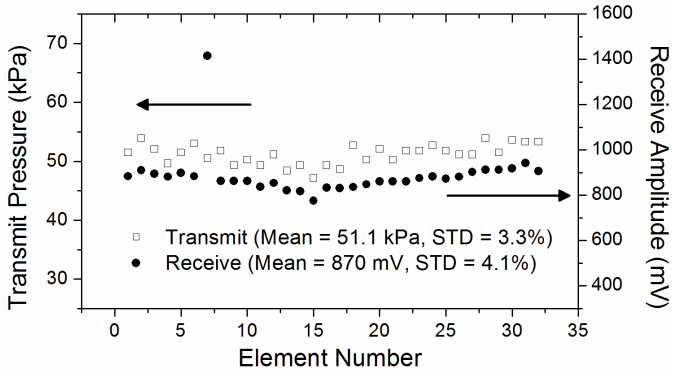

Figure 5.19: A plot of the transmission pressure generated from 32 different elements as measured by a hydrophone (open squares) 30 mm away and the received signals from the same 32 elements with signal generated from a piezoelectric transducer located 140 mm away (closed circles). The mean and standard deviation (STD) of the receive data excludes the data from element 7 (it is clearly an outlier).

5.6.3 Pan-Wafer and Wafer to Wafer Uniformity

While the uniformity across a single device is expected to be good given that the LPCVD deposited membrane thickness should not vary much over the scale of a single die, it is not certain that the same will hold true across an entire wafer and from wafer to wafer. When depositing low-stress silicon nitride in an LPCVD furnace it tends to deposit on the first surface it comes across [112]. As a result the wafers closest to the gas sources tend to have more material on them. The edges of individual

wafers also tend to have more material on them than the centers. The latter effect is somewhat mitigated by the CMP step as the polishing rate tends to be a little higher at the edge of the wafer than the center. To correct the former, the polishing time can be varied slightly to compensate for the different nitride thicknesses deposited.

To characterize the uniformity across a single wafer and among multiple wafers, an Agilent N5242A PNA-X network analyzer is used to measure the resonant frequency of a number of devices on each wafer of a single process run. As stated before, on each wafer there are many types of device layouts beyond the 64 element 1D array that is focused on here. There are both high and low frequency devices. To determine fabrication uniformity across a single wafer, the resonant frequency of one element from 12 different low-frequency devices is measured using a network analyzer. Using the same setup described in Section 5.5.1, a bias of 10 V is added to the RF signal from the network analyzer to more easily see the resonant frequency. The results from 12 different devices are plotted in Figure 5.20. The measured average value is 14.4 MHz with a standard deviation of 340 kHz, a relative value of 2.4%. Wafer-to-wafer uniformity of the processing run was determined by measuring the resonant frequency of a single element on two devices from each of the nine wafers processed. Of the two measured one of the devices measured is a 64 element array located on the top third of the wafer whereas the other one is a different type of array (typically a 64 element annular array) located on the bottom third of the wafer. Again a bias of 10 V is applied to make determining the resonant frequency easier. The results of this analysis are presented in Figure 5.21. The measured average value is 14.9 MHz with a standard deviation of 460 kHz, a relative value of 3.1%.

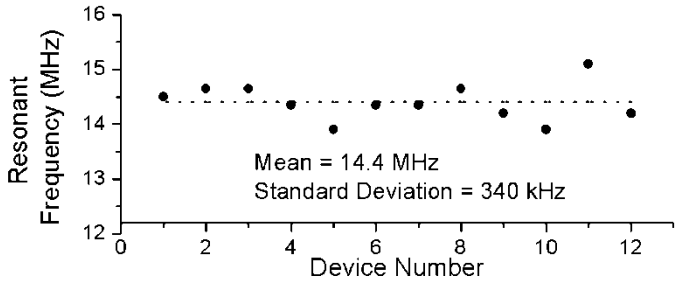

Figure 5.20: A plot of the resonant frequency of one element from 12 different low-frequency devices sourced from a single wafer.

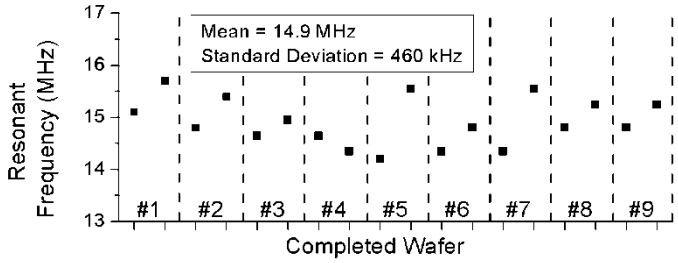

Figure 5.21: Measured resonant frequency of a single element from a pair of transducers sourced from nine different wafers processed during a single run.

5.7 Beamforming Results

With the individual elements of a low-frequency 64 element array characterized, the next step is to study how the elements work together when doing transmit phased array beamforming. To keep the size of the beamformer circuit reasonable only 32 of the 64 elements are driven (the same 32 characterized in the Section 5.6.1). In this section the beam profile of the focused acoustic beam is measured and details of the beamformer are discussed.

5.7.1 Beamformer Circuit Design and Performance

The design of the fundamental components of the beamformer, the voltage pulser and receive amplifier, have been discussed in Sections 5.5.2 and 5.5.4 respectively. The completed beamformer circuit contains 32 copies of the pulser and 32 copies of the amplifier circuit with 32 single-pole double-throw IC relays isolating them from one another. The timing of all of the components is controlled by a Virtex 4 XC4VSX35 FPGA mounted on a Xilinx ML402 test board. The board has a clock frequency of 100 MHz that can be multiplied, using on board functions, to up to 350 MHz. A high frequency clock is important for the transmit beamformer as it defines the timing resolution. For example, to focus a beam 5 mm away at a steering angle of 0°, an element at the centre of the 64 element low-frequency array has to fire 5.4 ns after its neighbour. A 350 MHz clock provides a resolution of ~2.9 ns, sufficient for the above example. However, using the same array but with the focal spot 15 mm away the time difference between the neighboring elements is only 0.9 ns. As the element size shrinks for higher frequency operation the requirements become more stringent.

The control program for the beamformer is written in Verilog and amounts to a look-up-table with all of the delay values for angles -45° to +45° at a fixed depth entered and a counter used to trigger each of the transmit channels at the correct time. The angle of focus is selected from a set of

DIP switches on the demonstration board. Delay values for different focal depths are held in different programs.

5.7.2 Beam Profile Measurements

In this section the method for measuring the focused transmit beam shape is discussed. As mentioned earlier, the element pitch of the array is 200 μm and the centre frequency of operation is ~ 5 MHz. This translates to an element pitch of ~0.8 wavelengths and therefore does not satisfy the half-wavelength pitch necessary to completely avoid grating lobes. In practice though, any grating lobe will only be found at large angles and given the large bandwidth of the transducer they will be of small amplitude [16] discussed in section 2.2.3.

A two-dimensional plot of the acoustic pressure of the focused beam profile is measured by scanning a hydrophone mounted on the translation stage in the azimuth and elevation dimensions and recording the peak-to-peak pressure at each location. The beamformer is programmed such that the acoustic focus is directly in front of the array (θ = 0°) 17.5 mm away. The pulse amplitude is 30 V and the bias voltage is -60V. A contour plot of the obtained beam profile is given in Figure 5.22. The scale of the contour plot is linear with pressure. As the array height is 5 mm, the distance of 17.5 mm from array to hydrophone is still in the near field in elevation and as a result structure in that direction is visible. The distance of transition from the near-field to the far-field is dependent of the aperture of the transducer as well as the frequency of operation. For a rectangular aperture, as is used here, the transition distance is defined as

$$z_t = 0.339\frac{L_y^2}{\lambda} \tag{5.1}$$

where L_y is the height of the transducer (5 mm for this transducer) and λ is the centre frequency of operation [103]. An effort is made to measure as close to the array as possible to ensure that the *f*-number is not too large which would result in a large focal width. The *f*-number is the ratio of focal length to the aperture and directly relates to the minimum achievable spot size, the full-width-at-half-maximum of which can be defined as

$$x_{FWHM} = \frac{1.206\lambda F}{L_x} \tag{5.2}$$

where $x_{FWHM,}$ is the FWHM of the focal line, F is the focal length of the phased array, and L_x is the width of the aperture, in this case 32x200µm = 6.4 mm [103]. In the future a reduced vertical aperture, a fixed cylindrical lens, or another means to focus in the elevation will need to be employed to enable imaging closer to the array surface. The measured full-width-at-half-maximum is 1 mm, which corresponds to a half-angle of 1.6° and agrees reasonably well with equation (5.2). The maximum peak-to-peak pressure measured is 2.1 MPa. The measured pressure values take into account the response of the hydrophone and amplifier but not medium absorption or diffraction.

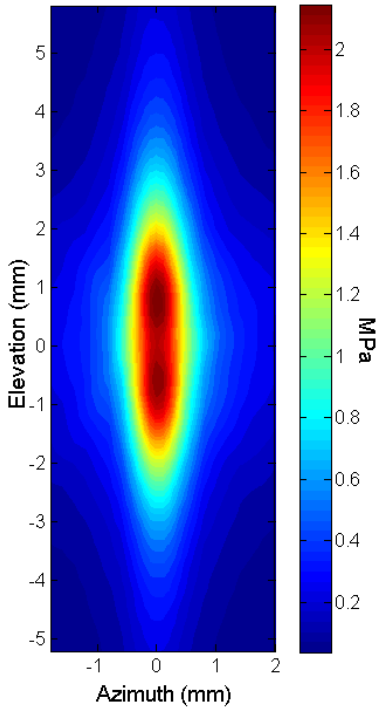

Figure 5.22: A map of the pressure distribution generated by a 32 element phased array imager focused 17.5 mm away from the transducer. The FWHM is measured to be ~1 mm, which corresponds to a half-angle of 1.6°.

5.8 Imaging Results

Demonstration of imaging with the low-frequency 64-element array is done by imaging a wire target. The target consists of 4 vertical wires positioned at different depths and angles from the centre of the transducer array. A photograph and plot of the wire target are given in Figure 5.23. The wires are made of steel and have a diameter of 225 µm. Because the wires are smaller than the resolving power

of the array they serve as point targets that can be used to characterize the imaging performance of the array. The details of this characterization process are given in the following section.

5.8.1 Imaging Method

A 90° sector scan of a 4-wire target is obtained using 32 elements of the 64 element low-frequency array. Both transmit and receive phased array beamforming are performed. As with all other experiments the voltage pulse to each of the elements is 30 V and the DC bias is -60V. The focal spot is scanned sequentially in 1° steps, from -45° to +45° using the FPGA. Two sets of 90° sector scans are taken with focal depths of 15 mm and 20 mm, for a total of 182 unique transmit focal spot positions. Better resolution can be obtained by dividing the sample volume into more depth regions, however the cost is an increase in image acquisition time. A high-speed oscilloscope is used to record the data from each of the 32 elements at each transmit focal spot, for a total of 5824 data sets. The data sampling rate of the oscilloscope is set to 1.25 x 10^9 samples/s. A high sample rate is used to make receive beamforming more straightforward by eliminating the need to interpolate data points. Because the receive beamforming and image processing is performed off-line the additional data and the space it requires is not an issue. In real-time imaging systems the sampling rate is much lower as interpolation can be performed quickly in DSP hardware [16].

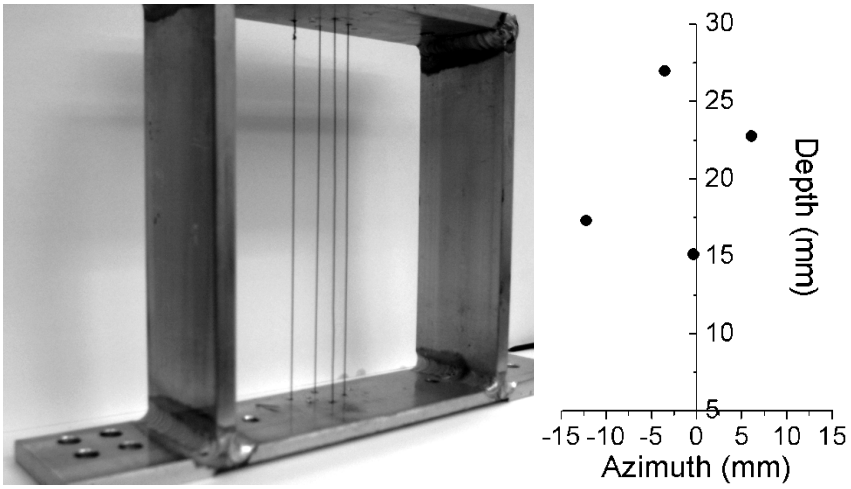

Figure 5.23: Left – Photograph of the wire target used to test the imaging of a 64 element (32 connected) low-frequency linear CMUT array. Right – A plot of the position of the four target wires relative to the centre of the transducer array. The wires have a diameter of 225 µm.

5.8.2 Image Processing Method

The raw amplitude data recorded with the oscilloscope goes through a number of processing steps to convert in to an image. The first step is to correct for the sensitivity of each element using the data shown in Figure 5.19.

Next, the angular response of the elements is compensated for. The sensitivity of the element depends on the angle of incidence of the sound. The response of a rectangular element which is much taller than it is wide is given by

$$D(\theta) = \cos(\theta)\,\mathrm{sinc}\left(\frac{w\sin(\theta)}{\lambda}\right) \tag{5.3}$$

where θ is the angle of incidence, w is the element pitch (200 μm for this array) and λ is the wavelength of sound (taken to be 300 μm) [113]. The compensation value is calculated for each element separately because the angle of incidence is different for each element. This becomes more significant the closer the reflector is to the transducer. A schematic of this is given in Figure 5.24.

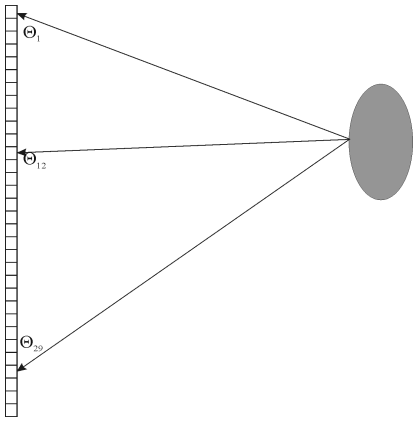

Figure 5.24: A schematic illustrating how for the same reflection point the angle of incidence, and hence sensitivity, is different for each element of the array.

The above mentioned corrections and the receive beamforming itself is performed using custom software written in MATLAB. The software is written to divide the imaged field into an array of (r, θ) positions. Then the delays that would be expected to be seen were there an acoustic reflector at the (r, θ) position are calculated. The sum of the received signal for each (r, θ) position is then determined by shifting the data of each channel by the amount determined in the delay calculation

and then summing them together. If there is a reflector at that particular (r, θ) position then the shift and sum process results in a large amplitude signal. If there is no reflector then the summed signal has a low amplitude. A plot of the signal from a single element is shown on the left of Figure 5.25. On the right is the beamformed signal. Note how only the signal gets amplified whereas the noise, near the front, is largely absent from the beamformed signal. The reflected signal is from the wire closest to the transducer.

After performing receive beamforming the data need to be transformed from a series of A-scans to a B-scan image as is typically used to display ultrasound images. This is done using envelope detection which consists of adding the square of the signal to the square of its quadrature signal and taking the square root.

$$E(t) = \sqrt{S(t)S(t) + S\left(t + \frac{\lambda}{4c_L}\right)S\left(t + \frac{\lambda}{4c_L}\right)} \tag{5.4}$$

c_L is the speed of sound, $E(t)$ is the calculated envelope signal, $S(t)$ is the receive beamformed signal (shown on the right in Figure 5.25) and $S(t+\lambda/4v)$ is the beamformed signal phased shifted a quarter of a period. Converting the signal shown on the right of Figure 5.25 using Equation (5.4) yields the signal shown below in Figure 5.26.

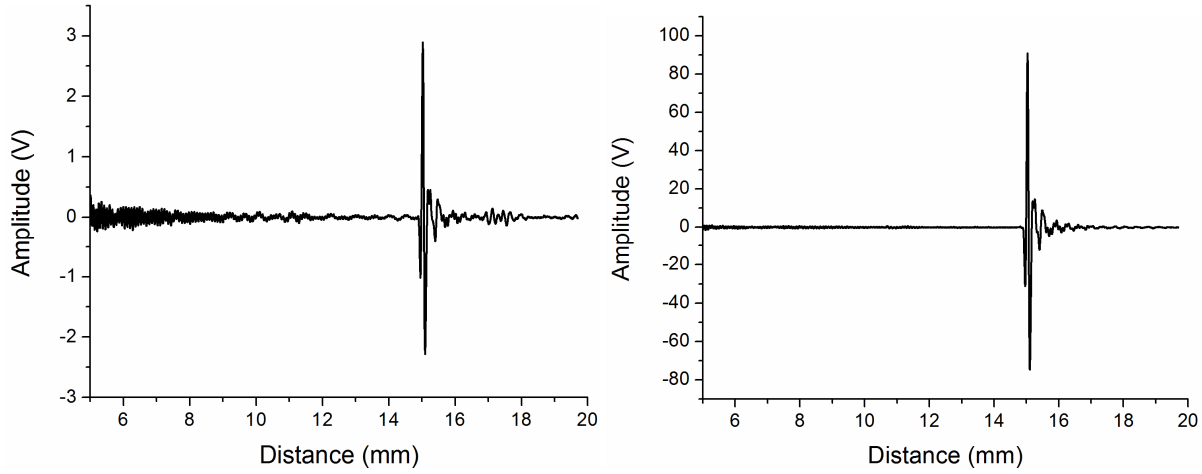

Figure 5.25: Left – The signal from a single element of the array. The sound is reflected off a 225 µm diameter steel wire. Right – The receive beamformed signal from all of the data channels.

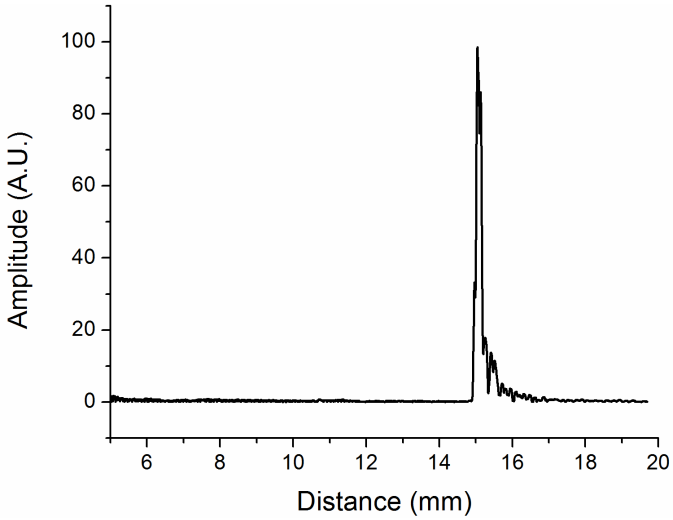

Figure 5.26: The calculated envelope of the receive beamformed signal from the wire nearest to the transducer.

The signal processing, done to this point, yields a series of angularly separated A-scan lines, shown in Figure 5.27. In order convert the data from an (r, θ) polar coordinate system to a Cartesian coordinate system suitable for display on a two dimensional screen bilinear interpolation is used.

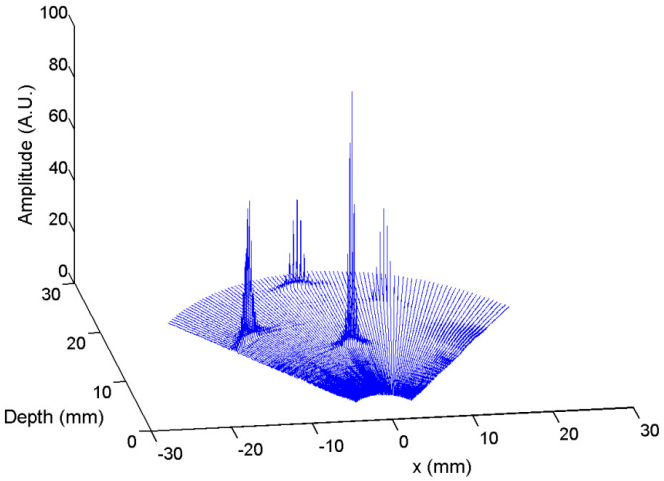

Figure 5.27: A three-dimensional plot of the four wire target after several steps of image processing.

The final processing steps compensate for the attenuation as a function of depth and convert everything to a logarithmic scale. In commercial ultrasound systems, attenuation compensation is typically performed in hardware before data acquisition by using variable gain amplifiers [16].

Essentially, the longer it takes for a reflected signal to arrive at the transducer the greater the amplification. In the work presented here the change in amplification as a function of depth is performed in software.

5.8.3 Imaging Results

The processed B-scan image of the 4-wire target is shown below in Figure 5.28. The dynamic range of the image is 60 dB. The four wires in the image are located where they should be based on the physical measurements made on the target, shown in Figure 5.23. The apparent wider dimensions of wires off-axis and further away from the transducer are expected as the transmit and receive beamforming spot sizes are larger. No apodization is performed.

The axial and lateral line-spread-functions of the nearest wire are shown in Figure 5.29. The -6 dB axial width is measured to be ~130 μm. The lateral -6 dB width is measured to be 0.03 radians which at the depth of 15 mm is ~500 μm. The signal to noise ratio is greater than 100 dB.

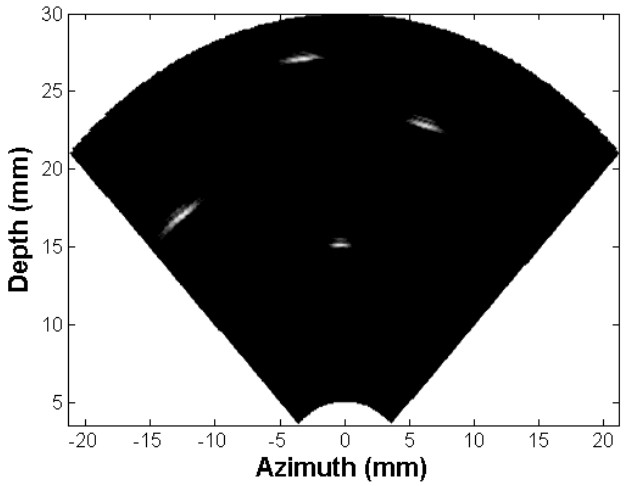

Figure 5.28: Ultrasound image of the four wire target using the low-frequency 64-element (32 connected). The dynamic range of the image is 60 dB.

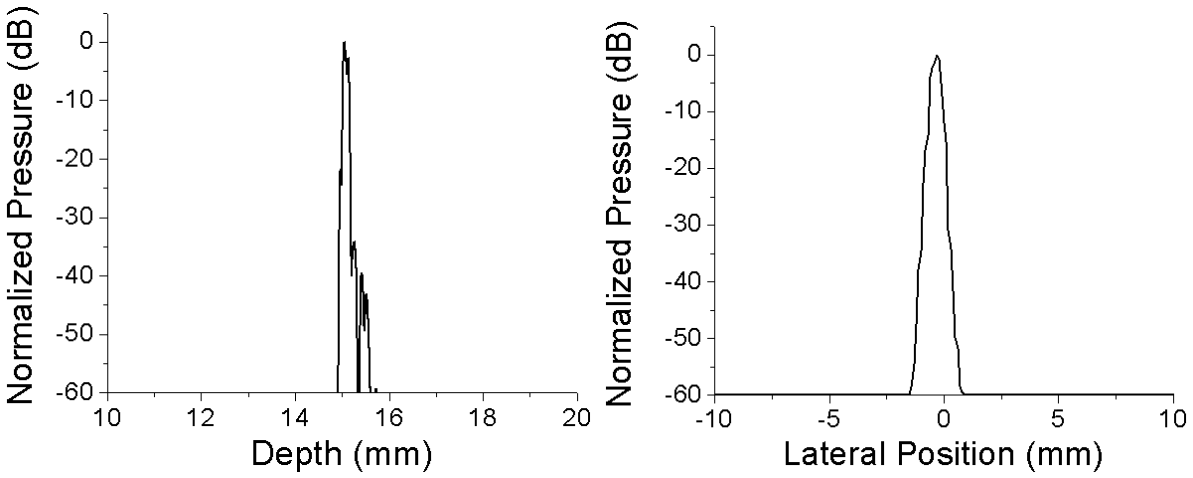

Figure 5.29: The left graph is a plot of the axial profile of the nearest wire. The -6dB width is ~130 µm. The graph on the right is the lateral profile of the nearest wire. The -6dB width is ~500 µm.

5.9 Dielectric Charging

In Section 4.6 the probable causes and effects of dielectric charging and how it relates to CMUTs was discussed. As a follow up, results from charging experiments done with the low-frequency 1D array are included. The devices reported in this chapter incorporate a stoichiometric nitride layer in the insulation. Experience with these devices shows that when they are cycled through collapse and snap-back by increasing then decreasing the bias voltage, charging occurs. One way this manifests itself is that the bias required for collapse increases. The effect can be reversed by switching the polarity of the bias and bringing the device into collapse again for a short period of time. This observation is consistent with what typically happens with silicon nitride as an insulator as has been reported elsewhere [105].

Further experiments are conducted to determine performance as a function of time in the conventional regime (i.e. non-collapse). In this case a simple immersion pitch-catch experiment is setup and left to run for more than 24 hours without interruption. The device is biased at -60V (~80% of the collapse voltage) and excited with unipolar 30 V pulses from the pulser circuit shown in Figure 5.6. The peak-to-peak value of the signal recorded with the hydrophone, located 20 mm away, is recorded periodically and plotted as a function of time. After a little more than 24 hours the bias is returned to 0 V for 20 minutes before increasing it again to -60V. The results are plotted in Figure 5.30. The data indicates that charges are entering the insulator (resulting in the increasing output

pressure) but are not being permanently trapped and that stable and repeatable performance can be achieved as long as the transducer is operated in the conventional (non-collapsed) regime.

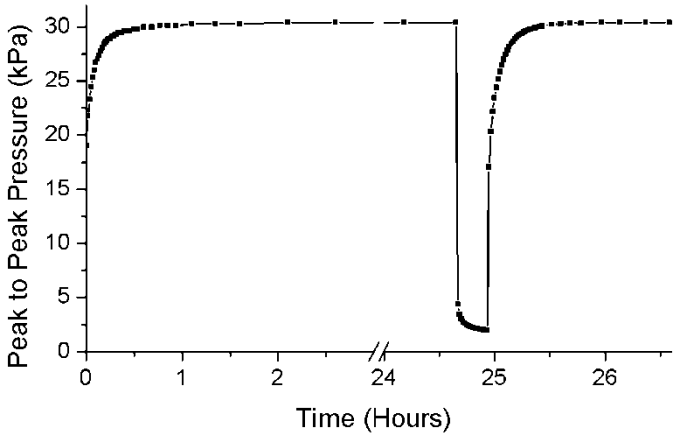

Figure 5.30: A plot of the output pressure of a single element as a function of time. After a little more than 24.5 hours the bias is turned off before being turned back on approximately 20 minutes later.

5.10 Discussion

The primary goal of the work presented in this chapter is to demonstrate the viability of CMUT transducers fabricated using a silicon nitride based fusion bonding process as potential imaging devices. This is achieved by demonstrating relative acoustic bandwidths well in excess of 100%, good performance uniformity, and the generation of a good quality phased-array image using a fairly rudimentary transmit beamformer and receive amplification circuitry.

The data presented in Chapter 4 demonstrated large bandwidths with silicon nitride based fusion bonded CMUTs, but in those cases the voltage pulses had come from a commercial pulser/receiver which generates large amplitude (>100V) pulses. Here, similar results have been demonstrated with voltage pulses generated from a much more modest source consisting of a couple of DC power supplies, a few dollars worth of off-the-shelf components (per element) and a trigger (in this case an FPGA). Pressures in excess of 2 MPa have been demonstrated when 32 elements are focused in the azimuth a relatively large distance (17.5 mm) from the transducer with no focusing in elevation. These results indicate that sufficient pressures and bandwidths will be readily achievable using modest performance electronics likely to be used in the space constraints of an endoscope or catheter.

When discussing the benefits of the fusion bonding fabrication process one of the advantages mentioned is the improved device uniformity which arises largely because the cell cavities are

defined by a well controlled dry etch process and because the membrane is typically the device layer of an SOI wafer. Because the membrane is user deposited silicon nitride in our case it will not have the uniformity in thickness that is available from an SOI wafer. Results here indicate that uniformity across a single transducer is very good, with a resonant frequency standard deviation of 0.67% of the mean resonant frequency. This compares very favourably with transducers fabricated using SOI wafers [37]. Uniformity across the wafer as measured by the resonant frequency yields a larger but manageable standard deviation of ~2% of the mean. The standard deviation of the resonant frequency across 9 wafers is a little higher still at ~3%. The variation on larger scales occurs because the rate of silicon nitride deposition varies with position on the wafer as well as position of the wafer within the LPCVD tube. The fabrication process as a whole, and the deposition parameters in particular, have not been explored to optimize uniformity. This is something that should be done in the future to achieve better performance. In addition to optimizing the furnace parameters it is also possible to reduce wafer to wafer variability by more carefully adjusting the parameters, such as time, of the CMP step.

One of the changes in the fabrication process reported here when compared to the first generation transducer presented in Chapter 4 is the use of a stacked layer of silicon nitride consisting of stoichiometric nitride directly on the conductive substrate followed by low-stress, silicon-rich nitride which makes up the rest of the insulation layer as well as the membrane. This change was made because of the low dielectric breakdown voltage of the silicon-rich nitride that tends to fail at modest electric field strengths (~150 V/μm). This was an issue when the membrane would fail to bond adequately during fabrication and peel off prior to metallization, resulting in the top electrode being placed directly on top of the insulation layer. The result of this was that unless the entire element was fabricated perfectly it was likely to fail. The use of 250 μm of stoichiometric nitride in this generation of devices eliminates the problem. A side effect of this change is that dielectric charging, which had been absent in previous devices, is now observed. It is believed that the somewhat poor dielectric characteristics of the silicon-rich nitride prevented charges from being trapped efficiently. In the current devices charging becomes an issue when the membrane is brought into collapse. When operating in the conventional regime the transducer output pressure increases to a stable point after some time and remains there after multiple power up and power down cycles. This change in behaviour suggests the need to more extensively study the effect of nitride composition on dielectric charging with respect to CMUTs.

Chapter 6 Two-Dimensional Arrays

6.1 Introduction

The final batch of devices reported for this thesis was fabricated in conjunction with the one-dimensional arrays discussed in the previous chapter and as a result they share many characteristics with those devices. All of the devices fabricated in this run are two-dimensional arrays that use a row-column addressing scheme to permit three-dimensional imaging. Details of this scheme are provided in the following section. As with the one-dimensional devices, the 2D arrays are fabricated to have one of two resonant frequencies, 15 MHz or 28 MHz. Due to time constraints the majority of the characterization is done with low-frequency devices. In this chapter the details, advantages, and disadvantages of row-column addressing will be discussed along with the fabrication process, characterization results and initial three-dimensional images.

6.2 Design Objectives

The motivation behind this set of devices is to achieve CMUT devices that are capable of generating three-dimensional images without mechanical motion. The most straightforward, if not the simplest in practice, is to use a fully populated 2D array with individually addressable elements. Much like adjusting the firing pattern of one-dimensional arrays permits two-dimensional imaging, the elements of a two-dimensional array can be fired in a coordinated sequence to generate a focal spot. The focal spot can be raster scanned in all three-dimensions resulting in a volumetric image. This approach can generate the best quality phased array three-dimensional images. The drawback is how quickly the number of elements scales up in conjunction with the complexity of the necessary electronics. For a small 16x16 element array, 256 connections are required, for a 32x32 array the number of elements grows to 1024, at 64x64 it's 4096. There is insufficient room for such a large number of surface traces and so it is necessary to build into the third dimension to connect to all of the elements. In reality, fabricating devices with large number of small elements is reasonably straightforward with CMUTs since the feature dimensions are still relatively large in the domain of semiconductor fabrication. The real challenge is the necessary electronics to drive the transducer and getting all of the information to and from the imager.

A row-column addressing scheme greatly simplifies the drive electronics necessary to achieve a three-dimensional. Implementing this technique with CMUTs allows the height and width of the transducer to be dynamically adjusted thereby enhancing image quality close to the transducer. Details of this scheme and comparisons to other simplifications will be discussed in subsequent section 6.3.

As with the one-dimensional arrays, multiple sizes of arrays have been fabricated that have one of two resonant frequencies, 15 MHz and 28 MHz. To maintain some level of consistency the 15 MHz devices are referred to as low-frequency devices and the 28 MHz ones are referred to as medium-frequency devices (in contrast to the high-frequency ones of the previous chapter). Of the low frequency devices, 128x128, 64x64 and 32x32 arrays have been fabricated. The bulk of the testing carried out is with the 32x32 arrays as they are suitable for demonstrating functionality while keeping the electronics similar to what is used for the one-dimensional arrays. Medium frequency arrays of 128x128, 64x64, 32x32, and 16x16 elements have been fabricated. The 32x32 and 16x16 medium frequency arrays are sufficiently small to be reasonably packaged into a catheter or an endoscope.

6.3 Simplified 2D Array Techniques

Using all the elements of a 32x32 element array to generate and receive ultrasound would require 1024 voltage pulsers, and 1024 pre-amplifiers, a challenge to fit into a device meant for an endoscope or a catheter. Beyond the pulsers and pre-amplifiers, a means to get the signals to and from the transducer needs to be devised. It is not possible to have all of the elements connected directly to the beamforming/image processing system as that many cables cannot fit into the lumen of a catheter or an endoscope. Some type of multiplexing/demultiplexing circuit needs to be placed by the transducer. There have been successful demonstrations of fully populated 2D arrays with the necessary pulsers and amplifiers fitting in the area underneath the transducer [37]-[40].This is done via flip-chip bonding to a separate custom built electronics circuit. At this point the electronics that drive them are not capable of firing all of the elements together for a transmit pulse, nor collecting all of the data in receive simultaneously [114].

If one is willing to compromise somewhat on image quality there are a many ways to simplify the design while still being able to generate three-dimensional images. These include using a ring array, a sparse array, synthetic phased array or row-column addressing. A ring array, as the name suggests, is a ring of many individually addressable elements. A common number of elements is 64 or 128 [41]-

[42]. Because the elements are distributed in a two-dimensional field it is possible to recover three-dimensional data from the sample. Another benefit is that the ring can be mounted on to the end of a catheter and if the centre of the ring is removed the aperture can be used to bring tools to the area being imaged, such as angioplasty balloons or cauterizing tools as an example. The drawbacks are a lower signal to noise ratio as the area actually used for transmitting is quite low.

A sparse array is similar in some ways to a ring array, only a subset of the total elements are used to transmit or receive. By reducing the number of elements used for transmit and receive the system as a whole is greatly simplified. Selecting the correct subset is key to maintaining a reasonable centre-lobe and low side-lobes. For example, if the transducer aperture is reduced by not using the outside elements, the beam width increases. If the internal elements are disconnected the effective pitch increases and grating lobes become an issue. Much research has been done on intelligently choosing which elements to use to maximize the simplification of the transducer while minimizing the penalty in image quality [115]-[118]. This can be achieved by selecting different sets of elements for the transmit and receive apertures such that the combined aperture minimizes side lobes [117]. In general, the background signal levels away from the main lobe scale inversely with the number of elements used [117].

Synthetic phased array imaging is a technique whereby an image is reconstructed from the sequential firing and receiving of individual elements [118]-[122]. By firing each element on its own and listening for the reflection it is possible reconstruct an image from all of the data. The drawback of this method is that it can take significantly more time to acquire all of the data, making real-time imaging more difficult. Also, the signal-to-noise ratio suffers due to do the significantly reduced transmit power.

In row-column addressing the top and bottom electrodes of the transducer are set orthogonal to one another with the result being essentially two orthogonal 1D arrays in a single transducer. There are a few ways to drive a transducer with this type of construction. In one method, one set of electrodes is used to transmit, the other to receive [123]-[125]. As an example, assume the column electrodes are connected to the voltage pulsers; the row electrodes are connected to ground. This essentially functions as a one-dimensional array and is able to generate line focus. To receive, a set of the column electrodes are connected to ground and a set of switches disconnects the row electrodes from ground and connects them to receive amplifiers. In effect, transmit beamforming is performed in azimuth and receive beamforming is performed in elevation. The combination of the two types of

beamforming results in the generation of a three-dimensional image. A more detailed schematic of this method will be presented in the following section. Some of the advantages of this method are that the number of connections of an *NxN* array scale with 2*N* as opposed to N^2 for a fully populated 2D array. Also, fewer pulse-echo events are required to generate an image when compared to the fully populated 2D array. The same number of pulse-echo events are needed to generate a three-dimensional image as are required for a two-dimensional image created with a one-dimensional array [126]. The primary drawback of this method is the reduction in image quality when compared to the fully populated array. This will be discussed in more detail in the following section.

A method that does not yield a three-dimensional image, but is a novel way of using the row-column electrodes to generate an image, takes advantage of the fact that CMUTs require a bias voltage along with the voltage pulses to get efficient actuation. In a scheme reported on by Daft *et al*, a dynamic Fresnel lens is built by alternating the polarity of the bias voltage in different regions [127]-[128]. There is a difference in phase between pulses originating from elements with a positive bias versus a negative bias. Assume the bias is applied along the row electrodes and the pulses are applied along the column electrodes. By alternating the bias polarity on the row electrodes the ultrasound beam can be made to focus in elevation. By changing the pitch of this alternating bias (by grouping rows together) the depth of the elevation focus can be made to change. This actuation method yields a better quality one-dimensional array without the need for an acoustic lens or a greater than one-dimensional array.

6.3.1 Row-Column Beamforming Method Using CMUTs

Row-column beamforming is chosen as the method to generate three-dimensional images due to its compatibility with the silicon nitride based fusion bonding fabrication method developed during this project and the minimal change in the necessary electronics compared to two-dimensional imaging. The method, as mentioned in the previous section, consists of essentially fabricating two one-dimensional arrays orthogonal to one another. The top electrodes are arranged as columns and the bottom electrodes are arranged as rows. Transmit beamforming generates a line focus, the same as achieved with one-dimensional arrays. The position of the line focus can be adjusted in depth and in azimuth as with 1D arrays. Sound striking a surface in the medium is reflected back toward the transducer. The receive amplifiers are connected to the bottom row electrodes where receive beamforming can be performed in elevation. In effect the receive beamforming splits up the

transmitted line focus in to smaller chunks allowing information of the target volume to be obtained in all three dimensions. Figure 6.1 is a schematic of the row-column beamforming method.

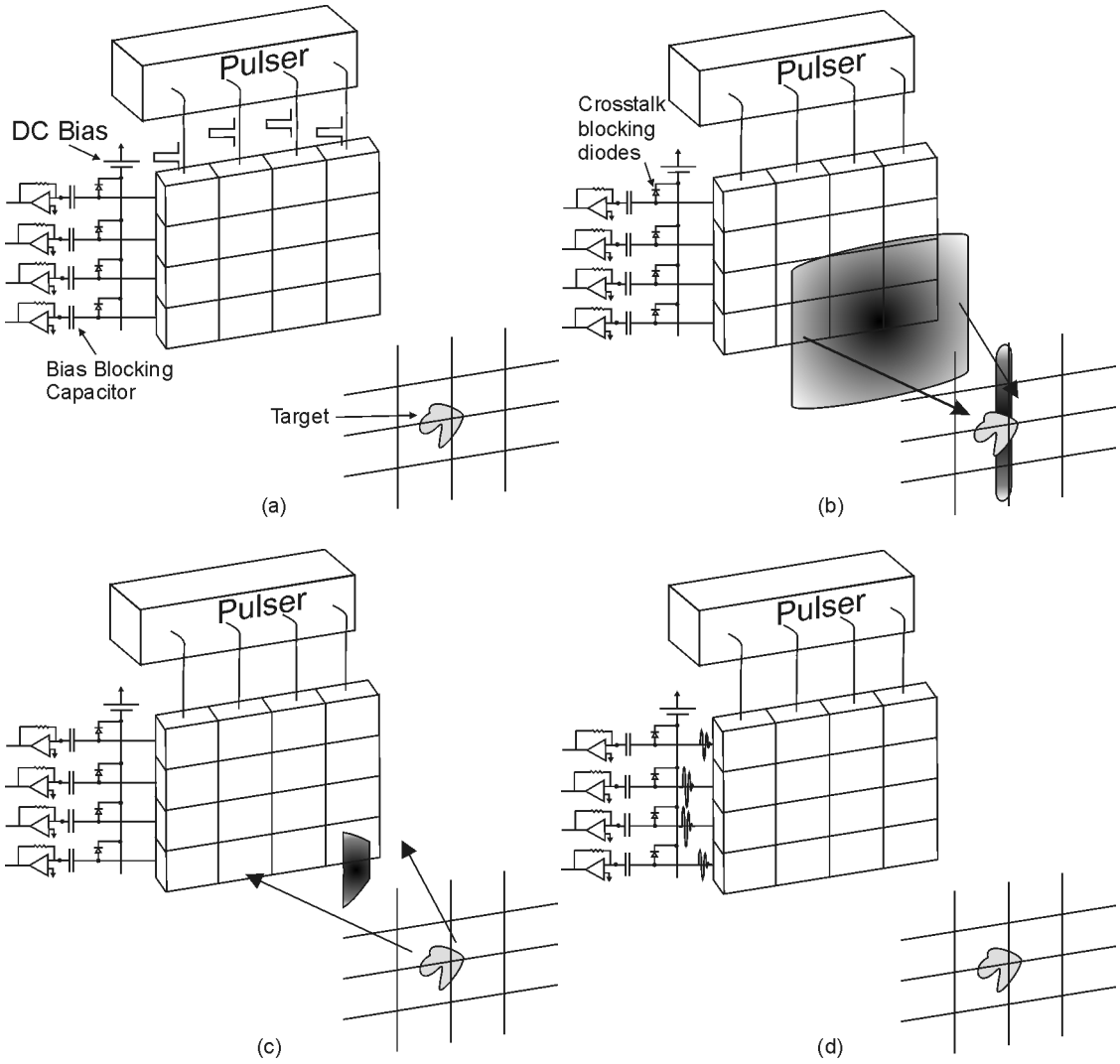

Figure 6.1: A schematic of how row-column beamforming operates. (a) Typical transmit beamforming is performed along the column electrodes which are located on top of the CMUT cells. (b) A line focus is the result of the transmit beamforming and the sound arrives at target. (c) A portion of the sound is reflected off the target back towards the transducer. (d) The bottom electrodes are connected in rows. The reflected sound strikes different rows at different times. The amplified signal is recorded and receive beamforming is performed.

One of the potential issues with row-column beamforming arises from how sound propagates away from the transducer, going from the near-field to the far-field. In the near-field, the pressure perpendicular to the direction of propagation can vary significantly. This arises because sound

emitted from different parts of transducer interferes constructively and destructively with itself over short distances. Sufficiently far from the transducer the rapid variation in pressure no longer occurs as the transducer begins to look like a point source, this is considered the far-field. The intensity profile in elevation at different depths as the signal propagates from the near field to the far field can be calculated analytically if one makes the simplifying assumption that the transducer has piston like action over the height of the transducer. Using equations given by Szabo [103] to calculate the radiation pattern:

$$p(y,z) = \sqrt{\frac{p_0}{2}} e^{i\pi/4} \left[F\left(\frac{y + L_y/2}{\sqrt{\lambda z/2}} \right) - F\left(\frac{y - L_y/2}{\sqrt{\lambda z/2}} \right) \right]$$
$$F(a) = \int_0^a e^{-i\pi t^2/2} dt \tag{6.1}$$

where $p(y,z)$ is the pressure at the position (y,z), p_0 is the pressure at the surface of the transducer, L_y is the height of the transducer and λ is the wavelength of operation. To illustrate the effect, the elevation beam profile of one of the low-frequency transducers is shown at different distances from the front of the transducer. The transducer height is 4.8 mm, and the frequency of operation is assumed to be 5 MHz. Plots of the pressure at different depths are given in Figure 6.2. The beam reaches its minimum width at

$$z_t \approx 0.4 \frac{L_y^2}{\lambda} \tag{6.2}$$

where z_t is the transition depth from the transducer, which using the dimensions discussed above occurs at about 30 mm. This is known as the natural focus. Focusing geometrically, with an acoustic lens or using phased array techniques accelerates the transition distance from near-field to far-field, moving the minimum beam width closer to the transducer.

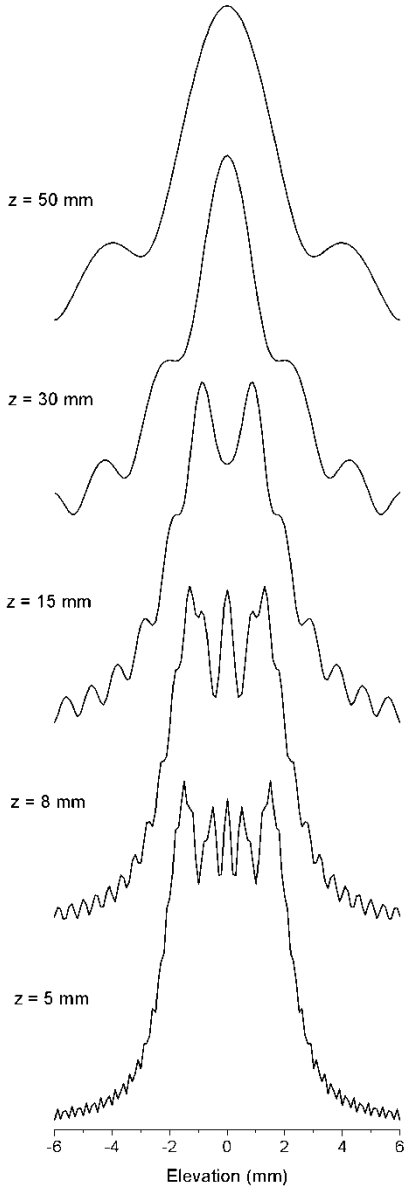

Figure 6.2: Elevation beam profile of the low-frequency transducer at different depths

A row-column beamforming method only focuses in one dimension when transmitting. Assume the transmitting electrodes are the column electrodes and so they focus into a vertical line at a depth z_f. At the focal depth, z_f, the beam waist in the azimuth will be at its minimum and providing the best resolution. In elevation, however, the beam is still in the near-field and therefore has the undesirable structure seen in Figure 6.2. Because the pressure in the vertical dimension can vary quite a bit in elevation it can be difficult to accurately reconstruct the image of the target. The same issues occur in

receive. A reflector close to the transducer will be in the near-field of the receive beam and yield an undesirable signal. For this reason, imaging in the near-field tends to be avoided.

A way to address this issue would be to dynamically control the aperture of the transducer. As can be seen in equation (6.2) the smaller the height (L_y) the shorter the near-field length. When imaging closer to the transducer the effective height could be reduced when transmitting. When imaging further away the full aperture is used. Because CMUTs require a DC bias along with the voltage pulse to efficiently generate sound and a bias to efficiently receive sound there is a means to affect desired aperture control.

Consider transmit aperture control. If the voltage pulses are applied along the columns and the DC bias is applied along the rows we can adjust the effective height of the transducer by not applying a bias to certain rows. Because transducer efficiency is strongly dependent on the bias voltage the rows are effectively off. Schematics of the elevation beam profile with all the rows connected to the DC bias and only half the rows connected is shown in Figure 6.3. The beam width minimum corresponds to the transition from the near-field to the far-field. Of course, as some of the rows are turned off the output pressure of the transducer will go down but the distance to the sample will be shorter as well, meaning less absorption in the interstitial medium.

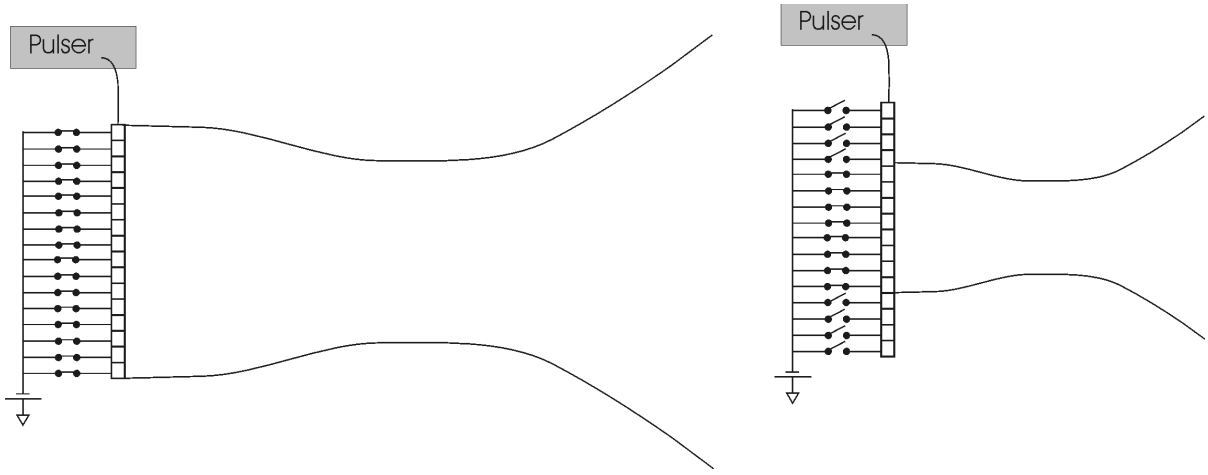

Figure 6.3: Schematic of the effect of turning off the bias to certain rows of the transducer. On the left all of the rows are connected to the DC bias resulting in the largest output pressure and the largest distance from transducer to the natural focus. On the right only half of the rows are connected to the bias (in reality the ones that are off would be connected to ground, and not left as an open switch). The natural focus is smaller and closer to the transducer permitting imaging closer to the transducer.

Similar controls in receive could be implemented. In that case a bias voltage of equal magnitude and polarity as is applied to the rows would be applied to the certain columns to turn them off. The effective bias along the 'off' columns would be 0 V, effectively turning them off and reducing the receive aperture. An additional benefit of being able image closer to the transducer is that the resolution improves as the *f*-number gets smaller ($f\# = F/L$).

A potential problem with turning off rows and columns of the transducer is that with a smaller aperture the minimum beam size increases [see equation (5.2)]. If one uses the transducer in Figure 6.3 as an example, with the bias turned off for half of the rows, only 8 are able to detect incoming sound waves with any level of sensitivity. Reducing the receive aperture height decreases sensitivity and degrades the potential resolution in elevation as well. The solution to this, discussed in section 6.7.1 , is to re-apply a bias to all of the disconnected rows immediately after the transmission pulse has been fired. If this is done before the reflected sound reaches the transducer, then there should be no loss in receive aperture size, and thus performance.

6.4 Fabrication Method

The fabrication method of the two-dimensional arrays is a combination of the process used for the first generation devices (discussed in Section 4.3) and the one-dimensional arrays (discussed in Section 5.3).

The process begins with two $\langle 100 \rangle$ wafers with a resistivity of 1-20 Ω-cm. The electrical properties of the top wafer are unimportant as it is used as mechanical platforms. Those of the bottom are important as the substrate can form a capacitor with the bottom electrodes. First, an 1100 nm thick thermal silicon dioxide layer is grown at 1200°C on the bottom wafer. This serves to electrically isolate the individual row electrodes from one another. This is illustrated on the left of Figure 6.4(a).

Next, an 1100 nm thick p+ doped layer of low-pressure chemical vapour deposition (LPCVD) polysilicon is deposited at 590°C for what will be the bottom electrodes. To improve the resistivity the wafers are annealed at 1100°C for one hour. The resulting resistivity is ~5.5 mΩ-cm. The annealing step increases the polysilicon grain size and makes the surface quite rough with peaks reaching 50-100 nm in height. To facilitate bonding a quick polishing step is required to reduce the RMS roughness to ~2 nm from ~18 nm before polishing. About 100 nm of material is removed.

The row electrodes are then photolithographically defined and a deep reactive ion etch is used to etch through the polysilicon to the underlying silicon dioxide. DRIE is used to ensure that the trenches separating the row electrodes do not get wider. Also, the DRIE tool allows the use of photoresist as the mask instead of oxide. Figure 6.4 (b) shows the polished and etched polysilicon layer. The trench width is ~3 μm.

From this point on the fabrication process is identical used for the one-dimensional arrays and will be covered in brief. An LPCVD process at 800°C is used to deposit 520 nm of silicon nitride on the top wafer (shown on the right side of Figure 6.4 (a)) and 380 nm on the bottom wafer. The silicon nitride on the bottom wafer is a stack of 200 nm of stoichiometric nitride followed by 180 nm of low-stress nitride. The motivation for using two types of nitride is discussed in Section 5.2. The silicon nitride needs to be polished to facilitate bonding. Each wafer is subjected to another short CMP step which removes about 20 nm of material and yields a surface roughness conducive to bonding.

Cell cavities are then patterned and etched into the bottom wafer. The cavity depth is ~165 nm and is shown on the left of Figure 6.4 (c). The two wafers are then cleaned before bonding. The two wafers are fusion bonded at 120°C in a vacuum chamber at 0.5 μbar under a compressive force of 3600 N. The bond is strengthened after a 4 hour anneal at 900°C.

After the silicon nitride on the backside of the membrane wafer has been removed using an RIE step the entire wafer is etched away in a heated 25% KOH solution. The removal takes approximately 5 hours and stops on the silicon nitride membrane, releasing the structure. The bonded and released membrane is shown in Figure 6.4(d).

Next, in the third photolithography step, the bottom electrode contact pads are patterned and etched using a CF_4 RIE process, shown in Figure 6.4(e).

Finally, the metal contact pads and top electrodes are deposited in an e-beam evaporator system. An adhesion layer of titanium is deposited first followed by 100 nm of aluminum. The contact pads and top electrodes are patterned using a lift-off process, shown in Figure 6.4 (f).

The critical dimensions of the completed low- and medium-frequency devices are given in Table 6-1. Scanning electron microscope (SEM) and optical images of the completed low- and medium frequency arrays are shown in Figure 6.5 and Figure 6.6 respectively.

The fabrication yield and failure mechanisms are essentially identical for the two-dimensional arrays as they are for the one-dimensional arrays discussed in the previous chapter.

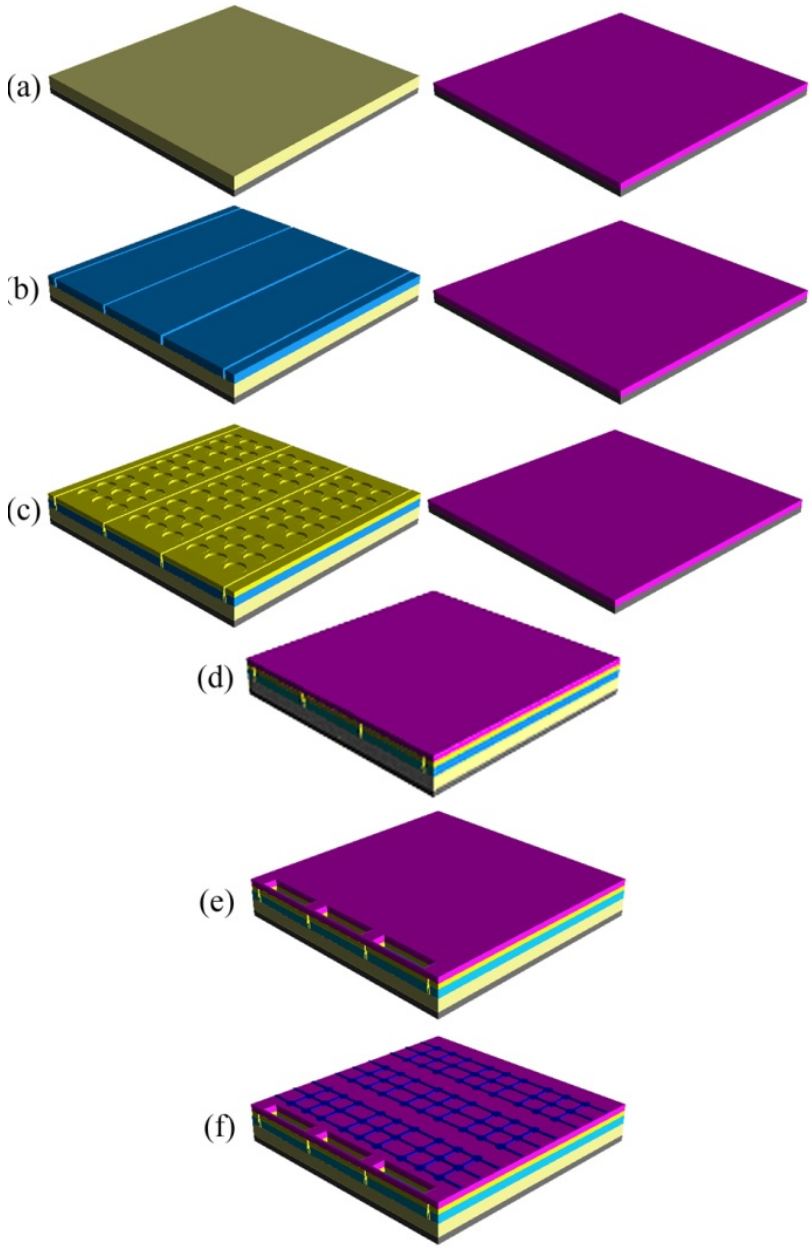

Figure 6.4: Summary of the fabrication process of a 2-D CMUT array. (a) Deposit LPCVD silicon nitride (right), grow thermal oxide (left). (b) Deposit LPCVD polysilicon, polish, pattern and etch row electrodes with DRIE. (c) Deposit LPCVD nitride, polish, pattern and etch cell cavities into bottom wafer. (d) Fusion bond and anneal wafers. Remove top handle wafer. (f) Pattern and expose ground electrode contact pads. (g) Deposit and pattern contact pads and top electrodes using titanium and aluminum.

Table 6-1: Physical dimensions of the low- and medium-frequency 32x32 element CMUT arrays.

Structure	*Low Freq*	*High Freq*
Membrane Diameter (µm)	25	18
Membrane Thickness (nm)	500	500
Electrode Diameter (µm)	15	12
Cavity Depth (nm)	165	165
Insulation Thickness (nm)	190	190
Element Length (µm)	150	45
Element Pitch (µm)	150	45
# of cells per element	30	4

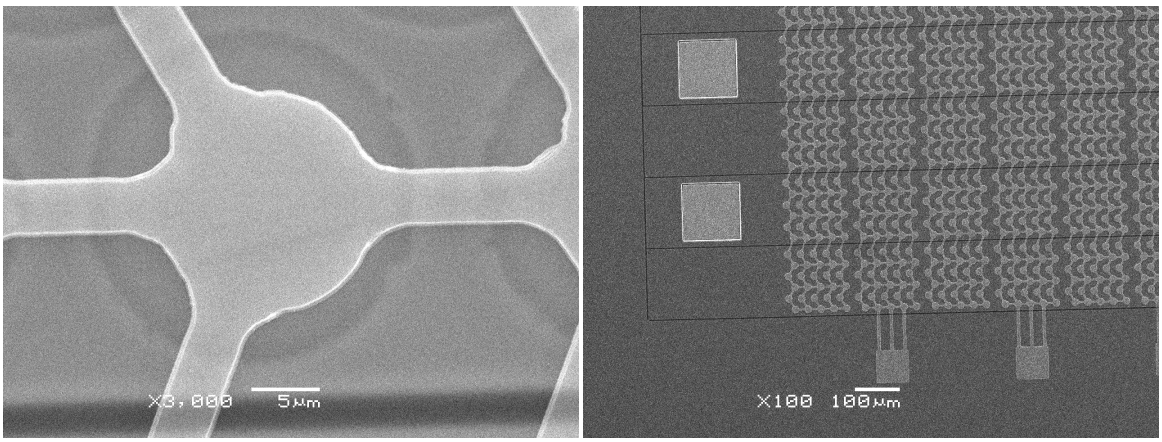

Figure 6.5: SEM images of completed low-frequency 32x32 element array devices.

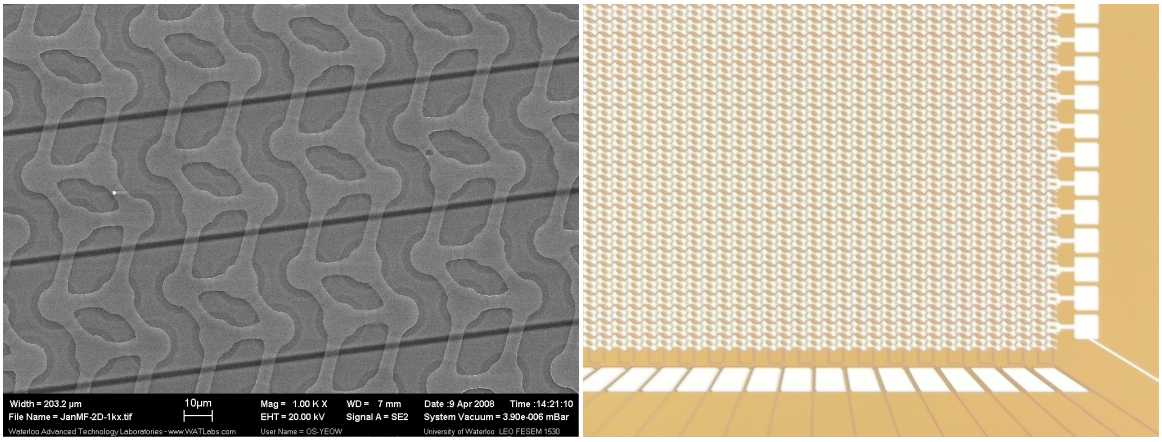

Figure 6.6: SEM and optical images of completed 28 MHz 32x32 element array devices.

6.5 Single Row/Column Characterization

The characterization process carried out for the two-dimensional arrays follows a very similar course as that done for the one-dimensional arrays. The resonant frequency of the 2D arrays are electrically determined with a vector network analyzer, and pitch-catch and pulse-echo experiments are performed in immersion to determine the operating frequency and bandwidth of the devices.

6.5.1 Electrical Characterization

The electrical characterization done with the two-dimensional arrays uses the same setup as was used for the first generation devices, discussed in Section 4.5.1. A ground-signal-ground probe is used to connect the network analyzer to the transducers. The ground contacts are connected to one bottom row electrode and the signal probe is connected to one of the top electrodes. The signal consists of both the RF generated by the VNA and the DC bias signal. The result is that only one element (the intersection of the row and column) has both the AC + DC signal and ground applied to its electrodes. The remaining elements in the signal-connected column have a floating bottom electrode. Both a low-frequency and a medium frequency 32x32 element array are tested electrically. The low-frequency device is biased at 0 V and 60 V (the collapse voltage is 75 V), the medium frequency device is biased at 0 V and 70 V (the collapse voltage is ~120 V). Plots of the real impedance are given of the low- and medium-frequency devices in Figure 6.7 and Figure 6.8 respectively.

In the two above graphs there are unusual features, instead of the single resonant peak that is observed in the impedance plots of the first-generation and 1D devices there are multiple peaks. The

feature is more pronounced at the higher bias voltage. The increased amplitude and the shifting of the peaks is consistent with what is expected of these devices as bias increases (due to increased transduction efficiency and the spring softening effect), the splitting up of the peaks is not. Due to time constraints the nature of the multiple peaks has not been investigated. It is believed they are a result of the floating bottom electrodes of all but one of the elements in the column connected to the VNA. Experience with the 2D arrays indicates that if one of the electrodes of the CMUT is floating actuation is still possible, though the behaviour is somewhat unpredictable. Data to follow in thesubsequent sections do not indicate any unusual behaviour in the performance of the 2D arrays lending credence to the theory that this is an artifact of the measurement setup and not a physical property of a fully connected row-column CMUT array. The resonant frequency in air of the low-frequency device is ~15 MHz and that of the medium-frequency device is ~28 MHz.

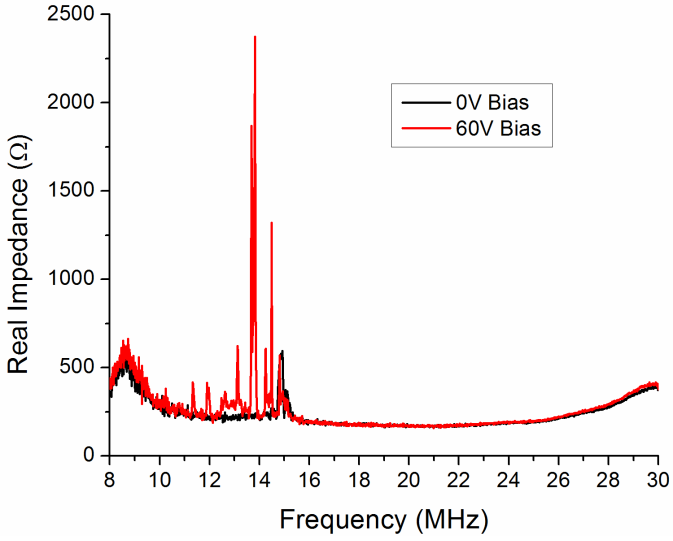

Figure 6.7: Real impedance of a single element of the low-frequency 2D array as measured with a vector network analyzer. The resonant frequency at 0 V is ~15 MHz. The source of the multiple peaks is unknown.

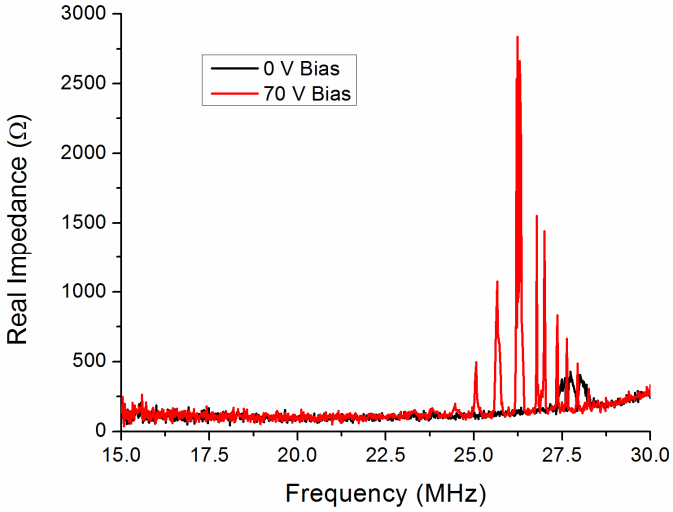

Figure 6.8: Real impedance of a single element of a medium-frequency 32x32 element array as measured with a vector network analyzer. The resonant frequency with a bias of 0 V is ~28 MHz.

6.5.2 Pitch-Catch Characterization

Pitch-catch experiments using a single column of both the low- and high-frequency 32x32 element arrays are performed using two different methods, the same two as used for the one-dimensional arrays discussed in Section 5.5.3. The low-frequency device is tested using the custom-built pulser (shown in Figure 5.6) supplying the voltage pulse and the bias is applied to all of the row electrodes. The transducer is mounted onto the beamformer PCB (to be discussed in more detail in a following section) and held perpendicular to the hydrophone in the same manner as is shown in Figure 5.8. The medium frequency device is driven by the commercial pulser/receiver and DC bias is added to the pulse (via a bias-T) and applied to a single column. All of the rows are tied together to ground so that the entire column can emit efficiently. In this case the transducer and hydrophone are mounted in the same manner as is shown in Figure 4.15, with the transducer and hydrophone not rigidly orthogonal to one another.

Testing of the low-frequency array is done with the hydrophone 20 mm from the transducer. A bias voltage of -60 V is applied. A plot of the received signal and its Fourier transform are given in Figure 6.9 and Figure 6.10. The Fourier transform is corrected for oil absorption, diffraction and hydrophone response. The -3 dB centre frequency of the corrected signal is ~ 5.8 MHz with a relative bandwidth of 5.7 MHz.

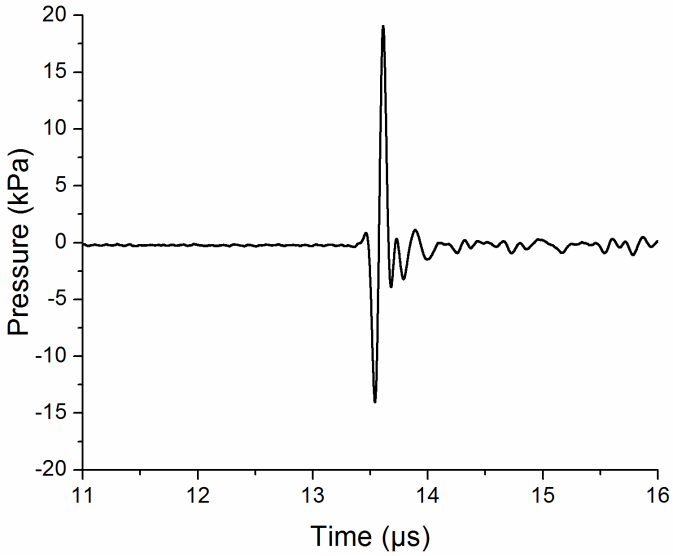

Figure 6.9: Signal received by the hydrophone in a pitch-catch experiment. The hydrophone is 20 mm from the transducer. The DC bias is -60 V and the voltage pulse is supplied the custom built pulser.

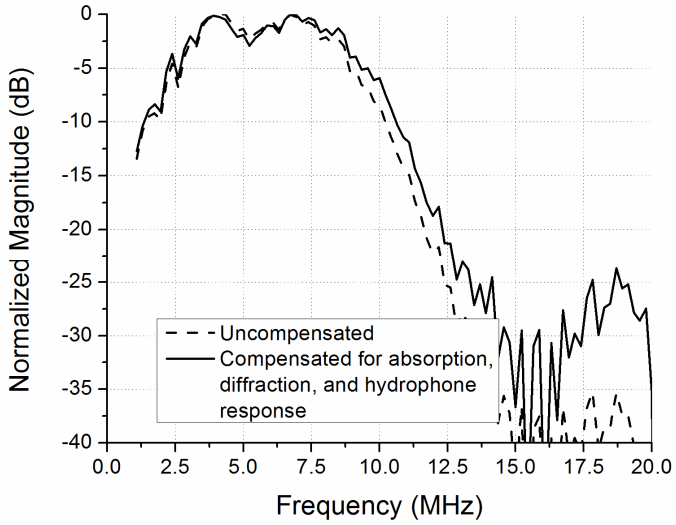

Figure 6.10: A frequency domain plot of the compensated and uncompensated Fourier transform of the pitch-catch measurement. The -3 dB centre frequency of the compensated plot is 5.8 MHz with a fractional bandwidth of 5.7 MHz.

With the medium-frequency device the hydrophone is 10 mm away from the transducer and the bias is set to -100V. Plots of the time and frequency domain response of the single element are given in Figure 6.11and Figure 6.12, respectively. As before, the Fourier transform is corrected for absorption, diffraction, and the hydrophone response. The corrected -3dB centre frequency is 12.5 MHz and the bandwidth is 8 MHz. The frequency domain plot extends to 30 MHz, but the calibration

data supplied by the hydrophone manufacturer only extends to 20 MHz. From 20 MHz to 30 MHz the calibration data at 20 MHz is used. This is far enough away from the peak that any inaccuracy is not significant.

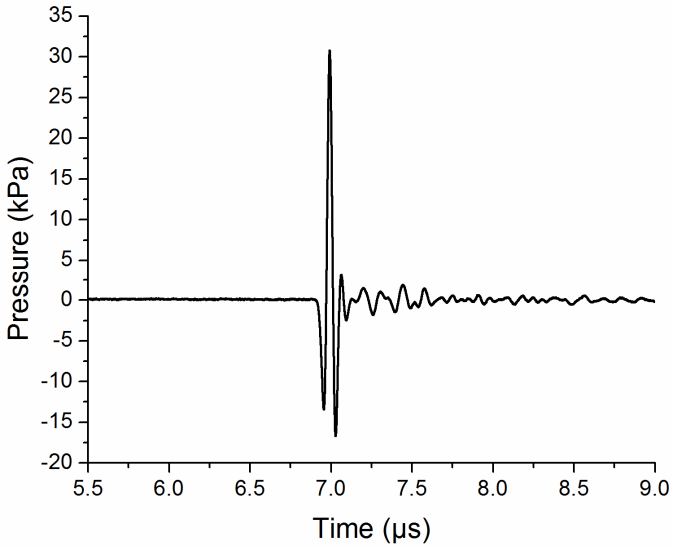

Figure 6.11: Signal received by the hydrophone in a pitch-catch experiment with the medium frequency device. The hydrophone is 10 mm from the transducer. The DC bias is -100 V and the voltage pulse is supplied from a commercial pulser/receiver.

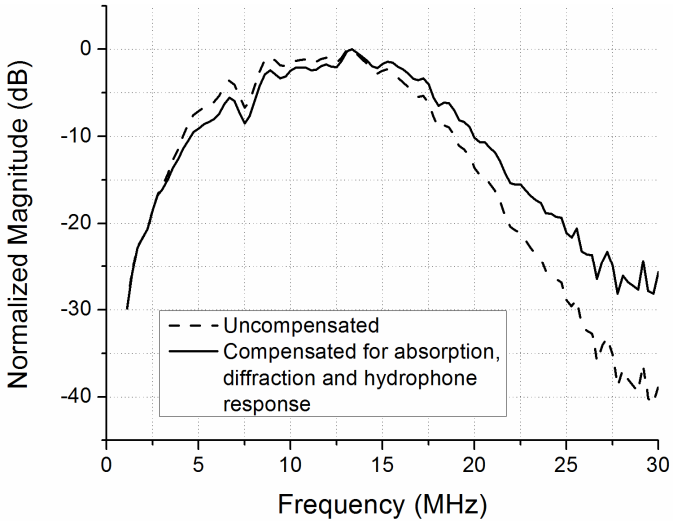

Figure 6.12: A frequency domain plot of the compensated and uncompensated Fourier transform of the pitch-catch measurement. The -3 dB centre frequency of the compensated plot is 12.5 MHz with a fractional bandwidth of 8.0 MHz.

6.5.3 Pulse-Echo Characterization

Pulse-echo experiments have only been performed with the low-frequency 2D arrays to date. The experimental setup is the same as that used for the one-dimensional array (section 5.5.4), in that the transducer is mounted onto the beamformer PCB and sound is reflected off a steel block. In this case the block is 20 mm away from the transducer. Electrically, the 30 V pulse is applied to one column, all of the rows are connected to the -60V DC bias. The reflected signal is amplified with an operational amplifier in a transimpedance configuration with a feedback resistance of 10 kΩ. Time domain and frequency domain plots of the received signal are given in Figure 6.13 and Figure 6.14, respectively. The uncorrected centre frequency is 5.2 MHz with a -6 dB bandwidth of 5.1 MHz; compensating for absorption and diffraction the centre frequency is 5.9 MHz with a bandwidth of 6.5 MHz, or a relative value of 111%.

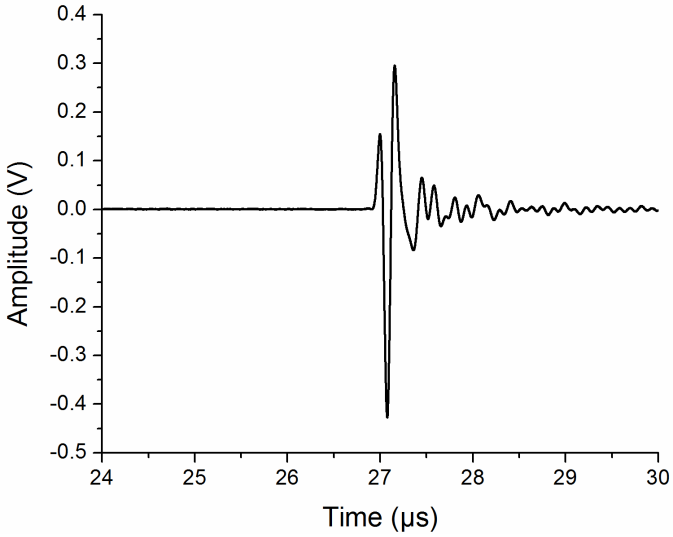

Figure 6.13: Time domain pulse-echo plot from a low-frequency 32x32 element array. Sound is transmitted from on column, reflected off a steel block 20 mm away and measured with a row element.

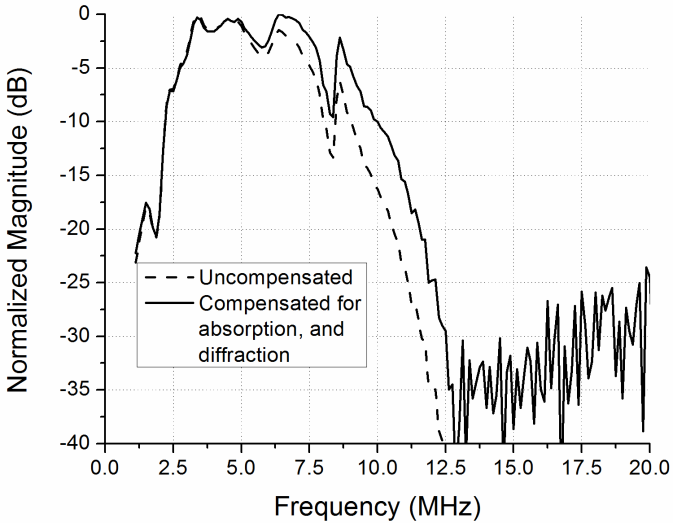

Figure 6.14: A plot of the compensated and uncompensated Fourier transform of the pulse-echo signal from a low-frequency 32x32 element array. The compensated -6 dB centre frequency is 5.9 MHz with a fractional bandwidth of 111%.

6.6 Array Uniformity Characterization

Extensive uniformity characterization has been carried out with the one-dimensional arrays in attempt to determine how repeatable the fabrication process is across a single transducer, a single wafer and from wafer to wafer. Because the fabrication process of the two-dimensional arrays is so similar to that of the one-dimensional arrays no significant difference is expected. For completeness, some characterization of a single array, both in air and in immersion, is carried out.

6.6.1 Vibrometer Results

The uniformity of a 32x32 element low-frequency transducer is characterized using the same vibrometer setup as discussed in section 5.6.1. In this case, however, the voltage pulse is supplied by the commercial Panametrics 5073 pulser/receiver instead of the custom built 30 V pulser. No DC bias is applied. The voltage pulse is applied to a top column electrode while the bottom row electrode is grounded. The element at the intersection of the row and column is the one that is measured. Due to the tedious nature of measuring all 1024 elements with the vibrometer, only a subset are actually measured. In this case every third element in both directions is measured (121 in total). The resonant frequencies of two cells from each measured element are averaged together. The mean resonant

frequency is 15.2 MHz with a standard deviation of 38 kHz, or 0.25%. A surface plot of the measured values is given in Figure 6.15.

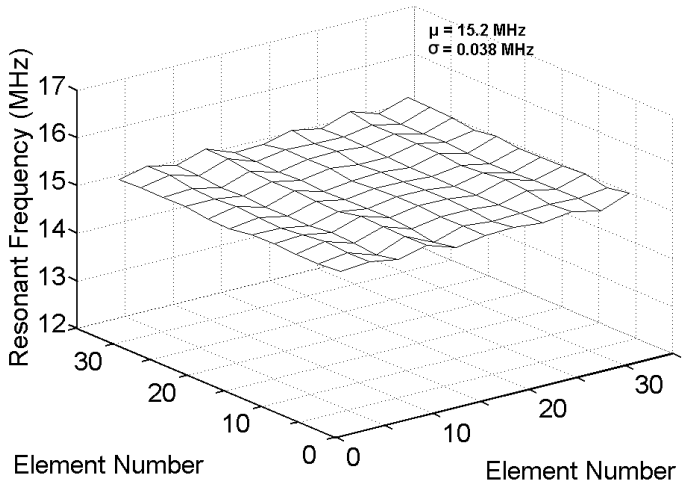

Figure 6.15: Plot of the resonant frequency of 121 out of 1024 elements of a low-frequency 32x32 element array measured with a vibrometer with no DC bias.

6.6.2 Immersion Transmit and Receive Uniformity

The experiments reported in this section are carried out in the same manner as those discussed in Section 5.6.2. To measure transmit uniformity the hydrophone is mounted onto a translation stage 30 mm away and each element is fired individually. Using the translation stage the hydrophone is kept in front of element that is firing. A plot of the measured pressure for each element is given in Figure 6.16. Conversion from amplitude to pressure is done using the hydrophone calibration data provided by the manufacturer. The signal is not corrected for absorption and diffraction. The average peak-to-peak pressure is 38.3 kPa, with a standard deviation of 1.3 kPa, or a relative value of ~3%, similar to what was obtained with the one dimensional arrays.

Receive uniformity of the 32 rows in the array is tested using a commercial piezoelectric transducer (Panametrics-NDT V327-SU) driven by a commercial pulser/receiver (Panametrics 5073) located 160 mm away to generate the acoustic pulses. Two sets of data are acquired, in the first the piezoelectric transducer is mounted onto the translation stage and moved to ensure that it remains directly in front of the element being tested. In the other set of data the piezo transducer remains fixed at approximately the centre height of the CMUT array. A plot of both sets of data is given in Figure 6.17. In the case where the piezoelectric transducer is scanned vertically the average measured signal

is 380 mV with a standard deviation of 28 mV, or 7.4%. Element #1 is at the top of the transducer and element #32 is at the bottom. There is a clear trend upwards as the measurements are made from top to bottom. When the same measurement is made with the piezoelectric transducer fixed in place the response is fairly symmetric about the middle of the transducer. It is believed that the upward trend is due to the impact the bottom of the tank is having on the propagation of sound, acting like a rigid baffle. Due to time constraints this could not be confirmed through further experiments, but a standard deviation of more than 7% is greater than what has been typically observed from the CMUT devices.

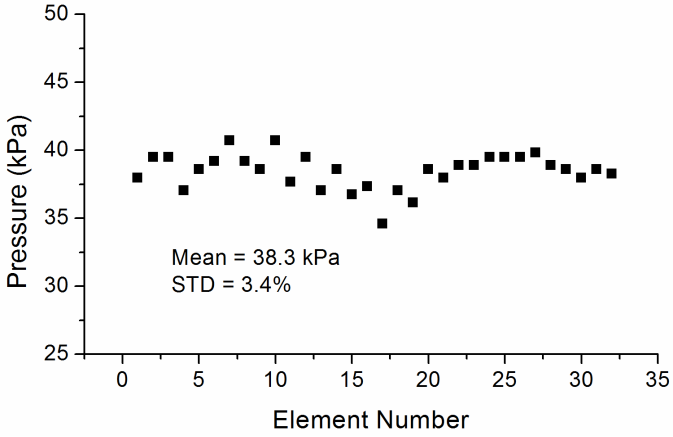

Figure 6.16: Peak to peak pressure measured with the hydrophone 30 mm away from the transducer.

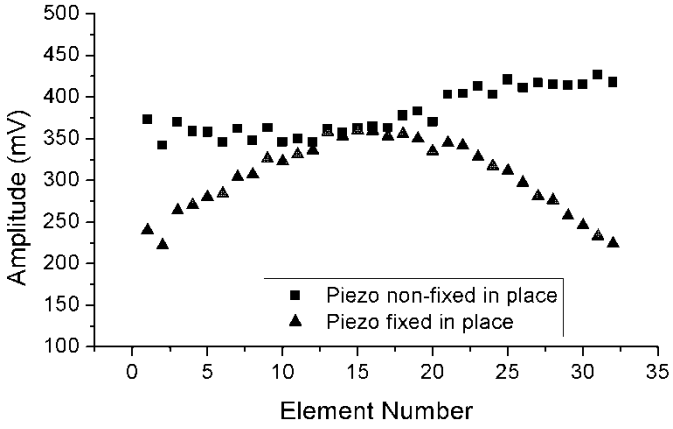

Figure 6.17: Receive uniformity of a low-frequency 32x32 element row-column array measured with the transmitting piezoelectric transducer fixed in place and with it scanned vertically to remain directly in front of the receiving element.

6.7 Beamforming Results

In this section the design of the row-column beamformer is discussed in detail. Also, the transmit beam profiles are measured at different depths as the effective height of the transducer is reduced by turning off the bias to certain rows.

6.7.1 Beamformer Design

For the first generation beamformer, dynamic control is limited to the transmit aperture in elevation. Future work should include dynamic control of the receive aperture as well. Were it not for the desire to turn the bias of certain rows on and off quickly the design of the row-column beamformer would, in many ways, be more straightforward than that used for the one dimensional arrays as the voltage pulsers and receive amplifiers are connected to different contact pads. The pulser circuit is identical to that discussed in section 5.5.2, in that 30 V pulses with a FWHM of ~40 ns are created using a pair of single-pole double-throw switches, a delay circuit and an FPGA. Since the pulser and receivers are effectively isolated from one another by the CMUT no toggling between transmit and receive modes is necessary. The rest of this section will concentrate on the receive portion of the circuit.

The most basic electronics that need to be connected to the row electrodes of the array are the amplifiers and the DC bias. A 4 nF capacitor is used to block the DC bias from saturating the amplifier on each channel. Because all of the receive elements are connected together via the DC bias another circuit element is needed to prevent cross-talk. A diode is used as it effectively blocks the small current generated from a reflected signal while allowing the DC signal to bias the transducer. To be able to dynamically enable and disable rows a switch is needed to either connect the row electrode to a DC signal or to ground. Switching between the DC signal and an open circuit was considered and tested as a method to enable and disable the rows however opening the circuit only reduced the transduction efficiency by a factor of two. Connecting to ground reduces the efficiency to less than 10%. A schematic of an example 8-element receive circuit is shown in Figure 6.18.

The switches in Figure 6.18 must be able to toggle quickly between being connected to ground and the DC bias (between -50 and -80 V) so that the row is effectively off during transmit and on when reflected sound returns to the transducer. The switch ultimately needs to be controlled by the FPGA and so logic level control is required. The time available to make the switch depends on how close to the transducer one wishes to image. For example, imaging 5 mm in front of the transducer

means the row must go from being off to being on in ~7 μs. Another constraint is that the switch between ground and bias cannot occur too quickly or else it will cause the membrane to deflect quickly, thus generating an acoustic pulse. To minimize the 'blind' distance in front of the transducer and to avoid generating unwanted acoustic noise a switching time of 5 μs is a reasonable goal.

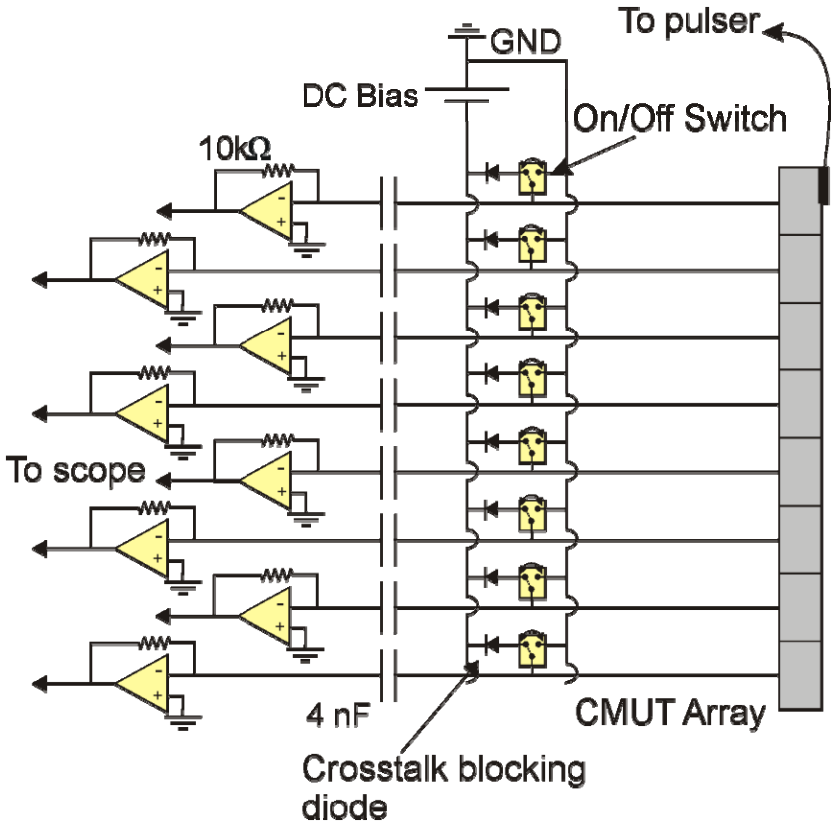

Figure 6.18: Schematic of the basic circuit structure used to permit enabling and disabling of select rows of the array. Switching between DC bias and ground effectively allows the dynamic control of the height of the transducer giving some simple control of the vertical beam profile. The pulser circuit is not shown but is connected to the rows of the array.

An off-the-shelf switch that would meet the above requirements is not readily available. The solution taken is to build a half-H-bridge circuit out of an n-channel and a p-channel MOSFET. The n-channel gate is driven by a PNP bipolar junction transistor which in turn can be turned on and off with logic level voltages. A schematic of the circuit used to drive the receive channel of a single element is shown in Figure 6.19. Connected to each row electrode are the half-H-bridge (consisting of a p-channel and an n-channel MOSFET and a PNP BJT), a diode and a transimpedance amplifier. In Figure 6.19 there is a break shown between the half-H-bridge and the SPDT switches to the left. This is because there is only one set of the SPDT switches to control the beamformer. These switches are

controlled by the FPGA to toggle in conjunction with the voltage. Not shown is a set of switches that reside between the SPDT switches and the half-H-bridge. This gives the ability to disconnect the right side of the circuit from the left side and connect it to fixed values (0V for the p-channel gate, and -5V for the PNP BJT base) so that the row remains biased the entire time. This is of course necessary because without it all of the rows would be unbiased during transmit and little sound would be generated. Also not shown is the circuitry that permits connection of the row electrodes to a positive bias. This is necessary so that the effects of dielectric charging can be reversed. The polarity of V_{bias} cannot simply be swapped as it would damage the transistors. The 2.7 kΩ resistor between the p-channel MOSFET and ground is there to prevent a quick discharge of the row as it is turned 'off' and the acoustic pulse that would result.

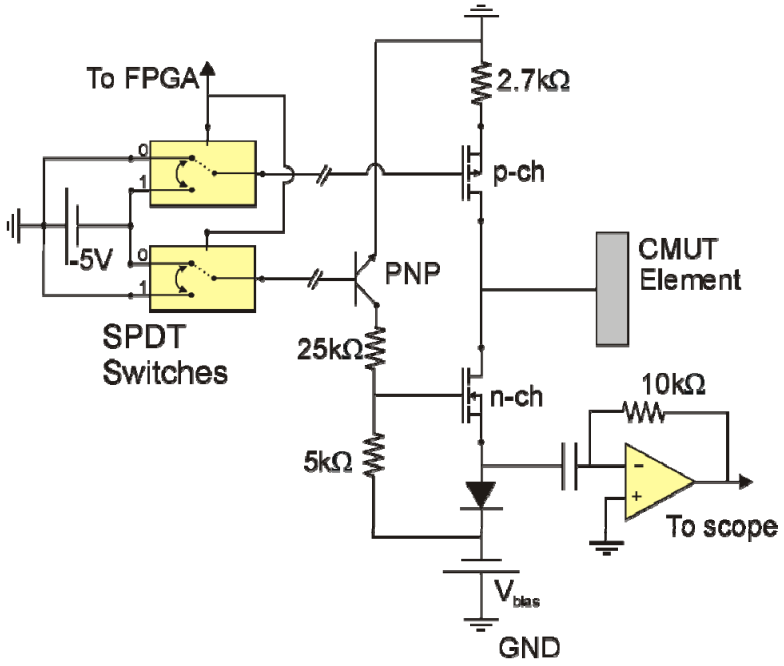

Figure 6.19: A more detailed schematic of the circuit used to toggle a row electrode between bias and ground. The FPGA controls the timing of the SPDT switches such that the row electrode is connected to bias, thereby turning it on and ready to receive, immediately after the transmit voltage pulse is sent out.

The functionality of the circuit shown in Figure 6.19 is fairly straightforward if we consider the p-channel and n-channel MOSFETs as just switches. To turn the row off, the p-channel switch is closed and the n-channel switch is open. The potential on the row is therefore 0V, and it is effectively off. Immediately after the transmit voltage pulse has been fired the switches toggle, such that the p-channel is open and the n-channel is closed. Current then flows from V_{bias}, through the diode to

charge up the row, turning it on. The PNP BJT is used to convert the -5V of the switch to the ~ -60V needed to open and close the n-channel transistor. Any signal received by the CMUT passes through the n-channel transistor and through to the op-amp. The DC blocking capacitor value is 4 nF, sufficiently large to allow the signal to pass through relatively unattenuated. Any received signal does not pass through the diode, thereby minimizing electrical cross-talk between the elements.

A demonstration of the timing of the circuit is shown in Figure 6.20. The figure shows the potential at the row electrode as it goes from being in the off (ground) state to the on (-60V) state. The time to go from off to on is about 1.2 µs. The jump from 0V to 5V in the row electrode potential at around 1 µs indicates when the 'off' to 'on' change is actually triggered by the FPGA. The exact reason for the 5V jump and the delay in switching to -60V is unknown. It is an issue with the switching circuitry that has yet to be debugged.

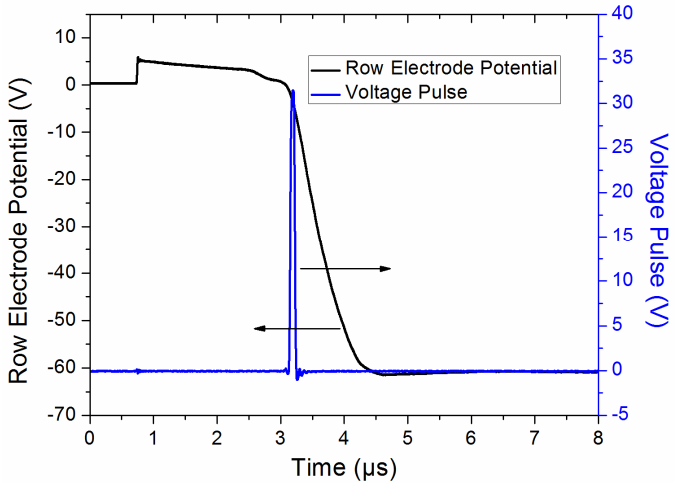

Figure 6.20: Plot showing the potential at the row electrode going from 0 to -60 V immediately after the voltage pulse is fired. With a bias of -60 V applied the row is able to receive signal.

An important consideration is what, if any, change is there in the sensitivity of the element as a result of quickly being switched on and measuring a signal. Two pulse-echo experiments are performed with one of the columns used to transmit. In the first experiment all of the rows are biased and no toggling takes place. In a second experiment two rows in the middle of the transducer are toggled, meaning they are off during the transmit event and are then turned on to measure the reflected signal. The results of the two experiments are shown in Figure 6.21. Because two of the 32 rows are not transmitting in the toggled data set, a rough expectation of the drop in amplitude would be ~6%, though it is not that straightforward as there is also going to be a change in the pressure

distribution of the beam which affects the measured signal The two graphs in Figure 6.21 indicate that there is not a significant change in the shape of the echo signal, but there is an 11% drop in peak-to-peak amplitude. Also visible in the top graph is a small oscillation before the main pulse which is due to the small 5V jump seen in Figure 6.20 when the FPGA triggers the row to go from 'off' to 'on'. A better experiment that would examine only the change in sensitivity due to toggling would be to use a pitch-catch setup where the transmitting transducer is triggered by the FPGA such that the acoustic pulse is coincident with the toggling of the row electrode. Time considerations prevented setting up of this experiment.

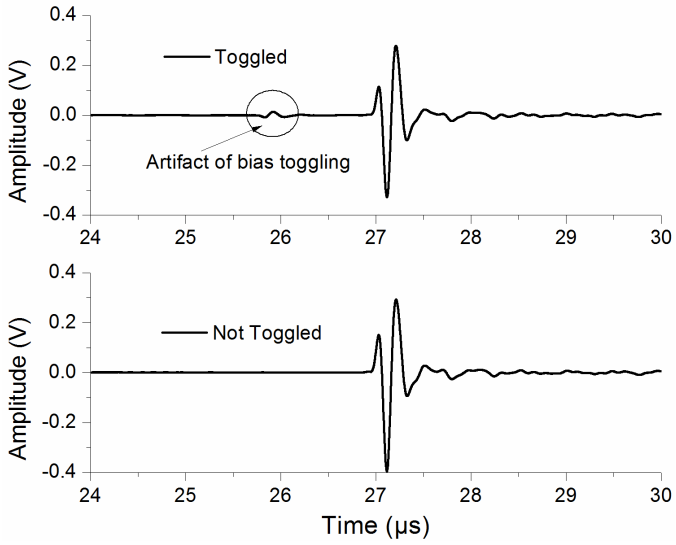

Figure 6.21: Plots of the pulse-echo signal received from one row of the 32x32 element array. Top-The row is toggled between the 'on' and 'off' state. Bottom – The row is kept 'on' the entire time. The toggling causes the signal to drop by ~11%, but there is no significant change in the shape of the pulse.

6.7.2 Beam Profiles in Elevation

In this section the effect of controlling the height of the transducer array by turning off rows on the vertical beam profile is explored. Because transmit beamforming is done using the column electrodes only focusing in the azimuth is possible, the result is a vertical focal line that is narrow in the azimuth (*x-dimension*) and broad in elevation (*y-dimension*). By appropriately adjusting the height of the transducer it is possible to adjust the profile of the vertical line from a multiple lobe structure to a narrower single lobe structure near the transducer. This is characterized using a pitch-catch experiment where all columns of the array are used to focus at the hydrophone directly in front of the middle of the CMUT transducer, such that the scan angle is 0°. The hydrophone is mounted on a

translation stage and is moved vertically through the line focus to map out the pressure in elevation. The distance of the hydrophone is varied in 5 mm steps from 5 mm away to 20 mm away. At each depth the effective height of the transducer is set to various values by turning off the bias to a select number of rows. The bias is set to -60V and the pulse amplitude is 30V.

With all 32 rows biased the vertical aperture of the transducer is 4.8 mm, using Equation (6.2) the transition from near-field to far-field should occur at approximately 30 mm from the array assuming a wavelength of 300 μm. Closer to the transducer than this and the elevation profile will exhibit a multi-lobe structure as shown in Figure 6.2. The first profile scan is made with the hydrophone 20 mm away from the transducer. A plot of the pressure as a function of position is given in Figure 6.22. With the full aperture the double lobe structure is clearly visible. Reducing the vertical aperture to 24 rows from 32 narrows the beam profile while also increasing the peak pressure. Further reducing the number of firing rows to 22 rows narrows the beam further to a FWHM of 3.0 mm but the maximum pressure is lower.

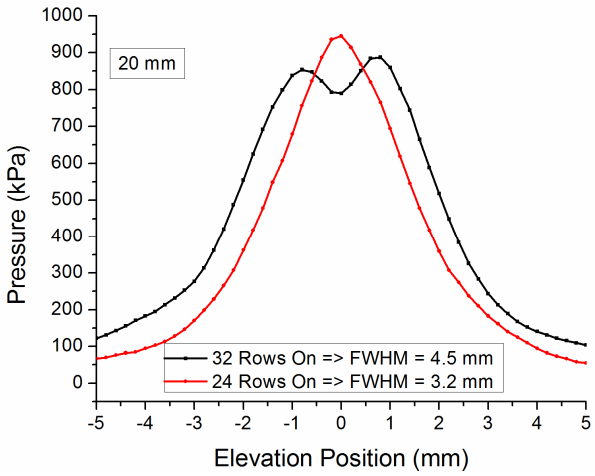

Figure 6.22: Vertical profile of the focal line of a 32x32 element low-frequency row-column CMUT 20 mm from the transducer.

The experiment is repeated at depths of 15, 10, and 5 mm with the data shown in Figure 6.23. At a focal depth of 15 mm with all of the rows firing the FWHM of the beam height is 4.3 mm, with 18 mm on it is 2.7 mm. At a focal depth of 10 mm the FWHM of the beam height with all the rows on is 4.5 mm, with 14 on it is 2.1 mm. At a focal depth of 5 mm the FWHM of the beam is 4.7 mm with all the rows on, with 10 on it is 1.4 mm. If we further reduce the aperture to 8 elements, the FWHM is reduced to 1.3 mm, though the output pressure is reduced by ~9%. These results demonstrate that

reducing the aperture size when close to the transducer not only improves the beam profile by making it narrower and single lobed, but it also increases the peak pressure at the natural focus.

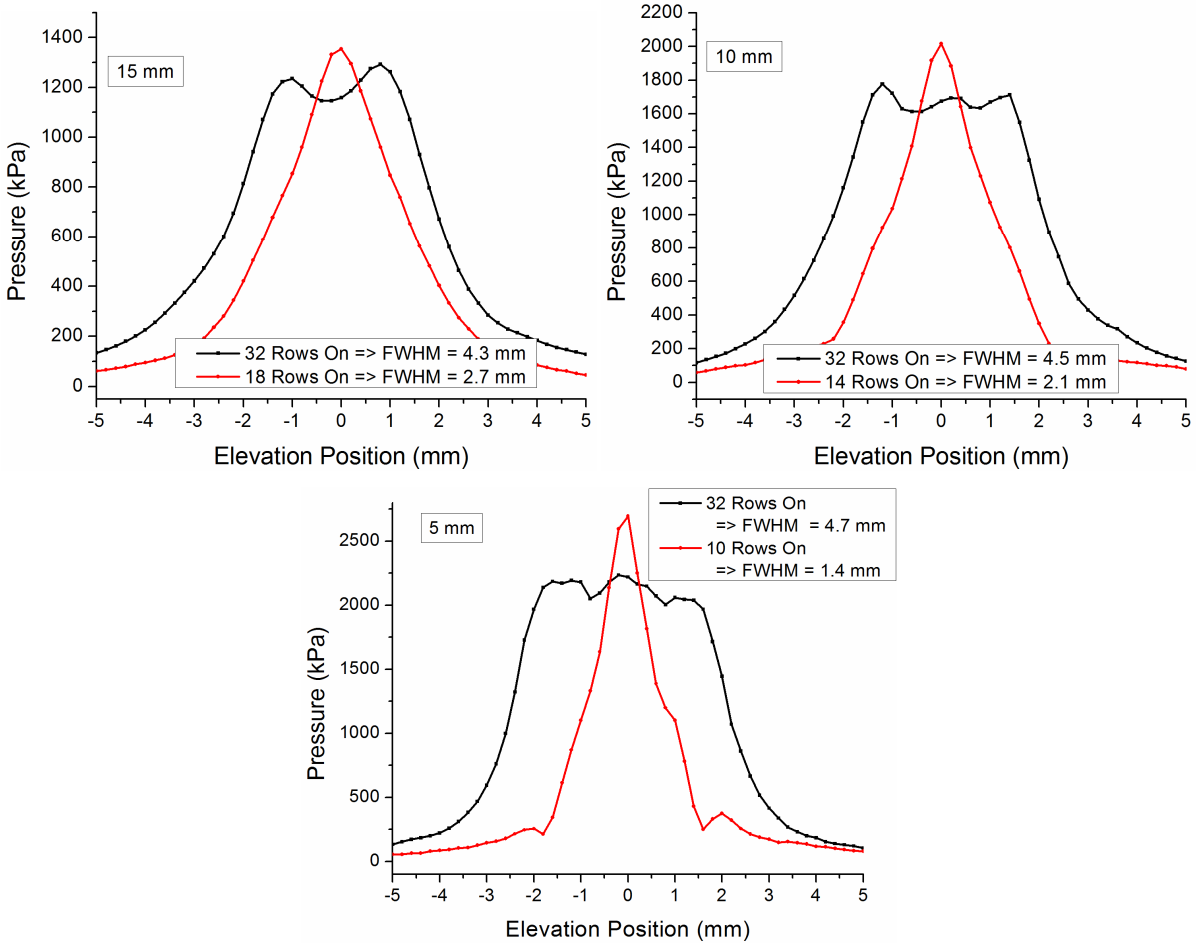

Figure 6.23: Vertical profiles of the focal line of a 32x32 element low-frequency row-column CMUT at depths of 15, 10, and 5 mm from the transducer with different numbers of rows 'on'.

In these experiments the transmitting aperture is centered on the middle of the transducer. This is because the beamformer is hard wired to maintain symmetry about the centre of the transducer. This has the potential to be a limiting factor in imaging applications, if the object of interest in near the transducer but not centered on it in the *y*-axis it may be invisible because the height of the beam is relatively small and the object may not be insonified. A way around this would be to enable any combination of rows to be turned on, effectively imitating the parallel scan of a linear array. In this case the subset of rows that are enabled would begin at the bottom and then advance upwards in a step by step manner allowing the imaging in front of the entire face of the transducer.

6.7.3 Beamprofiles in the Azimuth

In this section the width of the focal line will be discussed. The obtainable focal spot size is a function of the transducer aperture size, the wavelength of operation and the focal length, and can be approximated by

$$LineWidth = 1.206\frac{\lambda F}{L_x} \tag{6.3}$$

where *LineWidth* is the full-width-at-half-maximum of the beam width, λ is the wavelength of sound, F is the focal length, and L_x is the aperture size in the azimuth. For the 32x32 element transducer the aperture is 4.8 mm. The focal line width is measured in the same manner as the focal line height discussed in the previous section. In this case the hydrophone is scanned laterally through the focus of the beam. The hydrophone is placed directly in front of the transducer such that the scan angle is 0°. The bias voltage is -60V and the pulse amplitude is 30V. The height of the aperture is chosen based on the maximum pressure values obtained in the previous section. That is at 20 mm 24 rows are 'on', at 15 mm 18 rows are 'on', at 10 mm 14 rows are 'on' and at 5 mm 10 rows are 'on'. Plots of the line widths are given in Figure 6.24. As expected, the beam waist gets narrower as the focus is moved closer to the transducer from 1.1 mm at 20 mm to ~300 μm at 5 mm away. At 300 μm the beam width is close to the wavelength of operation which is typically given as the resolution limit of imaging systems. Clearly as the line width gets smaller the imaging resolution improves. This gives another impetus to be able to image close to the transducer.

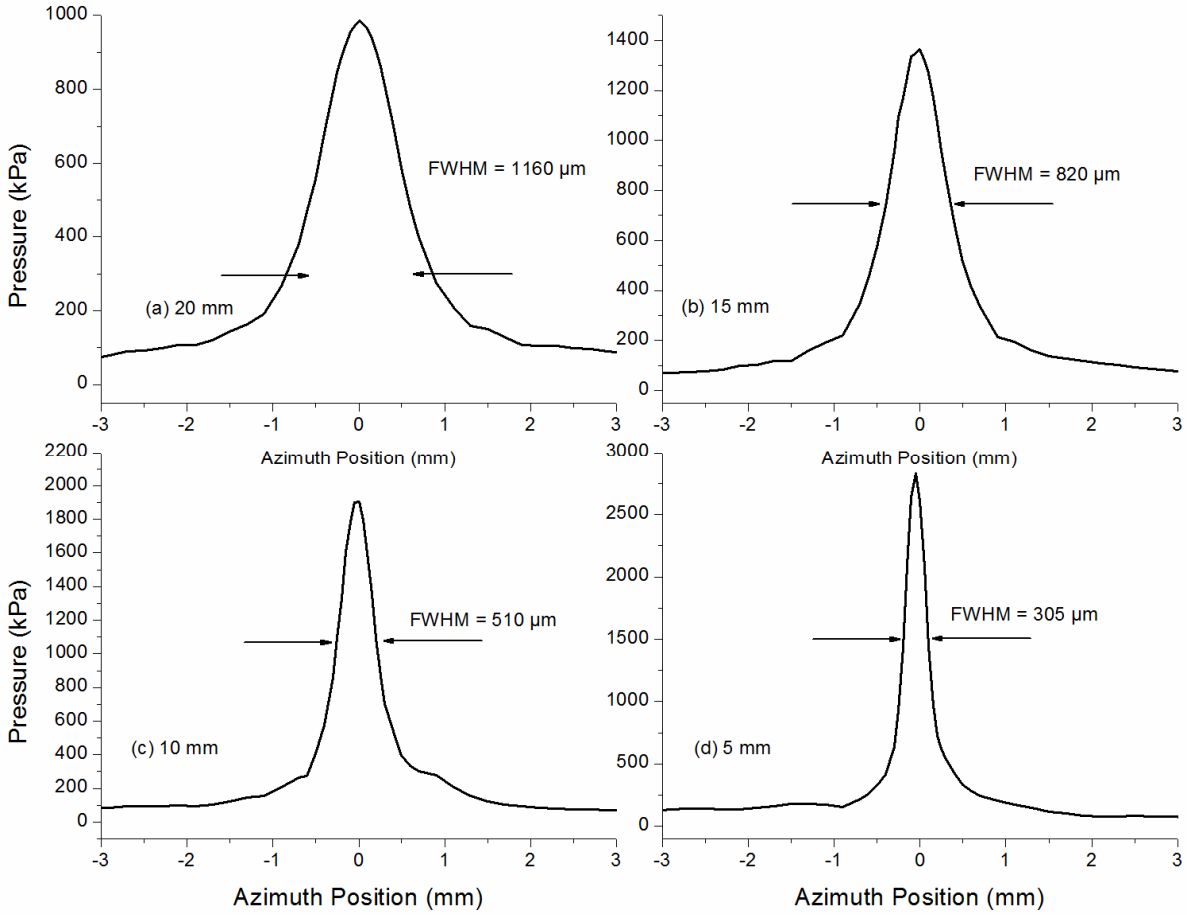

Figure 6.24: Plots of the lateral (azimuth) beam profile at distances of (a) 20 mm, (b) 15 mm, (c) 10 mm, and (d) 5 mm from the transducer. The transducer is focused directly in front of the transducer such that the scan angle is 0°. For (a) 24 of the rows are connected to the DC bias, for (b) 18 rows are connected, for (c) 14 rows are connected and for (d) 10 rows are connected.

6.7.4 Two-Dimensional Beam Profiles

For completeness, the two-dimensional beam profile of the transducer was measured with the system set to focus 10 mm away, once with all of the rows active and the other where 14 are active. The system setup is the same as is used for the elevation and azimuth measurements except this time the hydrophone is raster scanned through the entire field, and not just lines through the maximum. The bias is set to -60V and the voltage pulse is 30V. A plot of the two beam profiles is given in Figure 6.25.

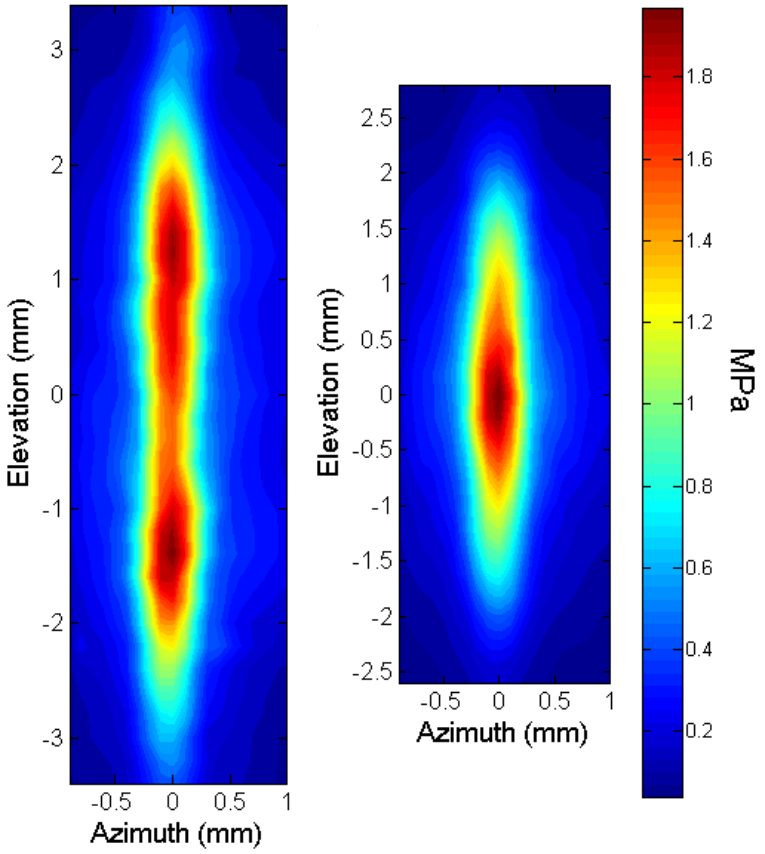

Figure 6.25: Beam profiles of the 32x32 element low-frequency array focused 10 mm onto the hydrophone 10 mm away. The profile on the left is with all 32 rows 'on', on the right 14 rows are 'on'.

6.8 Imaging Results

In this section initial proof-of-concept images are generated with the low-frequency 32x32 element row-column electrode transducer. Two targets are imaged with the transducer, the first is a wire target similar to the one used with the one-dimensional array. In this case two images are taken, one with a single vertical wire and one with a single horizontal wire. This helps establish the point spread function of the transmit and receive beams. The wires have a diameter of 225 μm and are made of steel. The second target is a set of 4 pins mounted perpendicularly to the front of the transducer such that heads of the pins are imaged. This is done to demonstrate the three-dimensional imaging ability of the row-column imaging scheme.

6.8.1 Imaging Method

Multiple sets of images are taken. When imaging the vertical wire, the entire height of the aperture is used. For the horizontal wire, one image is taken with the full aperture of the transducer enabled, and another is taken with 10 of the rows toggling. The voltage pulse is set to 30 V and the DC bias is -60 V. The transmit scan angle for the single wires is -10° to 10° and for the pin targets it is -20° to 20°. The beam is moved in 1° increments. The scan angles are kept small because of the lack of control of the receive aperture. The further off-axis the reflector is, the worse the performance of the receive beamforming. The array is set to focus at 15 mm, which is the midpoint of the depths of the four pins. The pins are set to have a range of distances from the front of the aperture, from approximately 12 mm to 17 mm. The heads of the pins have a diameter of ~1.8 mm. Data is recorded with a high speed oscilloscope sampling at 1.25×10^9 samples/s.

6.8.2 Image Processing Method

The image processing method for the row-column array is very similar to that used for the one-dimensional arrays. The angular response of the elements is compensated for using equation (5.3). If the transmit aperture is being dynamically adjusted the data is passed though a high-pass filter to eliminate some of the noise that the toggling causes on the signal. This electrical noise is somewhat of a concern as it can saturate the amplifier for about 10-15 μs after the voltage pulse. This effectively makes imaging closer than 10 mm not possible. For the time being this is not a significant concern as closer than 10 mm is too close to the transducer to obtain good image quality without a way to adjust the receive aperture.

Receive beamforming in elevation is then performed on each of the transmit data sets. This effectively divides the two-dimensional transmit slices into a series of three-dimensional lines that span the entire image volume. No apodization is performed. Envelope detection is performed as described in section 5.8.2 and the set of (r, θ, φ) data lines are converted into Cartesian coordinates using bilinear interpolation and put on a logarithmic scale. At this time, data above and below the centre plane of the transducer is projected onto the 0° plane to simplify display. The image processing software is custom written and currently lacks the sophistication necessary to fully manipulate the image data.

6.8.3 Wire Target Imaging Results

The processed B-scan image of the single vertical wire target with a fixed transmit aperture is shown below in Figure 6.26. The dynamic range of the image is 40 dB. The increased lateral spread of the wire compared to the two-dimensional image of Figure 5.28 is quite clear. Plots of the axial and radial cross sections of the wire are given in Figure 6.27. The measured -6 dB axial width is ~150 μm. The lateral -6 dB width is measured to be 46 mrad, which at a depth of 15 mm corresponds to ~690 μm.

The same experiment is carried out with a horizontal wire, located 15 mm away and 0° above the mid-plane of the transducer. In the first set the entire aperture is used for transmit. An elevation B-scan image of the wire is given in Figure 6.28. Plots of the axial and transverse (elevation) line widths are given in Figure 6.29. The axial -6dB width is 150 μm and the transverse -6dB width is 900 μm.

The experiment is repeated, but this time with the dynamic transmit enabled. For transmission, 22 rows are used. A B-scan image of the wire is given in Figure 6.30. Plots of the axial and transverse profiles are given in Figure 6.31. The axial -6 dB width is 150 μm and the transverse -6 dB width is 935 μm.

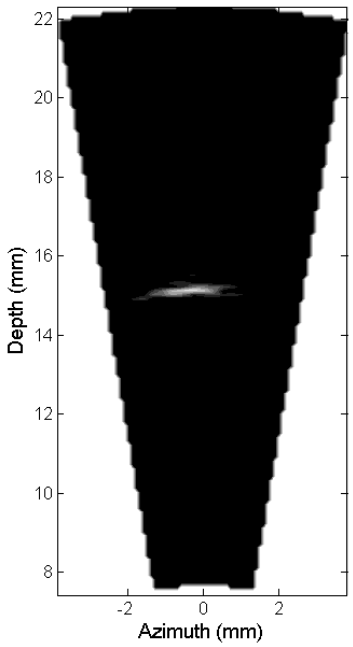

Figure 6.26: A 20° degree sector scan of a single vertical wire imaged with the low-frequency 32x32 element array. The dynamic range of the image is 40 dB. The transmit aperture is the full height of the transducer.

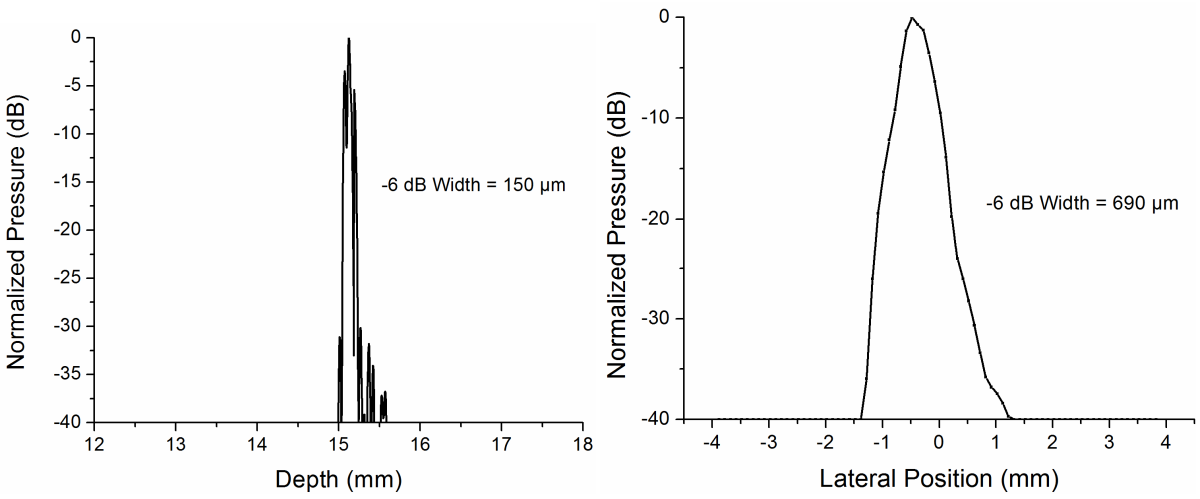

Figure 6.27: The left graph is a plot of the axial profile of a vertical 250 µm diameter wire. The -6dB width is ~150 µm. The graph on the right is the lateral profile of the wire. The -6dB width is ~ 690µm.

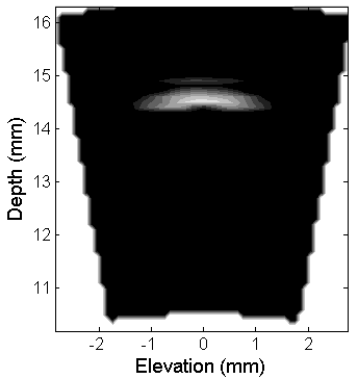

Figure 6.28: B-scan image of the horizontal wire. The dynamic range of the image is 40 dB. The full aperture of the transducer is used.

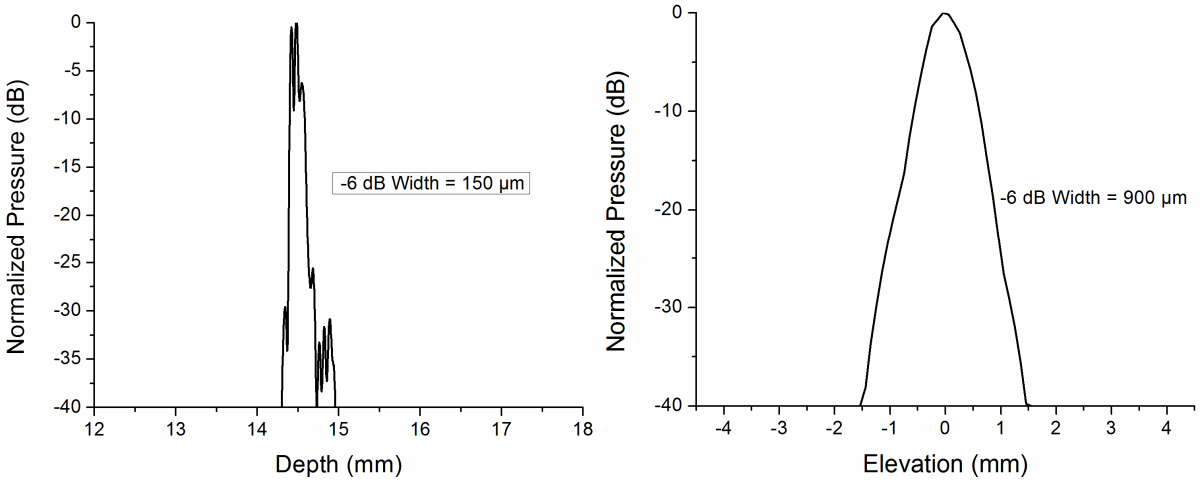

Figure 6.29: The left graph is a plot of the axial profile of a horizontal wire with the full aperture used for transmitting. The -6 dB width is 150 µm. The graph on the right is the profile in elevation of the wire. The -6 dB width is ~900 µm.

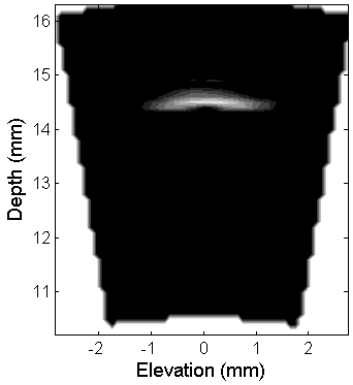

Figure 6.30: B-scan image of the horizontal wire with 10 of the rows toggling on and off. The dynamic range of the image is 40 dB.

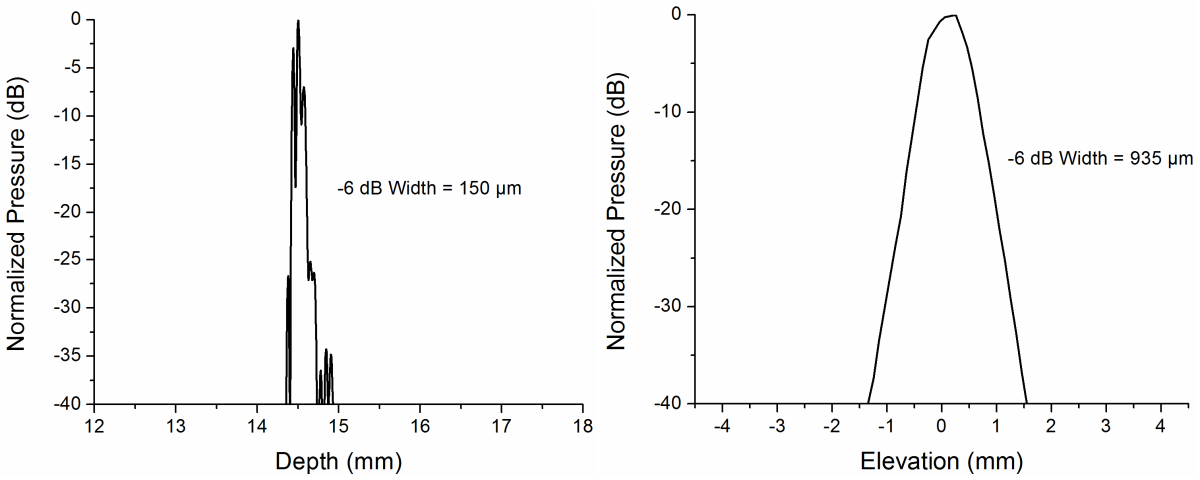

Figure 6.31: The left graph is a plot of the axial profile of a horizontal wire using the dynamic aperture for transmitting. The -6 dB width is 150 µm. The graph on the right is the profile in elevation of the wire. The -6 dB width is ~935 µm.

6.8.4 Three-Dimensional Image Results

As an initial demonstration of three-dimensional imaging a 4 pin-target is imaged. A schematic of the pin layout is shown in Figure 6.32

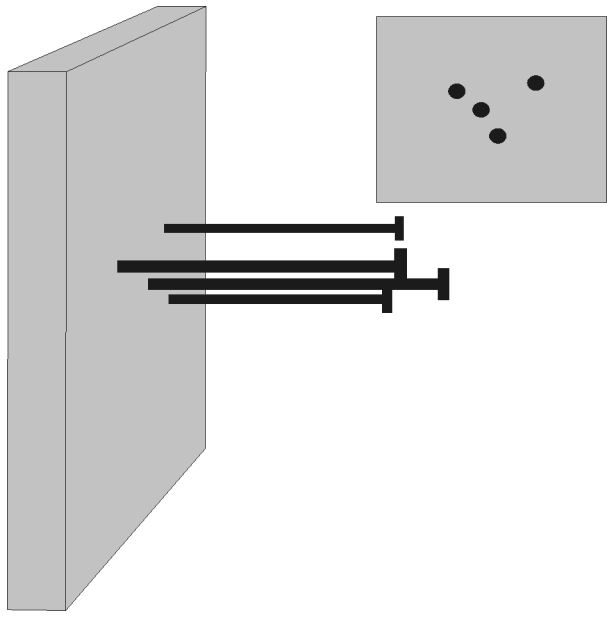

Figure 6.32: Schematic of the pin layout. The heads of the pins are placed at different *x-y* positions as well as at different depths.

Presented are a number of sector scans at four different receive angles with the dynamic aperture both disabled and enabled. In the four B-scan images presented in Figure 6.31, the receive beam is set to -6°, 0°, +5°, and +7°.

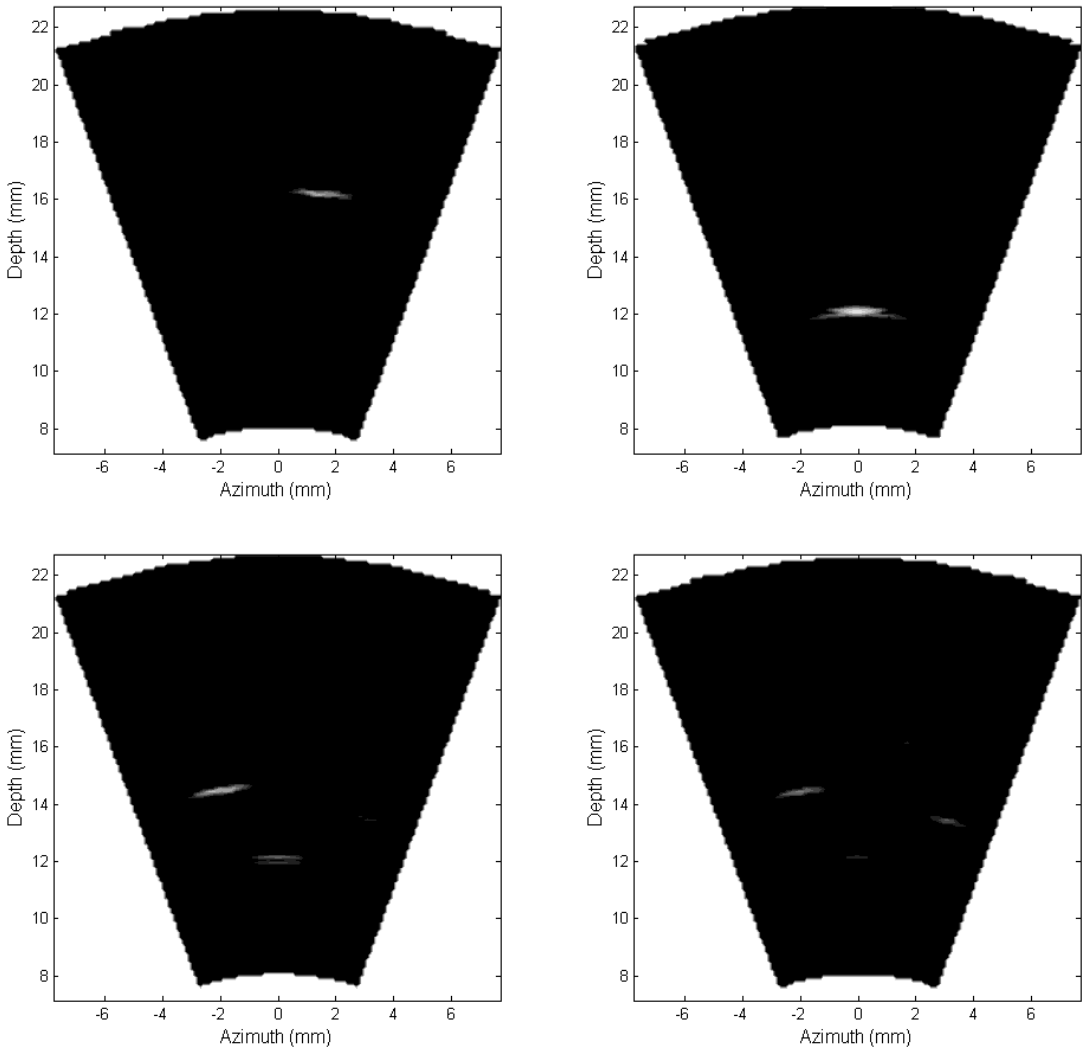

Figure 6.33: A set of B-scan images of the pin head target. The transmit beam scans from -20° to +20°. In the top left the receive beam is set to -6°, in the top right image the receive beam is set to 0°, in the bottom left the receive beam is +5° and in the bottom right image the beam is set to +7°.

The experiment is repeated with the dynamic aperture enabled. The receive beams are set to the same values as with the full aperture images, ie -6° (top left), 0° (top right), +5° (bottom left), and +7° (bottom right).

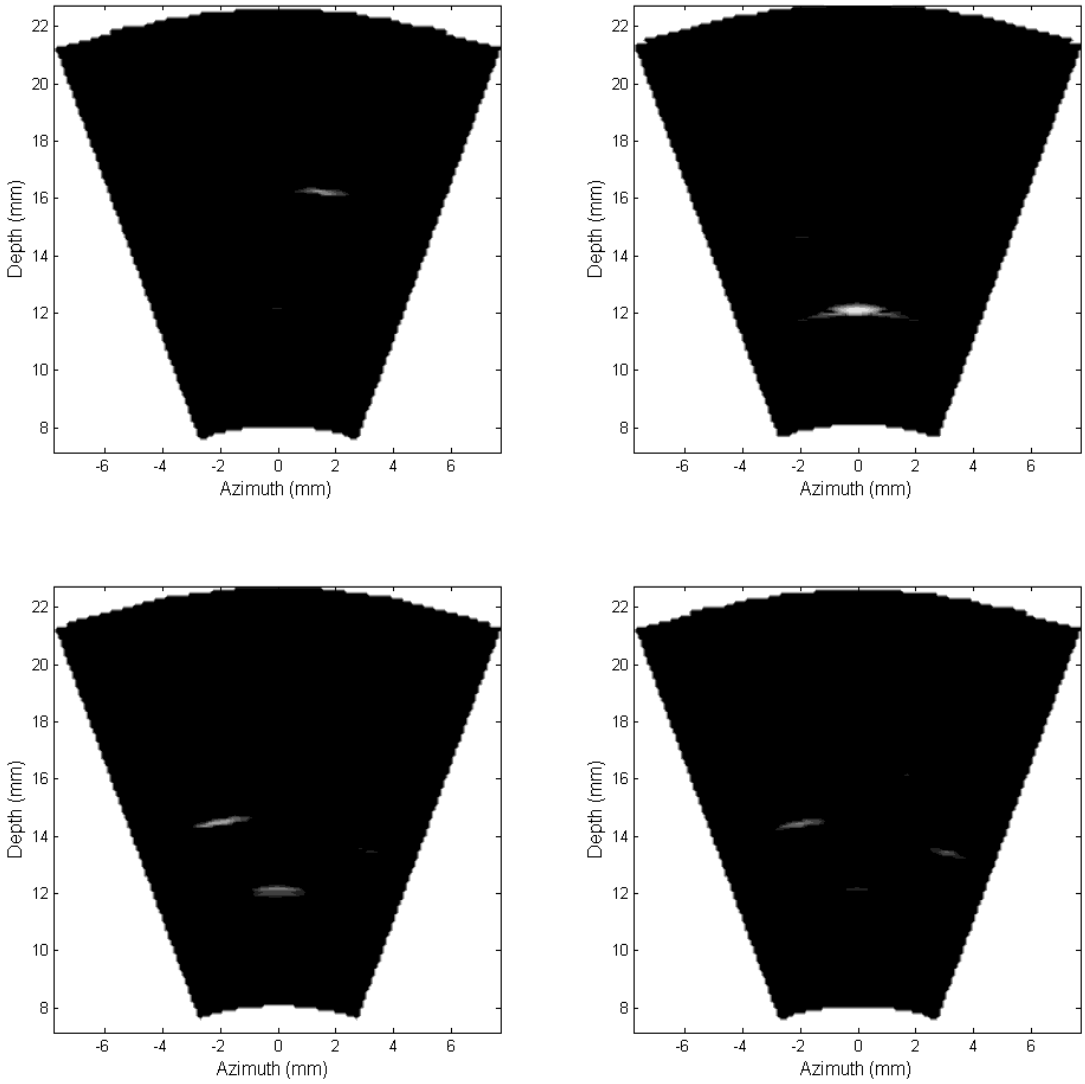

Figure 6.34: A set of B-scan images of the pin head target with the dynamic transmit aperture enabled. The transmit beam scans from -20° to +20°. In the top left the receive beam is set to -6°, in the top right image the receive beam is set to 0°, in the bottom image the beam is set to +5°, and in the bottom right it is set to +7°.

While this is an initial attempt at the three-dimensional imaging it is somewhat surprising that there is little noticeable benefit from adjusting the transmit aperture. Clearly more work needs to be done to explore the performance of this imaging method and improvements need to be made to the image processing software.

6.9 Discussion

In the work presented in this chapter the viability of using a crossed electrode CMUT array for three-dimensional imaging has been demonstrated. The bandwidths of the transducers are greater than 100%, relatively large pressures at the focal point in excess of 2 MPa has been shown, and three-dimensional imaging has been qualitatively demonstrated in proof-of-concept imaging.

The ability to generate volumetric images has important clinical value but getting the transducer, the electronics, and the necessary cabling into a space suitable for a catheter or an endoscope is very challenging. While a fully populated two-dimensional array has a much larger number of elements when compared to one-dimensional array, it is not the fabrication of the transducer itself that is the greatest challenge but getting the necessary information to and from the transducer. By significantly reducing the required electronics and the number of data channels while maintaining good image quality, volumetric imaging becomes accessible to a range of applications. Row-column addressing scheme can satisfy these goals.

In addition to demonstrating three-dimensional imaging using row-column addressing with CMUTs, the ability to dynamically adjust the height of the transducer by applying the necessary DC bias to only select rows has been shown to improve the transmit beam quality near the transducer. Extending this technique to include the dynamic adjustment of the receive aperture will allow the optimization of both the transmit and receive beams over a wide range of angles and distances from the transducer maximizing the field of view.

The technique of turning off the bias to select rows could also be advantageous in one-dimensional arrays. Typically, a fixed lens is used to focus in elevation but it, by necessity, has a fixed focal position. Being able to adjust the focal depth electronically in a relatively simple manner would extend the useful range of the lens. Implementing this for two-dimensional imaging would be more straightforward then it is for three-dimensional imaging as there would be no need to re-enable the rows after each transmitted pulse. Reducing the receive aperture height would in fact be beneficial when imaging near the transducer. The transducers used for three-dimensional imaging would be the exact same as those for the two-dimensional imaging described here. The only difference would be in the beamformer where the receive amplifiers would be connected to the columns and not to the rows.

One potential limitation of three-dimensional imaging with row-column addressing is that it is not easy to image the areas above and below the transducer. Because no active beamforming is done in the vertical dimension, significant acoustic energy does not extend above and below the transducer until the beam has propagated well into the far-field. As discussed earlier, the depth this occurs depends largely on the size of the aperture. One solution would be to transmit with only a few of the rows active at the top and the bottom of the transducer so that the length of the near-field is shortened. Another possible solution, though more complex to implement, would be to electronically swap the functionality of the rows and columns such that the rows are used to transmit and the columns are used to receive. Data obtained through both configurations could then be assembled into a single image. An extra set of switches would be needed to realize this type of functionality.

Chapter 7 Summary, Analysis, and Future Work

7.1 Summary

Ultrasound imaging is a very well established modality for obtaining information from the inside of opaque media, whether for medical or industrial purposes. Due to the much shorter wavelength, optical imaging techniques provide high imaging resolution but also suffer very short imaging depths in strongly scattering media such as biological tissue. Computed tomography (CT) scans achieve good resolution and depth; however, they expose the target to ionizing radiation. Magnetic resonance imaging (MRI) also provides excellent depth penetration and good resolution however the machines are very large and expensive limiting their availability to well-funded clinics and hospitals. Ultrasound, on the other hand, is low-cost, non-damaging, and has the potential to be ever more portable as signal processors become more powerful [129].

Virtually all commercially available ultrasound transducers use piezoelectric materials for the transducer. Capacitive micromachined ultrasonic transducers (CMUTs) are a relatively new technology that seeks to exploit the advances made in semiconductor processing technology to address some of the shortcomings of piezoelectric transducers, and to open up new imaging techniques. CMUTs typically have a larger bandwidth than piezoelectrics which improves depth resolution. They also have acoustic impedances that are much lower than those of piezoelectric transducers, thus making it easier to efficiently couple sound into media without the need for impedance matching layers. Perhaps most importantly, it is fairly straightforward to repeatedly and reliably fabricate small and densely populated arrays, which are necessary for electronic phased array imaging. Phased array imaging permits the generation of a multi-dimensional image from a stationary transducer and is considered superior to mechanically scanned imagers. In this thesis, CMUT transducers fabricated with a novel silicon nitride based fusion bonding fabrication process are investigated for their manufacturability, uniformity, electrical and acoustic performance, and suitability for two- and three-dimensional imaging.

Three generations of devices are investigated in this thesis, each with their own purposes. The first generation of devices establishes the fundamentals of the fabrication process while demonstrating promising functionality. Beyond the acoustic performance, the dielectric charging properties are studied.

The second generation devices simplify the fabrication process and consist of many array layouts that are suitable for imaging purposes. A 64-element linear array is investigated thoroughly for its uniformity, and its electrical and acoustic behaviour. Phased array beamforming and two-dimensional imaging is demonstrated.

The third generation devices are two-dimensional arrays designed to permit three-dimensional imaging. Because conventional phased array imaging with a two-dimensional array dramatically increases complexity, a row-column addressing scheme is employed which is only marginally more complex to operate than a one-dimensional array. To improve image quality near the transducer a novel driving technique is used that dynamically enables and disables portions of the transducer to enhance the near-field imaging possibilities of a row-column transducer. The electrical, acoustic, and beamforming performance is investigated. Three-dimensional imaging is demonstrated.

A summary of the measurement results follows.

7.1.1 First Generation Device Results

The fundamentals of the silicon-nitride based fusion bonding fabrication process are discussed in some detail. The fabrication process is straightforward, needing only three masks and can be completed by an individual in the cleanroom in less than a week. The yield is reasonably good for a first generation process. The mechanical durability is also found to be excellent.

Electrical characterization is performed that confirms the resonant frequency of the device is ~15 MHz, which agrees well with the equivalent circuit model presented in Chapter 3. Pitch-catch and pulse-echo measurements are performed to establish that the bandwidth of the transmitted pulse is in excess of 100% as is expected of CMUTs. The pulse-echo experiments also demonstrate that the transducers are sensitive enough for future imaging purposes.

The dielectric charging performance of the transducers is also investigated. This is of interest because this generation of devices does not exhibit the phenomena of dielectric charging that is typical of electrostatically actuated MEMS devices. The device was operated for more than 120 consecutive hours and brought into collapse mode with no significant change in the measured capacitance. This is significant because dielectric charging changes the operating point of the transducer and can require re-calibration or discharging to maintain the same operating performance.

The lack of dielectric charging is believed to be a result of the use of low-stress silicon nitride as the insulation layer. A drawback identified with this material is its very low dielectric breakdown voltage. This means that if the membrane does not remain bonded from the time it is released until the metallization is done then the dielectric layer will fail when a bias is applied shorting out the entire element. This has a significant impact on the yield of large transducers.

7.1.2 One-Dimensional Arrays Results

Transducers suitable for phased array imaging were presented. The fabrication process is somewhat simplified from that of the first generation of devices. The incorporation of a stoichiometric layer of silicon nitride underneath the low-stress nitride largely eliminates the problem of dielectric breakdown; however dielectric charging is now evident. Many types of layouts have been fabricated, including linear 1D arrays, 1.5D arrays, and ring arrays. The devices have one of two resonant frequencies, ~15 MHz or ~37 MHz. Some initial experiments have been conducted that demonstrate the functionality of the high frequency devices. These were carried out on a 64-element linear array. More extensive experiments were not carried out primarily due to time considerations but also because the elevated operating frequency makes the electronics necessary for beamforming somewhat more challenging. The experiments that have been carried out again demonstrate a large bandwidth in excess of 100% and good sensitivity.

More extensive experiments conducted with a 64-element low-frequency device were presented. Electrical experiments with a vector network analyzer were performed to demonstrate the resonant frequency of the device. Pitch-catch and pulse-echo experiments in immersion were carried out to confirm the expected large bandwidth of the device, determine the frequency of operation in immersion, and to demonstrate the good receive sensitivity.

The uniformity of the resonant frequency across a single transducer, multiple devices from the same wafer, and from wafer to wafer was measured using a vibrometer and a vector network analyzer. The resonant frequency across all 64 elements was found to be 14.4 MHz with a standard deviation of 89 kHz, or 0.6%. Testing 12 devices from a single wafer yielded an average value of 14.4 MHz with a standard deviation of 340 kHz, or 2.3%. Testing two devices from 9 different wafers yielded an average resonant frequency of 14.9 MHz with a standard deviation of 460 kHz, or 3.1%.

Aside from measuring the uniformity of the resonant frequency in air, the uniformity in immersion was also determined. In this case the peak-to-peak pressures of 32 elements from a single 64-element transducer were measured. The hydrophone was placed 30 mm away and the mean pressure measured was 51.1 kPa with a standard deviation of 1.7 kPa, or a relative value of 3.3%. The receive uniformity was also determined by measuring the receive signal on each element from a piezoelectric transducer placed 14 cm away. The mean peak-to-peak received signal was 870 mV with a standard deviation of 36 mV, or 4.1%.

A custom built beamformer consisting of a field programmable gate array (FPGA) and off-the-shelf integrated circuits was designed and built to test the CMUTs as phased array imagers. The voltage pulser is capable of generating pulses with amplitudes greater than 30V with a full-width-at-half-maximum (FWHM) of 40 ns. The beamformer is capable of driving 32 of the 64 elements.

The beam profile of the focused acoustic beam was measured using a hydrophone. Focusing directly in front of the transducer 17.5 mm away from the transducer yielded a focal line with a FWHM of ~1 mm and a maximum peak-to-peak pressure in excess of 2.1 MPa without correction for diffraction or attenuation.

Finally, a two-dimensional image of a 4-wire target was made using the beamformer and custom image processing software written in MATLAB. The steel wires have a diameter of 225 μm and were located between 15 and 27 mm away from the transducer. The -6 dB axial width of the nearest wire was measured to be 130 μm. The lateral width of the wire was measured to be 500 μm, or 30 mrad. The signal to noise ratio is greater than 100 dB.

7.1.3 Two-Dimensional Array Results

The final set of devices was fabricated to demonstrate three-dimensional imaging using a transducer that is easier to fabricate, and drive than a fully populated two-dimensional array. These devices use a crossed electrode scheme which amounts to having two one-dimensional arrays orthogonal to one another in a single transducer. Transmit beamforming is performed in the azimuth and receive beamforming is performed in elevation. Many sizes of arrays are fabricated with resonance frequencies at one of two values, ~15 MHz, or ~28 MHz. Array sizes range from 128x128 to 16x16. As with the one-dimensional arrays, a few initial experiments were performed with a medium frequency device but the majority were performed with a 32x32 element low-frequency array.

Tests with the medium frequency device established the resonant frequency as ~28 MHz, and the frequency of operation in immersion as ~12.5 MHz with reasonably good bandwidth.

Immersion experiments with the low-frequency device demonstrated the frequency of operation as approximately 5.8 MHz with a bandwidth in excess of 100%. Uniformity tests were carried out across a single transducer using a vibrometer with the average resonant frequency found to be 15.2 MHz with a standard deviation of 38 kHz, or 0.25%. The immersion transmit and receive uniformity were also measured across the array. Measuring the output pressure of each of the 32 elements yields an average peak-to-peak pressure of 38.3 kPa with a standard deviation of 1.3 kPa or a relative value of 3.4%. Receive uniformity was measured to have a standard deviation of 7.4%.

A beamformer suitable for driving a row-column electrode transducer was designed and built. The design is similar in many ways to the beamformer used for the one-dimensional arrays as both the pulser and amplifier circuitry is the same. The primary difference between the row-column beamformer and one-dimensional beamformer is the ability to dynamically adjust the effective height of the array by turning off the bias to selected rows. This permits a certain level of control in the beam height which in turn improves imaging performance near the transducer. A number of experiments were performed to characterize this improvement. With the beamformer set to focus 20 mm in front of the transducer the focal beam height is improved from 4.5 mm with two lobes to 3.2 mm with a single lobe. When focused at 5 mm the minimum beam height is reduced from 4.7 mm to 1.4 mm. In addition to narrowing the beam profile the peak pressure is also increased.

The lateral beam profile is also measured at a variety of different focal depths, ranging from ~1.2 mm at 15 mm to 300 μm at 5 mm. Peak pressures of ~2.8 MPa are observed when the focal point is set to 5 mm

The point spread function of the row-column array is determined by imaging a horizontal and a vertical wire target. Measuring the vertical wire, the axial width was found to be 150 μm and the lateral width was found to be 54 mrad. Measuring the horizontal wire with a fixed aperture, the axial width was found to be 150 μm, and the transverse width 60 mrad. With the dynamic aperture, the axial width was found to be 150 μm, and the transverse width a 62 mrad.

An initial demonstration of three-dimensional imaging was also carried out with the low-frequency 32x32 element array. More work needs to be done with the image processing to truly gauge the performance of this technique, however initial results do appear promising. A target consisting of

4 pin heads mounted perpendicularly to the transducer was imaged. Resolving the 4 pins was achieved with approximately the correct spatial position. Using the dynamic transmit aperture yielded a marginal change in the elevation performance. Imaging of extended diffuse reflectors is necessary to better gauge the performance of dynamic aperturing. To achieve better quality imaging near the transducer the electrical performance of the switching circuitry needs to be improved and a method for dynamically adjusting the receive aperture needs to be implemented as well.

7.2 Analysis

Here the results obtained with the one- and two-dimensional arrays will be given in the context of their suitability for endoscope or catheter based phased array imagers. In particular, the two main contributions of this dissertation, the novel fabrication process, and the use of a row-column addressing scheme with CMUTs will be looked at in terms of their advantages, disadvantages, and prospective.

7.2.1 Advantages of Si_xN_y Based Fusion Bonding Fabrication

7.2.1.1 Avoiding SOI Wafers

As discussed in section 2.5.2, the fusion bonding method of CMUT fabrication has a number of distinct advantages when compared to surface micromachining. Specifically, they are easier to fabricate, have better fill factor, and have improved uniformity. The fusion bonding process first developed by Huang *et al* uses silicon-on-insulator (SOI) wafers to enable the transfer of a membrane onto a wafer containing the etched cell cavities. SOI wafers in general are relatively easy to acquire from silicon wafer suppliers, though their cost is typically more than 10 times that of standard wafers and can be difficult to acquire in a timely manner with the desired device layer thickness and conductivity. This is especially true in research where relatively infrequent and small quantities form the basis of typical orders. Even getting a quote from a supplier can prove challenging for single boat size orders. Employing a user deposited membrane largely eliminates this problem with only a marginal increase in fabrication time and cost, and a minor penalty in thickness uniformity.

7.2.1.2 Insulating Membrane

Along with avoiding the difficulties associated with SOI wafers there are benefits to having an insulating membrane as opposed to a semiconducting one. It has been shown that there is an ideal layout of the top electrode that minimizes the parasitic capacitance and maximizes the transduction efficiency [130]. Transduction efficiency improves when the DC displacement of the membrane is maximized. Increasing the electrode coverage of the membrane increases the capacitance of the cell and thus results in a greater displacement for the same bias voltage. However, increasing the electrode coverage beyond 50% yields diminishing returns as the increase in transduction efficiency becomes minimal. This is primarily because the edges of the membrane are fixed and the outer edge of the membrane cannot deflect to as great an extent as the center of the membrane. The extra capacitance however does reduce the bandwidth of the transducer due to an increase in the time constant of the electrical component of the circuit.

A semiconducting membrane behaves somewhere between a conducting and insulating membrane. One can imagine a simple model of this situation with a resistor in parallel with a capacitor. At low frequencies, the reactance of the silicon is larger than the resistance and the membrane behaves as a conductor. At a high frequency the opposite occurs; the reactance diminishes and the membrane behaves as an insulator [65]. What is considered a high and low frequency depends on the dimensions of the membrane as well as its conductivity. This in and of itself can cause some design problems because the operation of the cell will be quite sensitive to the conductivity of the membrane. When the membrane behaves as a conductor one can no longer optimize the electrode coverage to achieve good efficiency and low parasitic capacitance. If the entire membrane behaves as a conductor then the whole device would be a capacitor, and patterning the top electrode will have little effect.

An insulating membrane does not suffer these issues and its electrical behaviour is well understood and is consistent with frequency. The dielectric constant of silicon nitride ensures that the capacitance of the gap will still be the dominant capacitance of the cell.

7.2.1.3 Potential for Reduction of Charge Buildup in the Insulating Layer

Dielectric charging is a primary concern with the commercialization of electrostatically actuated MEMS devices, CMUTs included. The buildup of charges in the dielectric layer shifts the operating

parameters of the device leading to a performance over time. The effect can be reversed by switching the polarity occasionally but this is not an ideal solution.

Experiments performed with the first generation devices showed that they exhibited only very minor dielectric charging effects. While subsequent generations did not exhibit the same behaviour, it is believed this is due to a change from using purely low-stress silicon nitride to using a combination of the low-stress nitride and stoichiometric nitride. Observing a lack of dielectric charging is very interesting and is worthwhile pursuing to determine if a good balance can be found between dielectric strength and a charging behaviour.

7.2.1.4 Patterning of Bottom Electrodes

The implementation of two-dimensional CMUT arrays is dependent on being able to isolate both the top and bottom electrode of individual elements. This is true whether the device is a fully addressed 2D array or if a row-column addressing scheme is being used. While this is not directly related to silicon nitride being used as the membrane and insulation membrane, it is related to CMP and fusion bonding being used to facilitate some fabrication flexibility on the bottom wafer beyond highly doped wafers and thermally grown silicon dioxide to yield functional CMUTs. The majority of two-dimensional arrays to date have been fabricated using the surface micromaching process because it is relatively easy to pattern both the top and bottom electrode arrays. Fully populated 2D arrays have been shown using a fusion bonding process but it involves significant patterning of the back side wafer to isolate the blocks of the silicon substrate from one another [37]. The process reported here allows the direct patterning of the bottom electrodes using straightforward photolithography steps. There is no reason the same techniques could not be used for dense 2D arrays as well.

7.2.2 Potential Drawbacks of Si_xN_y Based Fusion Bonding Fabrication

The primary drawback associated with this fabrication process stems from the fact the silicon nitride is user deposited. When depositing silicon nitride in a low-pressure chemical vapour deposition tube (LPCVD) the deposition rate is not uniform across a single wafer or from wafer to wafer in the tube. The reactants tend to deposit on the first surface they come across meaning the edges of the wafers and the wafers closest to the gas source tend to accumulate more material on them. Wafers with a nominal thickness of 500 nm of material on them can have values 10 – 20 nm above or below that. With 20 wafers in the furnace the difference between the thickest measured value and the thinnest

value can range up to 100 nm. By adjusting the polishing time the wafer to wafer uniformity can be improved to around ±20 nm. This lack of consistency in membrane thickness impacts the uniformity of the devices. This explains the results seen in Section 5.6 which show that uniformity across a single transducer is very good, with a relative standard deviation of less than 1%, while across a whole wafer and wafer to wafer it increases to several percent.

Aside from the LPCVD uniformity issues, the other potential concern is the smoothness of the surfaces. Fusion bonding is very sensitive to the smoothness of the surface. An RMS roughness of 5Å has been stated as a threshold roughness to getting good quality fusion bonding. The surfaces of the wafers after LPCVD deposition are rougher than this (in the case of annealed polysilicon it can be more than 2 orders of magnitude rougher) and this is why chemical mechanical polishing (CMP) is necessary. While CMP is an established microfabrication tool, it is not as well behaved as other tools. Along with concerns with the uniformity of the polishing rate across the surface of the wafer and from wafer to wafer there are issues with the slurry used in the process. If the wafers are not handled properly (discussed in Section 5.4) there is a strong chance that slurry particles will be stuck to the surface, which strongly impacts the fusion bonding success rate. Avoiding the CMP process entirely would be ideal. Using SOI wafers to supply the membrane and thermally grown silicon dioxide for the insulation layer means that no polishing is necessary if one pursues the 'traditional' fusion bonding process. That being said, reasonable yields were achieved using a non-optimized polishing procedure.

7.2.3 Prospective of Si_xN_y Based Fusion Bonding Fabrication

The fabrication process based on using silicon nitride for both the membrane and insulation layers and bonding them together has been shown in this work to be a viable method to fabricate CMUT devices for imaging applications. While it is too bold to suggest that this method is the 'best', or that CMUT fabrication should move toward this technique, the advantages of using user-deposited silicon nitride are real and many of the current drawbacks can be addressed through further research.

The fabrication process itself is straightforward, requiring only three masks. The most challenging steps to perform are the chemical mechanical polishing, the wafer bonding and the release. The rest of the process steps are straightforward material deposition and removal with features that are neither particularly deep nor small. All three of the challenging steps have room for optimization that will further improve the fabrication yield.

The chemical mechanical polishing (CMP) tool at the Cornell Nanofabrication Facility (CNF) has a number of settings which are user adjustable, including the type of slurry, the type of polishing pad, slurry flow rate, pad rotation speed, wafer rotation speed, downward pressure, and wafer holding vacuum pressure. All of these have varying degrees of impact on the polishing rate, smoothness and uniformity. While establishing a fabrication procedure for the CMUTs, some time was spent with the CMP tool to find suitable parameters. Because time and money were at a premium, once a set of parameters was found that yielded a reasonably successful outcome, little more was done to optimize the step. There is clearly more work that can be done to further optimize smoothness and uniformity. Beyond tweaking some of the parameters, a more repeatable process to get the polished wafers from the CMP tool to the slurry cleaning bath would invariably improve the yield as well. It is thought that this is the process that most critically impacts the success rate of the fusion bonding as it depends on the quickness and dexterity of the user.

Success with fusion bonding is critically dependent on the smoothness of the wafers which is why the CMP step is so important. After CMP, the cell cavities are etched into the bottom wafers and then a cleaning and activation process is performed immediately before bonding occurs. The cleaning and activation process was arrived upon after discussion with another CNF user who was doing fusion bonding with silicon dioxide based materials. Again, once successful bonding was demonstrated there was no further investigation of the pre-bonding process. There are likely improvements to the cleaning/activation steps which would make the two silicon nitride surface more amenable to bonding.

After bonding, the top handle wafer is removed to release the membrane. This was accomplished using a heated KOH bath to effectively dissolve the entire top wafer. The bottom wafer is protected by silicon nitride that is deposited on all surfaces by LPCVD. Silicon nitride is a very effective barrier to KOH; the silicon to silicon nitride selectivity is estimated to be 1,000,000:1 [131]. However, if there are any defects in the nitride layer the etchant can get to the bottom wafer and significantly etch into it. On several occasions wafers were ruined because of this process. Due to the incredibly high selectivity of the KOH to silicon versus silicon nitride, it is an excellent tool to release the membrane. However, a better method to remove most of the 500 μm thick handle wafer would be a mechanical grinder. Unfortunately a grinder was not available for use at CNF. Mechanically removing the first 450 μm of silicon in this manner, and the final 50 μm with the KOH would shorten the release time (greater than 5 hours in the heated KOH bath) and improve the yield because there would be

insufficient time in the KOH to significantly damage the bottom wafer if there are any defects in the silicon nitride protection layer.

In conclusion, the novel fabrication process presented in this thesis is able to produce CMUTs with a reasonably good yield with little optimization done to the process as a whole. The process as it stands now is straightforward and flexible with a clear route to address its shortcomings.

7.2.4 Advantages of Row-Column 3D Beamformer

There are two primary advantages to using a row-column electrode scheme to generate three-dimensional images. The first is they are simpler to fabricate and operate than fully populated 2D arrays, the second is that image acquisition time is no longer than that of a one-dimensional array.

7.2.4.1 Simple Fabrication and Operation

Adding the ability to perform three-dimensional imaging adds only two extra deposition steps and one photolithography step to the process designed for one-dimensional arrays. Equally important is the fact that the number of connections to the array only increases by a factor of two and not to the power of two. This makes implementation substantially easier.

If and when these devices are integrated into a catheter or endoscope some three-dimensional integration with electronics will likely be necessary due to space constraints. Flip-chip bonding is a likely candidate to implement such functionality. One change to the current CMUT layout necessary to accommodate this is to route the electrical signals of both the top and bottom electrodes to the bottom of the wafer to connect to the electronics. This is typically done using deep reactive ion etching (DRIE) to tunnel through the substrate and connect the top of the wafer to the bottom of the wafer. Needing fewer of these vias can have a significant impact on ease of fabrication, especially as the acoustic frequency of the device is increased to realize higher resolution imaging. Readily available aspect ratios with DRIE are typically in the range of 20:1. If one is working with a 500 μm thick wafer, the via would be ~25 μm in diameter. Consider that at moderately high frequencies such as 25 MHz the element pitch needs to be ~30 μm, or at 40 MHz it needs to be ~20 μm to satisfy the Nyquist sampling criteria and avoid grating lobes. Keeping the via size smaller than the element size becomes challenging, especially because each element needs its own through via. A row-column addressing scheme on the other hand needs only one connection for each row and column electrode, greatly reducing the number of through vias and the accompanying space constraints.

A related issue, is that a catheter or endoscope based imager is likely to require an application specific integrated circuit (ASIC) to handle the voltage pulse generation, pre-amplification and multiplexing for the transducer. Because each element needs its own pulser and amplifier, each copy of the pulser and amplifier would need to fit into an area the size of each element. Again as the frequency of operation increases and the element size shrinks this gets to be more challenging. A 32x32 element array using a row-column scheme requires only 32 pulsers and 32 pre-amplifiers, whereas a fully populated 2D array would require 1024 pulsers and 1024 pre amplifiers and a multiplexer/buffer able to feed all of that data down a limited number of channels. Clearly the ASIC becomes easier to design and operate with the substantially lower requirements afforded the row-column electrode scheme.

7.2.4.2 High Frame Rate

The other advantage a row-column addressing scheme affords is that the image acquisition time does not increase compared to a 1D array. Consider a linear phased array that scans from -45º to +45º and focuses at two different depths; to obtain reasonable image quality 182 transmit events are required. If the speed of sound is 1500 m/s and the deepest we wish to image is 20 mm it takes ~27 μs for each pulse echo event and 4.9 ms to generate a single frame which corresponds to a frame rate of ~200 frames/s. The same number of transmit pulses are required with row-column imaging since the transducer is driven like a 1D array in transmit. It is assumed that the travel time of the sound pulses is the limiting factor in getting a high frame rate, and that the digital signal processors are able to perform the receive beamforming in real time and render images at this rate.

Using classic phased array imaging with a fully populated 2D array, the focal region is a spot (not a line) and a full 3D raster scan is necessary to generate the whole image. Again, if we assume -45º to +45º scans in both directions as well as focusing at two different depths, a total of over 16,500 transmit events are required. Again assuming a 20 mm maximum depth the time to generate a single frame is ~0.5 seconds or 2 frames/s. There are ways to increase the frame rate by, for example, sending out multiple transmit and receive beams simultaneously [132], [133]. But the fact remains that to obtain the best quality image a low frame rate will result.

7.2.5 Disadvantages of a Row-Column Beamformer

Unsurprisingly, the biggest drawback of using a row-column electrode scheme for three-dimensional imaging is the loss of image quality. Groups that have modeled the point spread function of the transmit and receive beam report that the spot size is roughly twice that of using classic phased array imaging [124]. Of course whether the loss of resolution is acceptable or not depends on the application being considered. It could very well be that for large ex-corporeal transducers all of the electronics necessary for a fully populated 2D array can manageably fit into the transducer handle. It seems likely though that some simplification of a catheter or endoscope based system will be necessary, not just to increase the frame rate but to simplify the driving electronics and connection requirements. Khuri-Yakub *et al*, have done some modeling on various other driving schemes that are possible with fully populated 2D array in an attempt to find a compromise between image resolution, acquisition time and signal to noise ratio [118]. The conclusion they arrive at is to use the two long diagonals of a square array to transmit (focusing in all three dimensions is still possible) and the rest of the elements for receive. That being said, Demore *et al* have shown that by increasing the aperture of the transducer and the transmit power, resolutions and signal-to-noise ratios comparable to one-dimensional arrays with a fixed lens and fully populated 2D array can be achieved [124].

7.2.6 Prospective of a Row-Column Beamformer

A cross-electrode transducer appears to be a very promising way to achieve three-dimensional imaging. It offers a good compromise on ease of fabrication, controllability, image quality, and frame rate.

Fabrication of these types of transducers requires only a few extra steps beyond that needed for a one-dimensional arrays, and this by itself is fairly compelling. Beyond ease of fabrication, CMUT technology makes reducing the size of the array elements to sizes suitable for high frequency imaging relatively trivial as photolithography can easily be used to pattern features below a micron. Beyond being able to shrink the element size, using CMUTs also makes it straightforward to optimize the acoustic beam for imaging in the near-field by controlling the effective aperture of the transmit and receive apertures. Using this technique on its own or in conjunction with a fixed lens will increase the range of depths the transducer can provide good quality images.

The simplified drive electronics for this control method makes a strong case for further development of this technology. The ASICs necessary for implementation should be simpler to design as both space requirements and complexity are eased.

Reduced resolution compared to a fully populated array may limit applications but there are a couple of things that can be done to lessen the impact. The first would be operate at higher frequencies. At higher frequencies, image resolution improves and element pitch decreases meaning more elements can fit into the same area. A benefit of row-column beamforming is that the entire transducer is being used to transmit, hence the maximum signal is being sent into the target. The entire transducer is also used to receive which improves sensitivity. With some of the reduced element driving schemes discussed by Khuri-Yakub *et al* in [118], only a relatively small percentage of the elements are being used to transmit and therefore the signal-to-noise ratio is likely to suffer. Another potential way to improve the image quality is to acquire two sets of data for each frame. One where the columns are used to transmit and the rows to receive and another one with them switched where the columns receive and the rows transmit. The two images could then be combined to improve the image quality and also to increase the field of view.

Finally, as mentioned earlier in this section, the potential frame rate is the same as is possible for two-dimensional images as the same number of transmit events are necessary. This would be important for imaging anything that is not essentially stationary, for example arteries that move and flex with each pump of the heart, or valves within the heart.

In conclusion, while not offering the best possible image quality, a row-column addressing scheme provides many advantages that have the potential to make a small, easy to fabricate, robust, high frequency, simple to control and high frame rate imaging transducer imminently achievable without any serious increase in complexity from what is required for two-dimensional imaging.

7.3 Future Work

There are a number of steps that need to be taken to realize a CMUT based ultrasound imager in our lab. Some have them been discussed in the previous section, such as improving the yield of the fabrication process by better characterizing it and exploring the effect of nitride composition on dielectric charging. Beyond that there are the challenging engineering hurdles necessary to package

the transducer and the necessary electronics into a volume small enough to fit inside an endoscope or catheter. Some of these challenges will be discussed in the following sub sections

7.3.1 Development of an ASIC

Probably the most important and challenging design hurdle needed to package a CMUT into a transducer is the need for an application specific integrated circuit. The ASIC will contain the necessary pulsers, pre-amplifiers and pre-processing circuitry necessary to get all of the information into and out of the transducer. The circuits used to generate the data presented in this thesis are composed of off-the-shelf components and hence are quite large. The circuit board on which everything is housed now has an area of 350 cm^2. A number of groups have achieved ASICs that can drive their CMUT transducers, but there are typically compromises made such as only having single elements at a time transmit [37]-[40].

The ASIC is usually based on a high-voltage CMOS process because the circuit operates at potentials from 20-30 V which are necessary to generate the voltage pulses [38]. On the same die, pre-amplifiers/buffers are included to convert the current generated by the CMUT into a voltage and to impedance match to the long cables leading back to the image processor. Because the capacitance of the transducers is so small (fF - pF regime) the impedance mismatch with the cables is too large to be able effectively get the small signal out without impedance matching first. Keeping the pre-amplifiers very close to the transducer reduces loss in the signal.

Another reason for signal processing is the need to reduce the number of cables going to and from the transducer. Clearly some multiplexing needs to be done to reduce the number of channels to a handful so that they can physically fit into the catheter or endoscope. Consideration also needs to be taken to get the necessary transmit beamforming delays into the transducer as well. The delay values change constantly as the focus of the transducer moves in angle and in depth. Individual connections from the outside circuitry to each of voltage pulsers would not be any more feasible in terms of space constraints that connecting each receive channel directly.

Fortunately, much work has been done in the field at both the research and commercial level. Also, organizations such as CMC Microsystems make the design and fabrication of these ASICs easier to achieve as the necessary CAD software and fabrication facilities are available to university clients at below-cost rates.

7.3.2 Encapsulation Method for the Transducer

To date all of the immersion experiments carried out have been in vegetable oil. Vegetable oil is chosen partly because it is cheap, readily available, and does a reasonable job of mimicking the acoustic properties of tissue. However, the primary reason it has been chosen is because it is an insulating fluid. This is necessary because the top electrodes and contact pads are exposed to the environment. Without an insulating fluid everything would short out. Vegetable oil is a suitable immersion liquid for initial tests, but before *in vivo*, or even *ex vivo* imaging can be done an insulating coating will need to be applied to the transducer. This is necessary not only to prevent the short circuiting of the transducer but also to protect the patient from being exposed to the voltage pulses and biases.

Beyond being insulating, any coating applied would need to be biocompatible and not excessively degrade the performance of the transducer. The material would have to be flexible, adhere to the silicon surface, and have an acoustic impedance between that of the transducer and the surrounding material. Some potential coating materials for CMUTs have been presented in the literature, with paralyene seeming to be a good choice [101].

7.3.3 Design Optimization

This thesis represents the start of the MEMS-based ultrasound project within out group. It is for this reason that although many different transducer types were fabricated during the course of this research they are essentially all first generation devices. The first set of devices established a fabrication protocol and demonstrated the generation and reception of ultrasound signals. The one-dimensional arrays were conceived as the most straightforward manner to demonstrate phased array imaging with the CMUTs fabricated using the new fabrication process. Finally, the row-column arrays are the result of wanting to demonstrate three-dimensional imaging using a fabrication method not substantially different than what has already been accomplished. As a result, all of the transducers fabricated have been done under the primary goal of simply demonstrating functionality, whether for ultrasound generation and reception or for imaging purposes. They have not been optimized for frequency, fill factor, sensitivity, size, ease of packaging or electrical performance among others. As such, to fully explore the potential of the work presented here a next generation of transducers optimized for a specific application will likely need to be fabricated.

In the remainder of this section the most important design changes will be discussed.

7.3.3.1 Packaging

All of the devices fabricated use wire-bonds to electrically connect the transducer to the necessary circuitry. This method of connection has some significant drawbacks. The first is that once a CMUT has been successfully fabricated it is very mechanically robust; the wire bonds on the other hand are not. They have frequently been the reason a particular transducer must be discarded. The contact pads are small and so the opportunity for re-bonding is limited and further, once the transducer has been in the vegetable oil it is difficult to clean sufficiently for wire bonding to be possible. The other, more important reason is that the contact pads require a fairly large amount of surface area on the transducer die. For wire bonding to be fairly straightforward contact pads on the order of 100 μm on a side are necessary with spacing between each of them and the transducers themselves. The lower end of contact pad size that can be reliably bonded is a little less than 70 μm on a side [134]. At higher frequencies of operation the element pitch is below 40 μm and so the contact pads add unwanted size to the transducer. This is not critical for some of the larger low-frequency 64-element or larger arrays because the transducers are large themselves. This does become significant with the high and medium frequency devices where placement in a catheter is the ultimate goal. In that case the surface area of the transducer needs to be around 3 mm on a side or less. For such small transducers all of the available area should be used for the generation and reception of sound. The best way to maximize this is by moving the contact pads to the underside of the transducer and flip-chip bonding the transducer to the necessary electronics. The most obvious way to implement this is to use through wafer vias to connect the top of the wafer to the bottom. This will unfortunately add to the complexity of the fabrication process but will need to be undertaken at some point to facilitate the integration of the transducer into a catheter.

7.3.3.2 Fill Factor

Other less dramatic changes that may be made to the transducer design are to reduce the spacing between cells, reduce the channel widths in the row-column arrays and perhaps change the shape of the transducers from circles to rectangles to improve the fill factor. During the design of the initial devices the spacing between the cells was chosen to be fairly conservative. It seemed prudent that to maximize the likelihood of the bonding success the area that is being bonded should be large. The result of this is that the fill-factor, especially for the high frequency devices, is not as high as it could be. Another manner to increase the fill factor is to use rectangular cells as opposed to round ones.

This has been successfully demonstrated by other groups using the fusion bonding process. It remains to be seen if there would be a significant impact on yield given that the wafers are perhaps not as smooth as the SOI wafers used by the other researchers. There has been a report that while the fill factor is higher with rectangular transducers, the transduction efficiency may actually be lower [135].

With regards to the two-dimensional arrays, a way to improve the fill factor would be to reduce the channel width between the row electrodes. They are about 4 μm across. This value was chosen simply to ensure that fabrication would be easy. Ease of alignment between the various levels was also a factor.

7.4 Concluding Remarks

The purpose of the work described in this thesis has been to design, fabricate and characterize MEMS based ultrasound transducers that are suitable for imaging purposes. Work has been done to develop a novel fabrication process that entails the fusion bonding of two wafers with polished silicon nitride surfaces. This method has a number of advantages over other CMUT fabrication processes described in the literature. This process was modified a couple of times during the course of this work to simplify it and to add the ability to image in three-dimensions. Devices fabricated using this process have been characterized both electrically and acoustically. Electrical characterization demonstrated a lack of dielectric charging for the first generation of devices, identified the resonance frequency of the transducers and was used to characterize the resonant frequency uniformity across many transducers. Acoustic characterization demonstrated the expected broad bandwidth associated with CMUTs. Beyond identifying the acoustic properties of the individual elements of a transducer, work was undertaken to demonstrate imaging of simple two and three dimensional structures. A simple demonstration of three-dimensional imaging was implemented using a row-column addressing scheme. The drive electronics and transducer are very similar in complexity when compared to linear one-dimensional arrays. Some control of the beam aperture is possible when CMUTs are used to instead of piezoelectric transducers permitting good quality imaging near the transducer. Given that the transducers used to demonstrate ultrasonic generation, reception and imaging are essentially first generation devices the results obtained thus far are promising. A number of suggestions have been made for future work and it is hoped that some will be followed through.

References

[1] A. N. DeMaria, J. Narula, E. Mahmud, and S. Tsimikas, "Imaging Vulnerable Plaque by Ultrasound," *J. Am. College of Cardiology*, vol. 47, pp. C32-C39.

[2] M. Kawasaki, K. Sano, M. Okubo, H. Yokoyama, Y. Ito, I. Murata, K. Tsuchiya, S. Minatoguchi, X. Zhou, H. Fujita and H. Fujiwara, "Volumetric Quantitative Analysis of Tissue Characteristics of Coronary Plaques After Statin Therapy Using Three-Dimensional Integrated Backscatter Intravascular Ultrasound," *J. Am. College of Cardiology*, vol. 45, pp. 1946-1953, 2005.

[3] Y. Honda, and P. J. Fitzgerald, "Frontiers in Intravascular Imaging Technologies," *Circulation*, vol. 117, pp. 2024-2037, 2008.

[4] A. Sisman, J. Zahorian, G. Gurun, M. Karaman, M. Balantekin, F. L. Degertekin, and P. Hasler, "Evaluation of CMUT Annular Arrays for Side-looking IVUS," *2009 IEEE Ultrasonics Symposium*, pp. 2774-2777.

[5] J. A. Brown, F. S. Foster, A. Needles, E. Cherin, and G. R. Lockwood, "Fabrication and Performance of a 40-MHz Linear Array Based on a 1-3 Composite with Geometric Elevation Focusing," *IEEE Trans. Ultrason., Ferroelect., Freq. Contr.*, vol. 54, pp. 1888-1894, 2007.

[6] J. M. Cannata, J. A. Williams, Q. Zhou, T. A. Ritter and K. K. Shung, "Development of a 35-MHz piezo-composite ultrasound array for medical imaging", *IEEE Trans. Ultrason. Ferroelect., Freq. Contr.*, vol. 53, no. 1, pp. 224-236, 2006.

[7] J. R. Talman, and G. R. Lockwood, "Evaluation of the Radiation Pattern of a Split Aperture Linear Phased Array for High Frequency Imaging", *IEEE Trans. Ultrason. Ferroelect., Freq. Contr.*, vol. 47, no. 1, pp. 117-124, 2006.

[8] A. Oppelt, *Imaging Systems for Medical Diagnostics* (Edited by A. Oppelt, Publicis Corporate Publishing, Erlanger, Germany, 2005), section 8.1 pp. 184-185.

[9] T. L. Szabo, *Diagnostic Ultrasound Imaging: Inside Out* (Elseview Academic Press, San Diego, 2004), section 1.1, pp. 2-3.

[10] W. D. O'Brien, "Assessing the Risks for Modern Diagnostic Ultrasound Imaging", *Jpn. J. Appl. Phys.*, vol 37, pp. 2781-2788.

[11] T. L. Szabo, *Diagnostic Ultrasound Imaging: Inside Out* (Elseview Academic Press, San Diego, 2004), section 1.2, pp. 4-6.

[12] A. Oppelt, *Imaging Systems for Medical Diagnostics* (Edited by A. Oppelt, Publicis Corporate Publishing, Erlanger, Germany, 2005), section 8.2 pp. 185-196.

[13] T. L. Szabo, *Diagnostic Ultrasound Imaging: Inside Out* (Elseview Academic Press, San Diego, 2004), section 1.8, pp. 22-25.

[14] L. J. Thomas, *Imaging Systems for Medical Diagnostics* (Edited by A. Oppelt, Publicis Corporate Publishing, Erlanger, Germany, 2005), section 16.1 pp. 732.

[15] T. L. Szabo, *Diagnostic Ultrasound Imaging: Inside Out* (Elseview Academic Press, San Diego, 2004), section 1.4, pp. 12-16.

[16] L. J. Thomas, *Imaging Systems for Medical Diagnostics* (Edited by A. Oppelt, Publicis Corporate Publishing, Erlanger, Germany, 2005), section 16.2 pp. 745-767.

[17] C. E. Morton, G. R. Lockwood, "Evaluation of Kerfless Linear Arrays,"*2002 IEEE Ultrasonics Symposium*, pp. 1257-1260, 2002

[18] T. L. Szabo, *Diagnostic Ultrasound Imaging: Inside Out* (Elseview Academic Press, San Diego, 2004), section 5.7, pp. 123-127.

[19] M. Lukacs, J. Yin, G. Pang, R. C. Garcia, E. Cherin, R. Williams, J. Mehi, and F. S. Foster, "Performance and Characterization of New Micromachined High-Frequency Linear Arrays", *IEEE Trans. Ultrason. Ferroelect., Freq. Contr.*, vol. 53, pp. 1719-1729, 2006.

[20] I. Ladabaum, X. Jin, H. T. Soh, A. Atalar and B. T. Khuri-Yakub, "Surface Micromachined Ultrasonic Transducers", *IEEE Trans. Ultrason., Ferroelect., Freq. Contr.*, vol. 45, pp. 678-690, 1998.

[21] G. S. Kino, *Acoustic Waves – Devices, Imaging, & Analog Signal Processing*. Englewood Cliffs, NJ: Prentice-Hall, Inc, 1987.

[22] A. R. Selfridge, "Approximate material properties in isotropic materials", *IEEE Trans. Son. Ultrason.*, vol. SU-32, no. 3, pp. 381-394, 1985.

[23] D. M. Mills, "Medical imaging with capacitive micromachined ultrasound transducer (CMUT) Arrays", *Proc. IEEE Ultrason. Symp.*, vol. 1, 2004, pp. 384-390.

[24] J. A. Brown, F. S. Foster, A. Needles, E. Cherin, and G. R. Lockwood, "Fabrication and performance of a 40-MHz linear array based on 1-3 composite with geometric elevation focusing", *IEEE Trans. Ultrason. Ferroelect., Freq. Contr.*, vol. 54, no. 9, pp. 1888-1894, 2007.

[25] K. A. Snook, C-H. Hu, T. R. Shrout and K. K. Shung, "High-frequency ultrasound annular-array imaging. Part I: array design and fabrication", *IEEE Trans. Ultrason. Ferroelect., Freq. Contr.*, vol. 53, pp. 300-308, 2006.

[26] J. M. Cannata, J. A. Williams, and K. K. Shung, "A Kerfless 30 MHz Linear Ultrasonic Array", *2005 IEEE Ultrasonics Symposium*, pp. 109-112, 2005.

[27] R. Liu, K. A. Harasiewicz, and F. S. Foster, "Interdigital Pair Bonding for High Frequency (20-50 MHz) Ultrasonic Composite Transducers", *IEEE Trans. Ultrason. Ferroelect., Freq. Contr.*, vol. 48, pp. 299-306, 2001.

[28] F. V. Hunt, *Electroacoustics: The Analysis of Transduction, and Its Historical Background* (Harvard University Press, Cambridge, Massachusetts, 1954), Chapter 1, pp. 1-91.

[29] M. I. Haller, B. T. Khuri-Yakub, "A surface micromachined electrostatic ultrasonic air transducer", *Proc. IEEE Ultrason Symp.*, vol. 2, 1994, pp. 1241-1244.

[30] M. I. Haller, B. T. Khuri-Yakub, "A surface micromachined electrostatic ultrasonic air transducer", *IEEE Trans. Ultrason. Ferroelect., Freq. Contr.*, vol. 43, no. 1, pp. 1-6, 1996.

[31] I. Ladabaum, B. T. Khuri-Yakub, D. Spoliansky and M. I. Haller, "Micromachined ultrasonic transducers (MUTs)", *Proc. IEEE Ultrason. Symp.*, vol. 1, 1995, pp. 501-504.

[32] P-C Eccardt, K. Niederer, T. Scheiter and C. Hierold, "Surface micromachined ultrasound transducers in CMOS technology", *Proc. IEEE Ultrason. Symp.*, vol. 2, 1996, pp. 959-962.

[33] Y. Huang, A. S. Ergun, E. Haeggstrom, M. H. Badin and B. T. Khuri-Yakub, "Fabricating Capacitive Micromachined Ultrasonic Transducers with Wafer-Bonding Technology", *J. MEMS*, vol. 12, pp. 128-137, 2003.

[34] D. T. Yeh, O. Oralken, A. S. Ergun, X. Zhuang, I. O. Wygant and B. T. Khuri-Yakub, "High-Frequency CMUT Arrays for High-Resolution Medical Imaging", *Medical Imaging 2005 Proc. SPIE*, vol. 5750, pp. 87-98, 2005.

[35] O. Oralken, S. T. Hansen, B. Bayram, G. G. Yaralioglu, A. S. Ergun and B. T. Khuri-Yakub, "High-Frequency CMUT Arrays for High-Resolution Medical Imaging", *2004 IEEEUltrasonics Symp.*, pp. 399-402, 2004.

[36] C. Daft, P. Wagner, B. Bymaster, S. Panda, K. Patel and I Ladabaum, "CMUTs and Electronics for 2D and 3D Imaging: Monlithic Integration, In-Handle Chip Sets and System Implications", *2005 IEEE Ultrasonics Symp.*, pp. 463-474, 2005.

[37] X. Zhuang, I. O. Wygant, D-S. Lin, M. Kupnik, O. Oralkan, and B. T. Khuri-Yakub, "Wafer-bonded 2-D CMUT arrays incorporating through-wafer trench-isolated interconnects with a

supporting frame," IEEE Trans. Ultrason. Ferroelectr. Freq. Control, vol. 56, no. 1, pp. 182-192, 2009.

[38] I. O. Wygant, N. S. Jamal, H. J. Lee, A. Nikoozadeh, O. Oralkan, M. Karaman, and B. T. Khuri-Yakub, "An Integrated Circuit with Transmit Beamforming Flip-Chip Bonded to a 2-D CMUT Array for 3-D Ultrasound Imaging", Trans. Ultrason. Ferroelectr. Freq. Contr., vol 56, pp. 2145-2156.

[39] I. O. Wygant, D. T. Yeh, X. Zhuang, A. Nikoozadeh, O. Oralkan, A. S. Ergun, M. Karaman, and B. T. Khuri-Yakub, "A Miniature Real-Time Volumetric Ultrasound Imaging System," Proc. SPIE Medical Imaging 2005, vol. 5750, pp. 26-36, 2005.

[40] R. Wodnicki, C. G. Woychik, A. T. Byun, R. Fisher, K. Thomenius, D.-S. Lin, X. Zhuang, O. Oralkan, S. Vaithilingam, and B. T. Khuri-Yakub, "Multi-Row Linear CMUT Array Using CMUTs and Multiplexing Electronics", 2009 IEEE Ultrasonics Symposium, pp. 2696-2699, 2009.

[41] A. Nikoozadeh, O. Oralkan, M. Gencel, J. W. Choe, D. N. Stephens, A. de la Rama, P. Chen, K. Thomenius, A. Dentinger, D. Wildes, K. Shivkumar, A. Mahajan, M. O'Donnell, D. Sahn and B. T. Khuri-Yakub, "Forward-Looking Volumetric Intracardiac Imaging Using a Fully Integrated CMUT Ring Array", *2009 IEEE Ultrasonics Symposium*, pp. 511-514, 2009.

[42] F. L. Degertekin, R. O. Guldiken, and M. Karaman, "Annular-Ring CMUT Arrays for Forward-Looking IVUS: Transducer Characterization and Imaging", IEEE Trans. Ultrason. Ferroelectr. Freq. Contr., vol. 53, pp. 474-482, 2006.

[43] C. Daft, S. Calmes, D. de Graca, K. Patel, P. Wagner and I. Ladabaum, "Microfabricated Ultrasonic Transducers Monolithically Integrated with High Voltage Electronics", *2004 IEEE Ultrasonics Symposium*, pp. 493-496, 2004.

[44] G. Gorun, M. S. Qureshi, M. Balantekin, R. Guldiken, J. Zahorian, S-Y. Pend, A. Basu, M. Karaman, P. Hasler, and L. Degertekin, "Front-end CMOS Electronics for Monolithic Integration with CMUT Arrays: Circuit Design and Initial Experimental Results", *2008 IEEE Ultrasonics Symposium*, pp. 390-393, 2004.

[45] S. Linder, H. Baltes, F. Gnaedinger and E. Doering, "Fabrication Technology for Wafer Through-Hole Interconnections and Three-Dimensional Stacks of Chips and Wafers", *1994 IEEE Proc. Micro Electro Mech Syst.*, pp. 349-354, 2004.

[46] C. H. Cheng, A. S. Ergun and B. T. Khuri-Yakub, "Electrical Through-Wafer Interconnects with Sub-PicoFarad Parasitic Capacitance", *2001 MEMS*, pp18-21, 2001.

[47] X. Zhuang, A. S. Ergun, Y. Hongli, I. O. Wygant, O. Oralkan and B. T. Khuri-Yakub, "Integration of Trench-Isolated Through-Wafer Interconnects with 2D Capacitive Micromachined Ultrasonic Transducer Arrays", *Sensors and Actuators A*, vol. 138, pp. 221-229, 2007.

[48] R. A. Noble, A. D. R. Jones, T. J. Robertson, D. A. Hutchins and D. R. Billson, "Novel, Wide Bandwidth, Micromachined Ultrasonic Transducers", *IEEE Trans. Ultrason., Ferroelect., Freq. Contr.*, vol. 48, pp. 1495-1507, 2001.

[49] J. Knight, J. McLean and F. L. Degertekin, "Low Temperature Fabrication of Immersion Capacitive Micromachined Ultrasonic Transducers on Silicon and Dielectric Substrates", *IEEE Trans. Ultrason., Ferroelect., Freq. Contr.*, vol. 51, pp. 1324-1333, 2004.

[50] M. Wang, J. Chen, J-C. Cheng, and P-C. Li, "Design and Test of a Monolithic Ultrasound-Image-Guided HIFU Device Using Annular CMUT Rings", *2008 IEEE Ultrasonics Symposium*, pp. 459-462, 2008.

[51] S. Wong, M. Kupnik, R. D. Watkins, K. Butts-Pauly, and B. T. Khuri-Yakub, "Capacitive Micromachined Ultrasonic Transducers for Therapeutic Ultrasound Applications", *IEEE Trans. Biomedical Eng.*, vol. 57, pp. 114-123, 2010.

[52] H. Jagannathan, G. G. Yaralioglu, A. S. Ergun, F. L. Degertekin, and B. T. Khuri-Yakub, "Micro-Fluidic Channels with Integrated Ultrasonic Transducers", *2001 IEEE Ultrasonics Symposium*, pp. 859-862, 2001.

[53] P. Cristman, O. Oralkan, X. Zhuang, T.-J. Ma, S. Vaithilingam, T. Carver, I. Wygant, and B. T. Khuri-Yakub, "A 2D CMUT Hydrophone Array: Characterization Results," *2009 IEEE Ultrasonics Symposium*, pp. 992-995, 2009.

[54] M. Thranhardt, P.-C. Eccardt, H. Mooshofer, P. Hauptmann, and F. L. Degertekin, "A resonant CMUT Sensor for Fluid Applications", *2009 IEEE Sensors Conference*, pp. 878-883, 2009.

[55] B. T. Khuri-Yakub, K. K. Park, H. J. Lee, G. G. Yaralioglu, S. Ergun, O. Oralkan, M. Kupnik, C. F. Quate, T. Braun, H. P. Lang, M. Hegner, J.-P. Ramseyer, C. Gerber, and J. Gimzeqski, "The Capacitive Micromachined Ultrasonic Transducer (CMUT) as a Chem/Bio Sensor", *2007 IEEE Ultrasonics Symposium*, pp. 472-475, 2007.

[56] H. J. Lee, K. K. Park, P. Cristman, O. Oralkan, M. Kupnik, and B. T. Khuri-Yakub, "A Low-Noise Oscillator Based on a Multi-Membrane CMUT for High-Sensitivity Resonant Chemical Sensors," *2009 IEEE MEMS Conf*, pp. 761-764, 2009.

[57] S. Vaithilingam, T.-J. Ma, Y. Furukawa, I. O. Wygant, X. Zhuang, A. De La Zerda, O. Oralkan, A. Kamaya, S. S. Gambhir, R. B. Jeffrey, and B. T. Khuri-Yakub, "Three-Dimensional Photoacoustic Imaging Using a Two-Dimensional CMUT Array," *IEEE Trans. Ultrason., Ferroelect., Freq. Contr.*, vol. 56, pp. 2411-2419, 2009.

[58] J, Liu, C. Oakley, and R. Shandas, "Capacitive Micromachined Ultrasonic Transducers Using Commercial Multi-User MUMPs Process: Capability and Limitations," *Ultrasonics,* vol. 49, pp. 765-773, 2009.

[59] A. Coppa, E. Cianci, V. Foglietti, G. Caliano, and M. Pappalardo, "Building CMUTs for Imaging Applications From Top to Bottom," *Microelect. Eng.*, vol. 84, pp. 1312-1314, 2007.

[60] A. Caronti, A. Coppa, A. Savoia, C. Longo, P. Gatta, B. Mauti, A. Corbo, B. Calabrese, G. Bollino, A. Paz, G. Caliano, and M. Pappalardo, "Curvilinear Capacitive Micromachined Ultrasonic Transducer (CMUT) Array Fabricated Using a Reverse Process,"*2008 IEEE Ultrasonics Symposium*, pp. 2092-2095, 2008.

[61] A. Logan, J. T. W. Yeow, "Fabricating Capacitive Micromachined Ultrasonic Transducers with a Novel Silicon-Nitride-Based Wafer Bonding Process," *IEEE Trans. Ultrason., Ferroelect., Freq. Contr.*, vol. 56, pp. 1074-1084, 2009.

[62] K. Midtbø, A. Rønnekleiv and D. T. Wang, "Fabrication and characterization of CMUTs realized by wafer bonding", *Proc. IEEE Ultrason. Symp.*, vol. 1, 2006, pp. 938-941.

[63] K. K. Park, H. J. Lee, M. Kupnik, O.Oralkan, and B. T. Khuri-Yakub, "Fabricating Capacitive Micromachined Ultrasonic Transducers with Direct Wafer-Bonding and LOCOS Technology," *2008 IEEE MEMS Conf.*, pp. 339-342, 2008.

[64] S. Olcum, K. Oguz, M. N. Senlik, F. Y. Yamaner, A. Bozkurt, A. Atalar and H. Koymen, "Wafer Bonded Capacitive Micromachined Underwater Transducers", *2009 IEEE Ultrasonics Symposium*, pp. 976-979, 2009.

[65] A. S. Ergun, Y. Huang, X. Zhuang, O. Oralkan, G. G. Yaralioglu, and B. T. Khuri-Yakub, "Capacitive Micromachined Ultrasonic Transducers: Fabrication Technology," *IEEE Trans. Ultrason., Ferroelect., Freq. Contr.*, vol. 52, pp. 2242-2258, 2005.

[66] M. A. Averkiou, "Tissue Harmonic Imaging," *2000 IEEE Ultrasonics Symposium*, pp. 1563-1572, 2000.

[67] S. Zhou, and J. A. Hossack, "Reducing Inter-Element Acoustic Crosstalk in Capacitive Micromachined Ultrasonic Micromachined Transducers", *IEEE Trans. Ultrason., Ferroelect., Freq. Contr.*, vol 54, pp. 1217-1228, 2007.

[68] S. Zhou, P. Reynolds, and J. Hossack, "Precompensated Excitation Waveforms to Suppress Harmonic Generation in MEMS Electrostatic Transducers", *IEEE Trans. Ultrason., Ferroelect., Freq. Contr.*, vol 51, pp. 1564-1574, 2004.

[69] O. Oralkan, A. S. Ergun, J. A. Johnson, M. Karaman, U. Demirci, K. Kaviani, T. H. Lee, and B. T. Khuri-Yakub, "Capacitive Micromachined Ultrasonic Transducers: Next-Generation Arrays for Acoustic Imaging?" *IEEE Trans. Ultrason., Ferroelect., Freq. Contr.*, vol. 49, pp. 1596-1610, 2002.

[70] S. Berg, and A. Ronnekleiv, "Reducing Fluid Coupled Crosstalk Between Membranes in CMUT Arrays by Introducing a Lossy Top Layer", *2006 IEEE Ultrasonics Symposium*, pp. 594-597, 2006.

[71] Y. Roh, and B. T. Khuri-Yakub, "Finite Element Analysis of Underwater Capacitor Micromachined Ultrasonic Transducers", *IEEE Trans. Ultrason., Ferroelect., Freq. Contr.*, vol 49, pp. 293-298, 2002.

[72] J.-H. Ma, J. B. Fowlkes, A. L. Robinson, and P. L. Carson, "Crosstalk Reduction with a Micromachined Diaphragm Structure for Integrated Ultrasound Transducer Arrays", *IEEE Trans. Ultrason., Ferroelect., Freq. Contr.*, vol. 39, pp. 48-55, 1992.

[73] K. R. Chapagain, and A. Ronnekleiv, "Minimizing the Bottom Reflection in Ultrasonic CMUT Transducer Backing Using Low Profile Structuring," *2009 IEEE Ultrasonics Symposium*, pp. 430-433, 2009.

[74] S. Berg, and A, Ronnekleiv, "Challenges with Acoustic Backing of CMUT Arrays on Silicon with Integrated Electronics", *2009 IEEE Ultrasonics Symposium*, pp. 980-983, 2009.

[75] C. Goldsmith, J. Ehmke, A. Malczewski, B. Pillans, S. Eshelman, Z. Yao, J. Brank and M. Eberly, "Lifetime characterization of capacitive MEMS switches", *Microwave Symp. Digest*, vol. 1, 2001, pp. 227-230.

[76] J. DeNatale, R. Mihailovich, "RF MEMS reliability", *12th Int. Conf, Solid State Sens. Actuators Microsyst.*, vol. 2, 2001, pp. 943-946.

[77] Y. Huang, E. O. Haeggstrom, X. Zhuang, A. S. Ergun and B. T. Khuri-Yakub, "A solution to the charging problems in capacitive micromachined ultrasonic transducers", *IEEE Trans. Ultrason. Ferroelect., Freq. Contr.*, vol. 52, no. 4, pp. 578-580, 2005.

[78] W. P. Mason, *Electromechanical Transducers and Wave Filters* (D. Van Nostrand Company, Inc., Toronto, Canada, 1948).

[79] G. G. Yaralioglu, M. H. Badi, A. S. Ergun, and B. T. Khuri-Yakub, "Improved Equivalent Circuit and Finite Element Method Modeling of Capacitive Micromachined Ultrasonic Transducers", *2003 IEEE Ultrasonics Symposium*, pp. 469-472., 2003

[80] F. Y. Yamaner, and A. Bozkurt, "Modeling the Pulse-Echo Response of a 2D CMUT Array Element," *2009 IEEE Ultrasonics Symposium*, pp. 1-4, 2009.

[81] A. Caronti, G. Caliano, A. Iula, and M. Pappalardo, "An Accurate Model for Capacitive Micromachined Ultrasonic Transducers", *IEEE. Trans. Ultrason., Ferroelect., Freq., Contr.*, vol. 49, pp. 159-168, 2002.

[82] A. Ronnekleiv, "CMUT Array Modeling Through Free Acoustic CMUT Modes and Analysis of the Fluid CMUT Interface Through Fourier Transform Methods," *IEEE. Trans. Ultrason., Ferroelect., Freq., Contr.*, vol. 52, pp. 2173-2184, 2005.

[83] A. Lohfink, P.-C. Eccardt, W. Benecke, and H. Meixner, "Derivation of a 1D CMUT Model from FEM Results for Linear and Nonlinear Equivalent Circuit Simulation", *2003 IEEE Ultrasonics Symposium*, pp. 465-468, 2003.

[84] D. Certon, F. Teston, and F. Patat, "A Finite Difference Model for CMUT Devices", *IEEE. Trans. Ultrason., Ferroelect., Freq., Contr.*, vol. 52, pp. 2199-2210, 2005.
[85] H, K, Oguz, S. Olcum, M. N. Senlik, A. Atalar, and H. Koymen, "A Novel Equivalent Circuit Model for CMUTs", *2009 IEEE Ultrasonics Symposium*, pp. 2193-2196, 2009.
[86] H. A. C. Tilmans, "Equivalent Circuit Representation of Electromechanical Transducers: II. Distributed-Parameter Systems", *J. Micromech. Microeng.*, vol. 7, pp. 285-309, 1997.
[87] G. W. Vogl, and A. H. Nayfeh, "Primary Resonance Excitation of Electrically Actuated Clample Circular Plates", *Nonlinear Dyn.*, pp. 181-192, 2007.
[88] F. V. Hunt, *Electroacoustics: The Analysis of Transduction, and Its Historical Background* (Harvard University Press, Cambridge, Massachusetts, 1954), Chapter 6, pp. 168-212.
[89] A. S. Ergun, G. G. Yaralioglu and B. T. Khuri-Yakub, "Capacitive Micromachined Ultrasonic Transducers: Theory and Technology", *J. Aerospace Eng.*, vol. 16, pp. 76-84, 2003.
[90] U. Demirci, A. S. Ergun, O. Oralkan, M. Karaman and B. T. Khuri-Yakub, "Forward-Viewing CMUT Arrays for Medical Imaging", *IEEE. Trans. Ultrason., Ferroelect., Freq., Contr.*, vol. 51, pp. 886-894, 2004.
[91] S. Olcum, M. N. Selnik and A. Atalar, "Optimization of the Gain-Bandwidth Product of Capacitive Micromachined Ultrasonic Transducers", *IEEE. Trans. Ultrason., Ferroelect., Freq., Contr.*, vol. 52, pp. 2211-2219, 2005.
[92] R. O. Guldiken, J. McLean and F. L. Degertekin, "CMUTs with Dual-Electrode Structure for Improved Transmit and Receive Performance", *IEEE. Trans. Ultrason., Ferroelect., Freq., Contr.*, vol. 53, pp. 483-491, 2006.
[93] A. Caronti, G. Caliano, A. Iula and M. Pappalardo, "An Acurate Model for Capacitive Micromachined Ultrasonic Transducers", *IEEE. Trans. Ultrason., Ferroelect., Freq., Contr.*, vol. 49, pp. 159-168, 2002
[94] H. A. C. Tilmans, "Equivalent Circuit Representation of Electromechanical Transducers: I. Lumped- Parameter System", *J. Micromech. Microeng.*, 6, pp. 157-176, 1996.
[95] A. H. Nayfeh, *Nonlinear Interaction: Analytical, Computational, and Experimental Methods* (Wiley, New York, 2000).
[96] T. L. Szabo, *Diagnostic Ultrasound Imaging: Inside Out* (Elseview Academic Press, San Diego, 2004), section 5.3, pp. 106.-110.
[97] G. G. Yaralioglu, M. H. Badi, A. S. Ergun and B. T. Khuri-Yakub, "Improved Equivalent Circuit and Finite Element Method Modelling of Capacitive Micromachined Ultrasonic Transducers", *2003 Ultrasonics Symp.*, pp. 469-472, 2003.
[98] A. Caronti, R. Carotento, G. Caliano, and M. Pappalardo, "The Effects of Membrane Metallization in Capacitive Microfabricated Ultrasonic Transducers", *J. Acoustic. Soc. Am.*, vol. 115, pp. 651-657, 2004.
[99] G. G. Yaralioglu, M. H. Badi, A. S. Ergun and B. T. Khuri-Yakub, "Improved Equivalent Circuit and Finite Element Method Modelling of Capacitive Micromachined Ultrasonic Transducers", *2003 Ultrasonics Symp.*, pp. 469-472, 2003.
[100] O. Oralkan, A. S. Ergun, J. A. Johnson, M. Karaman, U. Demirci, K. Kaviani, T. H. Lee and B. T. Khuri-Yakub, "Capacitive micromachined ultrasonic transducers: next-generation arrays for acoustic imaging?", *IEEE Trans. Ultrason., Ferroelect., Freq. Contr.*, vol 49, no. 11, pp. 1596-1610, 2002.
[101] X. Zhuang, A. Nikoozadeh, M. A. Beasley, G. G. Yaralioglu, B. T. Khuri-Yakub, and B. L. Pruitt, "Biocompatible Coatings for CMUTs in a Harsh, Aqueous Environment," *J. Micromech. & Microeng.*, vol. 17, pp. 994-1001, 2007.
[102] R. Chanamai and D. J. McClements, "Ultrasonic Attenuation of Edible Oils", *J. Am. Oil Chem. Soc.*, vol. 75, no. 10, pp. 1447-1448, 1998.

[103] T. L. Szabo, *Diagnostic Ultrasound Imaging: Inside Out* (Elseview Academic Press, San Diego, 2004), section 6.3, pp. 142.-148.
[104] I. Ladabaum, P. Wagner, C. Zanelli, J. Mould, P. Reynolds and G. Wojcik, "Silicon substrate ringing in microfabricated ultrasonic transducers", *Proc. IEEE Ultrason. Symp.*, vol. 1, 2000, pp. 943-946.
[105] S. Machida, S. Migitaka, H. Tanaka, K. Hashiba, H. Enomoto, Y. Tadaki, and T. Kobayashi, "Analysis of the Charging Problem in Capacitive Micro-machined Ultrasonic Transducers", *2008 IEEE Ultrasonics Symposium*, pp. 383-385, 2008.
[106] P. Tournois, S. Calisti, Y. Doisy, J.M. Bureau, and F. Bernard, "A 128x4 Channels 1.5D Curved Linear Array for Medical Imaging,", *1995 IEEE Ultrasonics Symposium*, pp. 1331-1335, 1995.
[107] D. G. Wildes, R. Y Chiao, C. M. W. Daft, K. W. Rigby, L. S. Smith, and K. E. Thomenius, "Elevation Performance of 1.25D and 1.5D Transducer Arrays", *IEEE Trans. Ultrason., Ferroelect., Freq. Contr.*, vol. 44, pp. 1027-1037, 1997.
[108] D. T. Yeh, O. Oralkan, I. O. Wygant, M. O'Donnell, and B. T. Khuri-Yakub, "3-D Ultrasound Imaging Using a Forward-Looking CMUT Ring Array for Intravascular/Intracardiac Applications", *IEEE Trans. Ultrason., Ferroelect., Freq. Contr*., vol. 53, pp. 1202-1211, 2006.
[109] Y. Wang, D. N. Stephens, and M. O'Donnell, "Optimizing the Beam Pattern of a Forward-Viewing Ring-Annular Ultrasound Array for Intravascular Imaging", *IEEE Trans. Ultrason., Ferroelect., Freq. Contr*., vol. 49, pp. 1652-1664, 2002.
[110] A. S. Logan, and J. T. W. Yeow, "1-D CMUT Arrays Fabricated Using a Novel Wafer Bonding Process", *2008 IEEE Ultrasonics Symposium*, pp. 1226-1229, 2008.
[111] www.ondacorp.com
[112] J. Olson, "Analysis of LPCVD Process Conditions for the Deposition Low Stress Silicon Nitride. Part I: Preliminary LPCVD Experiments", *Mat. Sci. in Semiconduc. Process.*, vol 5, pp. 51-60, 2002.
[113] T. L. Szabo, Diagnostic Ultrasound Imaging: Inside Out (Elseview Academic Press, San Diego, 2004), section 7.4, pp. 177-190.
[114] I. O Wygant, N. S. Jamal, H. J. Lee, A. Nikoozadeh, O. Oralkan, M. Karaman, and B. T. Khuri-Yakub, "An Integrated Circuit with Transmit Beamforming Flip-Chip Bonded to a 2-D CMUT Array for 3-D Ultrasound Imaging," *IEEE Trans. Ultrason. Ferroelectr. Freq. Contr.,* vol. 56, pp. 2145-2156, 2009.
[115] J. L. Schwartz, and B. D. Steinberg, "Ultrasparse, Ultrawideband Arrays," IEEE Trans. Ultrason. Ferroelectr. Freq. Contr., vol. 45, pp. 376-493, 1998.
[116] V. Bavaro, G. Caliano, and M. Pappalardo, "Element Shape Design of 2-D CMUT Arrays for Reducing Grating Lobes," *IEEE Trans. Ultrason. Ferroelectr. Freq. Contr.,* vol. 55, pp. 308-318, 2008.
[117] G. R. Lockwood, P. –C. Li, M. O'Donnell, and F. S. Foster, "Optimizing the Radiation Pattern of Sparse Periodic Linear Arrays," IEEE Trans. Ultrason. Ferroelectr. Freq. Contr., vol. 43, pp. 7-14, 1996.
[118] M. Karaman, I. O. Wygant, O. Oralkan, B. T. Khuri-Yakub, "Minimally Redundant 2-D Array Designs for 3-D Medical Ultrasound Imaging," *IEEE Trans. Medical Imag.*, vol. 28, pp. 1051-1061, 2009.
[119] G. R. Lockwood, J. R. Talman, and S. S. Brunke, "Real-Time 3-D Ultrasound Imaging Using Sparse Synthetic Aperture Beamforming", *IEEE Trans. Ultrason. Ferroelectr. Freq. Contr.*, vol. 45, pp. 980-988, 1998.

[120] S. I. Nikolov, and J. A. Jensen, "3D Synthetic Aperture Imaging Using a Virtural Source Element in the Elevation Plane", *2000 IEEE Ultrasonics Symposium*, pp. 1743-1747, 2000.
[121] N. M. Daher, and J. T. Yen, "2-D Array for 3-D Ultrasound Imaging Techniques Using Synthetic Aperture Techniques," *IEEE Trans. Ultrason. Ferroelectr. Freq. Contr.*, vol. 53, pp. 912-924, 2006.
[122] I. O. Wygant, X. Zhuang, D. T. Yeh, O. Oralkan, A. S. Ergun, M. Karaman, and B. T. Khuri-Yakub, "Integration of 2D CMUT Arrays with Front-End Electronics for Volumetric Ultrasound Imaging", *IEEE Trans. Ultrason. Ferroelectr. Freq. Contr.*, vol. 55, pp. 327-342, 2008.
[123] C. H. Seo, and J. T. Yen, "A 256x256 2-D Array Transducer with Row-Column Addressing for 3-D Rectilinear Imaging," *IEEE Trans. Ultrason. Ferroelectr. Freq. Contr.*, vol. 56, pp. 837-847, 2009.
[124] C. E. M. Demore, A. W. Joyce, K. Wall, and G. R. Lockwood, "Real-Time Volume Imaging Using a Crossed Electrode Array", *IEEE Trans. Ultrason. Ferroelectr. Freq. Contr.*, vol. 56, pp. 1252-1261, 2009.
[125] A. S. Logan, L. L. Wong, and J. T. W. Yeow, "2-D CMUT Wafer Bonded Imaging Arrays with a Row-Column Addressing Scheme", *2009 IEEE Ultrasonics Symposium*, pp. 984-987, 2009.
[126] C. E. Morton, G. R. Lockwood, "Theoretical Assessment of a Crossed Electrode 2-D Array for 3-D Imaging", *2003 IEEE Ultrasonics Symposium*, pp. 968-971, 2003.
[127] C. Daft, P. Wagner, S. Panda, and I. Ladabaum, "Elevation Beam Profile Control with Bias Polarity Applied to Microfabricated Ultrasound Transducers", *2003 IEEE Ultrasonics Symposium*, pp. 1578-1581, 2003
[128] C. Daft, S. Panda, and I. Ladabaum, "Two Approaches to Electronically Scanned 3D Imaging Using CMUTs", *2006 IEEE Ultrasonics Symposium*, pp. 685-688, 2006.
[129] M. I. Fuller, K. Owen, T. N. Blalock, J. A. Hossack, and W. F. Walker, "Real Time Imaging with the Sonic Window: A Pocket-Sized, C-Scan, Medical Ultrasound Device," *2009 IEEE Ultrasonics Symposium*, pp. 196-199, 2009.
[130] A. Bozkurt, I. Ladabaum, A. Atalar and B. T. Khuri-Yakub, "Theory and analysis of electrode size optimization for capacitive microfabricated ultrasonic transducers", *IEEE Trans. Ultrason. Ferroelect., Freq. Contr.*, vol. 46, no. 6, pp. 1364-1374, 1999.
[131] K. R. Williams, and R. S. Muller, "Etch Rates for Micromachining Processing," *IEEE J. MEMS*, vol. 5, pp. 256-269, 1996.
[132] O. T. von Romm, S. W. Smith, H. G. Pavy Jr., "High-Speed Ultrasound Volumetric Imaging System – Part II: Parallel Processing and Imaging Display," *IEEE Trans. Ultrason. Ferroelectr. Freq. Contr.*, vol. 38, pp. 109-115, 1991.
[133] A. Drukarev, K. Konstantinides, G. Seroussi, "Beam Transformation Techniques for Ultrasonic Medical Imaging," *IEEE Trans. Ultrason. Ferroelectr. Freq. Contr.*, vol. 40, pp. 717-726, 1993.
[134] Private communication with Alireza Rezvani, 2010.
[135] S. H. Wong, M. Kupnik, X. Zhuang, D.-S. Lin, K. Butts-Pauly, and B. T. Khuri, Yakub, "Evaluation of Wafer Bonded CMUTs with Rectangular Membranes Featuring High Fill Factor", *IEEE Trans. Ultrason. Ferroelectr. Freq. Contr.*, vol. 55, pp. 2035-2065, 2008.